THEORY AND DESIGN OF NEXT-GENERATION RETRODIRECTIVE TAGS AND THEIR CHANNELS

A Dissertation
Presented to
The Academic Faculty

By

Mohammad Alhassoun

In Partial Fulfillment
of the Requirements for the Degree
Doctor of Philosophy in the
School of Electrical and Computer Engineering

Georgia Institute of Technology

December 2019

THEORY AND DESIGN OF NEXT-GENERATION RETRODIRECTIVE TAGS AND THEIR CHANNELS

Approved by:

Prof. Gregory D. Durgin, Advisor
School of Electrical and Computer Engineering
Georgia Institute of Technology

Prof. Andrew F. Peterson
School of Electrical and Computer Engineering
Georgia Institute of Technology

Prof. John R. Barry
School of Electrical and Computer Engineering
Georgia Institute of Technology

Prof. Paul G. Steffes
School of Electrical and Computer Engineering
Georgia Institute of Technology

Prof. R. Michael Buehrer
Bradley Department of Electrical and Computer Engineering
Virginia Polytechnic Institute and State University

Date Approved: November 06, 2019

I am very seldom interested in applications. I am more interested in the elegance of a problem. Is it a good problem? An interesting problem?

Claude Shannon

To my mother, Hussa;

my aunt, Modhawi;

my wife, Leena;

and my little angle, Norah

ACKNOWLEDGEMENTS

First and foremost, all praise and thanks to Almighty Allah for showering me with his blessings, guiding me throughout this journey, giving me the strength and ability to overcome all difficulties, and everything in my life.

I want to sincerely thank my advisor, Prof. Gregory Durgin, for his endless support, guidance, and encouragement. From the moment I set foot in his office, he welcomed me with nothing but a great smile and willingness to make me—and everyone in his lab—not only a better researcher, but also a much better person. He is both an advisor and a mentor. I am grateful for all of the valuable comments and helpful feedback that he provided me throughout the years I was in his group. I cannot thank him enough for all of the opportunities that he gave me to strengthen both my research and teaching skills. I want also to thank him for generously allowing me to use his office to run my experiments.

I want also to extend my thanks to Prof. Andrew Peterson for reviewing my dissertation and providing me with valuable feedback. After taking his applied electromagnetic class, I knew that electromagnetic is my PhD field. I want to thank him also for all of the fruitful discussions that I had with him and for generously making his own office library available to me whenever I needed to borrow a book.

I am grateful for my other committee members: Prof. John Barry, Prof. Paul Steffes, and Prof. Michael Buehrer for their time, helpful comments, and valuable feedback. I want to specifically thank Prof. Buehrer for hosting me in his lab at Virginia Tech and for the wonderful experience I had there.

I owe special thanks to Dr Muhammad Bashir Akbar and Dr Francesco Amato for their technical and emotional support. I want to thank them for the valuable discussions, limitless guidance, and treating me like a younger brother.

A bundle of thanks goes to my current and former colleagues: Dr. Sang Kyu Kim, Dr. Blake Marshall, Qi Cheng, Michael Vernar, Qian Yang, Robert Corless, David Giles, Emily Backer, and Will Braddock. I want to thank them all for their kindness and friendship.

I am deeply indebted to Prof. Ghassan AlRegib for his unwavering support from the moment I joined Georgia Tech. His advice, guidance, and encouragement provided me with

the strength I needed to successfully complete my PhD journey.

This work and myself owe a great deal of thanks to James Steinberg, Kevin Pham, and Kevin Ferri. With their help and support, the impossible becomes possible. Their friendship is one of the most valuable things I have at Georgia Tech. I want to thank them all for believing in me.

My thanks extend to ECE staff: Sharon Pugh, for always being in my side; and Dr Daniela Staiculescu for making me focus on nothing but my research.

The people who shared this journey with me deserve a tremendous amount of thanks. In particular, sincere thanks to Abdallah Alshehri, Thamer Alquthami, Wail Falath, Hussain Albinali, Said Alabri, Yazeed Alaudah, Salem Alotaibi, Tariq Alshawi, Ali Alreshaid, Maad Alowaifeer, and to all Saudi friends at Georgia Tech. Special thanks to my dear friend, Motaz Alfarraj, the man I truly shared my journey with, we started together and we also finished together.

Finally, I cannot begin to express my thanks to my family for their prays and engorgement. In particular, my mother, aunts, uncles, and brothers. I am also grateful to my wife, Leena, for her endless support, the sacrifices she made throughout my journey, her patience with my unusual working hours, cheering me up when I am down, encouraging me when I am not motivated, and making my PhD her priority. Leena, without your support, my PhD would be impossible. My little angle, Norah, I cannot thank you for the joy and smile you bring on me. From the moment I knew that I will be your father, everything in my life becomes much easier.

TABLE OF CONTENTS

LIST OF TABLES

LIST OF FIGURES

LIST OF SYMBOLS AND ABBREVIATIONS

$(\cdot)^*$	The complex-conjugate operator.
$\|\cdot\|_x$	The ℓ_x norm operator. The default is $x = 2$.
$\lfloor x \rfloor$	The floor operator; maximum integer less than x.
$\boldsymbol{x}$	Denotes a vector $\boldsymbol{x}$.
$\tilde{\boldsymbol{x}}$	Denotes a complex vector $\tilde{\boldsymbol{x}}$.
$\underline{\mathbf{X}}$	Denotes a complex matrix $\underline{\mathbf{X}}$.
X	Denotes a random variable X.
λ	Free-space wavelength (m)
λ_m	Substrate wavelength (m)
Γ	The complex reflection coefficient.
Γ^*	The conjugate-matched reflection coefficient.
$\mathcal{CN}(0, \sigma^2)$	A complex, circularly-symmetric Gaussian random variable with 0 mean σ^2 standard deviation.
$E\{\cdot\}$	The mathematical expectation.
$\widetilde{\mathbf{E}}$	The complex vector time-harmonic electric field (V/m).
$\mathbb{Z}$	The set of integer numbers.
ϱ	The correlation coefficient.
ASIC	Application-specific integrated circuit.

BPSK	Binary phase-shift keying.
BW	Bandwidth.
CDF	Cumulative distribution function.
CW	Continues wave.
DFT	Discrete Fourier transform.
EIRP	Effective isotropic radiated power.
FCC	Federal Communications Commission.
IR	Ideal retrodirective.
ISM	Industrial, scientific, and medical band.
LoS	Line-of-sight geometry.
MRC	Maximal-ratio combining.
nLoS	Non-line-of-sight geometry.
OOK	ON-OFF Keying.
PAPR	Peak-to-average power ratio.
PCB	Printed circuit board
PDF	Probability density function.
POW	Power-optimized waveform.
QAM	Quadrature amplitude modulation.
QPSK	Quadrature phase shift keying.

RCS	Radar cross section (m^2). Also, denoted by σ.
RF	Radio frequency.
RFID	Radio-frequency Identification.
RLF	Retrodirectivity-loss factor.
RMS	Root mean square.
UHF	Ultra-high frequency.
SB	Standard backscatter.
SNR	Signal-to-noise ratio.
SOW	Standard one-way.
TEM	Transverse electromagnetic.
TWDP	Two-wave with diffuse power.
US	United States.
VNA	Vector Network Analyzer.

SUMMARY

Passive and semi-passive backscatter communication systems such as radio-frequency identification (RFID) experience several challenges that limit their proliferation especially at microwave and millimeter-wave (mm-wave) frequencies, a consequence from the round-trip and low-powered nature of these systems. These challenges manifest themselves in the forms of backscatter-communication range reduction, deep spatial nulls caused by the rapid change in the received power within a small area, or both. To overcome these challenges, a retrodirective-array-equipped backscatter transponder (an RFID tag) is used to replace the standard single-antenna transponder. The benefits of using retrodirective tags are twofold: First, since retrodirective tags that operate at microwave and mm-wave frequencies have similar propagation properties—in terms of power losses and field-of-view—to the current single-antenna RFID tags, which operate at ultra-high frequency (UHF) band, the higher-frequency retrodirective tags maintain the same coverage distance as the UHF tags and permit faster data rates by leveraging the spectrum availability at microwave and mm-wave regimes. Second, retrodirective tags reduce the randomness of the backscatter channel by changing the small-scale statistical behavior of the channel from double- to single-fading statistics, much like current one-way wireless channels—an original contribution of this research.

This work presents a compact, novel, and high spectral-efficiency microwave structure using a ring-based retrodirective array. Furthermore, this research investigates, theorizes, and measures the small-scale statistical characteristics of retrodirective backscatter channels. In fact, a two order of magnitude reduction in the channel fade margin is measured when a retrodirective tag replaces its single-antenna counterpart—a significant improvement in the reliability of the backscatter link. The analyses, results, and designs in this research are key enablers for next-generation microwave and mm-wave, ubiquitous, and power-free RFID and Internet-of-things (IoT) systems.

CHAPTER 1
INTRODUCTION

This chapter sheds some lights on the concept of contemporary low-power backscatter systems in general and radio-frequency identification (RFID) systems in particular. Therefore, the mathematical formulas and deep-physical theories are deferred to later chapters. Particularly, this chapter addresses the following points:

- An overview of the limitations in the current microwave and millimeter-wave (mm-wave) backscatter systems and the major role of this dissertation in overcoming these limitations.
- A brief history of backscatter communications.
- The frequency spectrum at which current and future backscatter systems can operate.
- The next-generation backscatter systems.
- The overall structure of this dissertation.

1.1 Overview

Current backscatter systems operate mainly in the industrial, scientific, and medical (ISM) ultra-high frequency (UHF) band; namely, at 915 MHz in the United states (US) since this band has a rather acceptable communication distance. However, since the received power is inversely proportional to the quadruple distance between the interrogator and transponder, the backscatter range is further reduced when higher frequencies—such as 5.8 GHz—are used for communications. Not only do backscatter systems in general and specifically at higher-frequencies suffer from reduced range, but they also experience severe fading caused by the pinhole (keyhole) nature of backscatter channels.

In the research literature, several solutions are proposed to tackle the two problems (range reduction and severe fading) independently. For instance, Griffin [1] showed theoretically and experimentally that deep fading nulls can be reduced with spatial diversity in

the transponder; that is, when the transponder uses two independently-signaled antennas. He also showed a significant reduction in the spatial nulls when two interrogators—in conjunction with the two-antenna transponder—applying the maximal-ratio combining (MRC) technique are used instead of a single interrogator.

On the other hand, Koo *et al.* [2] showed that when the transponder is equipped with a retrodirective array, an array in which the impinging electromagnetic waves are reflected back towards to the direction of incidence with maximal gain, the backscatter range increases. Not only does the array in [2] reflect the waves with maximal gain, but it also modulates the reflected waves using quadrature phase shift keying; therefore, both the backscatter range and spectral efficiency are increased. Another design that aims for increasing the backscatter range appeared in the work of Marshall [3], who proposed a beamforming antenna system that harvests power from all directions and backscatters that power towards the direction of incidence. Compared to the work of Koo *et al.* [2], Marshall's work [3] is more focused on maximizing the harvested energy for passive transponder rather than increasing the spectral efficiency.

The solutions in [1, 2, 3] have several limitations. In fact, all of the three solutions have a common factor; that is, the improvement in either fading reduction or communication range (along with spectral efficiency) requires an increase in the physical dimensions of backscatter systems. That is, the system in [2] requires variable-length transmission lines that modulate the backscattered signal. When the modulation order is increased, one of two problems arises: First, additional transmission lines are added to the system, which requires proper routing and consequently increasing the physical dimensions of the transponder. Second, when the operating frequency and modulation order are simultaneously increased, the fabrication tolerance becomes very small since the phases of those added transmission lines, which is a function of the transmission line electrical length, should be carefully chosen for better signal-to-noise ratio. In addition, the technique in [1] requires adding additional antennas on the transponder, having more than a single interrogator that are spatially apart to ensure that the interrogators are decorrelated, or both.

This dissertation addresses and proposes a novel solution to the limits associated with the proposed designs in [1] and [2]. That is, by using a ring-based retrodirective array on

the transponder, a performance similar to that in [2] is achieved but with a more compact size. Not only are the physical dimensions reduced, but also the spectral efficiency is increased while retraining a semi-fixed physical size. That is, the modulation order can be increased without changing the size of the transponder. Furthermore, the proposed system significantly reduces those deep nulls observed in [1] without the necessity of adding spatial diversity. In other words, a single, compact, and high spectral-efficiency transponder outperforms a bulky, diversity-leveraging system.

1.2 A Brief History of Backscatter Communications

Despite the devastation that world war II brought to humanity, it marked the first RFID system, known as the radar. Continuous post-war research efforts (much later) led to a commercial implementation of the RFID technology as an anti-theft system for merchandise [4]. With increased interest in RFID applications during the 1970s, Los Alamos scientists Alfred Koelle, Steven Depp, and Robert Freyman presented the very first RFID system that uses the concept of backscatter communications proposed by Stockman [5] two decades earlier, which occurs when the load of the tag antenna is varied [6]. In the 1980s, interest in backscatter-based RFID systems led to the adoption of RFID technology in railcar tracking and automated tolling systems [7]. However, the modern RFID system was not born until near the end of the 20th century, specifically in 1998 and 1999, when David Brock and Sanjay Sarma in Auto-ID centers at MIT [8] led efforts to introduce widespread UHF RFID in logistics. Since then, RFID technology has proliferated into applications in shipment tracking, baggage tracking [9][1], remote sensing, health monitoring, vehicle trolling, and many more.

In the 5.8-GHz ISM band, Joshua Griffin [1] led efforts in studying the communication aspects of backscatter systems. In particular, he studied the power link budget and fading characteristics of 5.8 GHz backscatter systems. In the realm of battery-free backscatter systems, Matthew Trotter [11] proposed the use of an FCC-compliant multi-tone signal that increases the peak-to-average power ratio (PAPR) of the interrogator transmitted sig-

[1] Aviation is a growing industry for RFID applications thanks to the International Air Transport Association (IATA) resolution 753 [10].

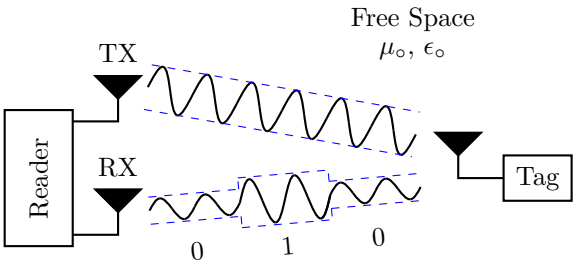

Figure 1.1: A generic structure of an RFID system (The figure is adapted from [14] © IEEE 2019)

nal, which in turn increases the conversion efficiency—the percentage of RF power that is converted to DC—of passive tags. The multi-tone signal, known as the power-optimized waveform (POW), overcomes the voltage-limit of the energy harvester by transmitting periodic bursts of a high-voltage waveform. On the other hand, the use of multi-antenna techniques at the transponder is shown in the work of Koo [2, 12] and Marshall [3]. The former replaced the transponder single-antenna system by a retrodirective array; thus, the reflected power by the transponder is always in the direction of the interrogator. However, the latter used a staggered pattern technique that steers the main lobe of the transponder towards multiple angles, which in turn increases the harvesting power efficiency.

1.3 A Concise Overview of RFID Technology

In an abstract way, RFID systems consist of two major subsystems: The reader (interrogator) and the tag (transponder) as depicted in Figure 1.1, which shows a reader sending uncoded signals and receiving modulated backscattered signals. The data exchange mechanism in Figure 1.1 is very common for testing and proof-of-concept analyses; however, in practice, the reader sends and receives modulated signal [13].

Changing the design of the reader and/or the tag would impact the overall system performance; therefore, the following subsections briefly discuss the available variants of the reader and tag, and pinpoint how choosing one design over others influences the overall system behavior.

1.3.1 Reader

The reader consists mainly of three parts: The antenna system,[2] the RF circuitry, and the baseband circuitry. Starting with the antenna system and referring to Figure 1.1, the relation between the transmitting (Tx) and receiving (Rx) antenna results in three RFID reader configurations [15]: Monostatic (same antenna system is used for transmitting and receiving), co-located bistatic (different antenna systems but they are spatially closed), and dislocated bistatic (different antenna systems but they are spatially farther apart). Choosing one of these configuration not only changes the system design, but it also changes the statistical properties of the backscatter channel.

In most cases, the antenna system in the reader consists of a single directive or semi-directive antenna such as [16]. Nonetheless, researchers have shown that with beam-steering arrays, the achievable communication range can be extended. For instance, Lee *et al.* [17] showed that by using a modified 4×4 Butler matrix as the reader antenna system, they achieved a 180° beam coverage with gain. Another design appeared in [18] in which the authors designed a 4×4 phased-array antenna system based on semi-circular patch antennas.

The RF and baseband circuitry of the reader are similar to most transceiver designs. One such example is given by [19]. However, backscatter communication adds two extra burdens to the system: First, the carrier frequency is considered a noise source and it can either saturate the receiver electronics or mask data signals that operate at low data rates. Second, the reader is more sensitive to the noise than a standard transceiver since the signal of interest is usually very weak as a result from the round-trip nature of backscatter communications.

1.3.2 Tag

The second major subsystem in Figure 1.1 is the RFID tag, which is considerably cheaper than the reader in commercial practice. In fact, tags can be as cheap as 7 US cents [20]. Structurally, passive tags usually consist of two parts: An antenna and an application-

[2]Throughout this work, the terms antenna and antenna system are used interchangeably. They both refer to the radiating system of the reader or tag whether it is a single antenna or an antenna array. However, to refer to a single antenna, we explicitly mention that the antenna is of a single-element type.

specific integrated circuit (ASIC). Semi-passive tags have external batteries (or energy sources such as solar cells [21, 22]) that power up the ASIC. In both cases, the tag communicates with the reader by changing the antenna impedance of the tag, which in turn changes the radar cross section (RCS) of the tag antenna. The relation between the antenna impedance and the RCS of the tag antenna is deferred to Chapter 2.

The design of the tag antenna is of great importance; in fact, the goal of this dissertation is to show that changing the tag antenna not only changes the tag read distance, but it also alters the backscatter channel statistics. Furthermore, when it comes to the selection of antenna tag type, most of UHF-based RFID tags use a variant of a meandered-dipole antenna [23]. Nevertheless, other types of antennas appeared in the research literature such as patch antennas [24, 25, 26] and Yagi-Uda antennas [27], to name a few. However, antenna arrays in UHF-based RFID tags are less common because of the large footprint of antennas at these frequencies.

1.4 RFID Frequency Spectrum

Most RFID systems operate in the unlicensed UHF band, which in general differs from one country to another. For instance, in the United States; the frequency range of the UHF band in the ISM radio bands—some of which are listed in Table 1.1—is from 902 MHz to 928 MHz, which spans a 26-MHz of bandwidth [28]. European countries, on the other hand, have the option to use either 862-870 MHz, 915-921 MHz, or both [29].

Operating at the UHF band has two major advantages: First, this band offers a tradeoff between antenna form-factor and backscatter read range. That is, a single antenna at both the reader and tag can be be used to communicate over relatively long distances with a small form-factor. Second, circuit simulation (a SPICE-based simulator yields acceptable results), fabrication (cheap substrate such as FR4 and matching circuits made from lumped elements), and testing are inexpensive in terms of time and cost. However, one key drawback of operating at UHF is that the bandwidth is narrow (26 MHz at 915 MHz compared to 150 MHz at 5.8 GHz [28]).

On the other hand, operating at frequencies higher then that of the UHF band comes

with both obstacles and promises. For one, the communication bandwidth increases with the increase in frequency. This increase has two benefits for RFID systems: First, data rate increases. Second, wider bandwidth allows a sufficient spectral gap between the carrier frequency and hardware noise, and the data frequency since—in the case of backscatter communications—the carrier frequency is considered a major source of noise [30].

Another major advantage of operating at frequencies beyond the UHF band is that the power received at the reader in line-of-sight (LoS) backscatter communications—ignoring the hardware losses at the tag—is in fact higher. To explain this phenomenon, recall that received power by any one-way wireless system has the following proportionality form:

$$\text{Power}_{\text{received}} \propto \text{Gain}_{\text{transmitter}}\ \text{Gain}_{\text{receiver}} \frac{(\text{Wavelength})^2}{(\text{Distance})^2}, \tag{1.1}$$

and the gain of the antenna also has the following proportionality form:

$$\text{Gain}_{\text{antenna}} \propto \frac{\text{Aperture Area}}{(\text{Wavelength})^2}. \tag{1.2}$$

Commonly, the antenna gain is fixed with the increase in frequency; therefore, the aperture area decreases, which results in a small form-factor antenna. However, if the aperture area is fixed, then the gain increases with the increase in frequency (decrease in the wavelength). Therefore, the received LoS power in the latter case increases by a factor of $1/(\text{Wavelength})^2$. Furthermore, the problem of atmospheric gas attenuation [31], which is critical for radar applications and recently becomes a big advantage for 5G cellular networks is negligible since RFID systems are considered short-range communication systems.

1.5 Next-Generation RFID Systems

Table 1.1 showed two major advantages for operating at frequencies beyond UHF: First, the available bandwidth increases, which enables either more channels per frequency band or transmission at faster data rates. Second, with the exception of the 2.4-GHz band, frequency bands become loosely regulated. These advantages in addition to researcher curiosities stimulate research and design of RFID systems that operate at frequencies beyond UHF.

Table 1.1: Comparison between ISM Bands in the US [28, 32, 33]

Frequency Band (GHz)	Bandwidth (MHz)	Maximum Hopping Channel Bandwidth	EIRP	Notes
$0.902 - 0.928$	26	At least 50 channels with $BW < 250$ kHz and 25 channels with $250 \leq BW \leq 500$ kHz. The separation between channels should be at least 25 kHz or one 20-dB BW, whichever greater.	36 dBm	Only frequency-hopping and digitally-modulated systems are allowed to operate
$2.400 - 2.500$	100	At least 15 channels. The separation between channels should be at least 25 kHz or one 20-dB BW, whichever greater. Also, a separation of 2/3 of the 20 dB BW with maximum power of 27 dBm is allowed	36 dBm if # of channels ≥ 75 and 27 dBm otherwise	Only frequency-hopping and digitally-modulated systems are allowed to operate
$5.725 - 5.875$	150	At least 75 channels with $BW \leq 1$ MHz	36 dBm	Only frequency-hopping and digitally-modulated systems are allowed to operate
$24.000 - 24.250$	250	Not specified in part 15	32.73 dBm	Information is taken from the field-strength limit
$60.000 - 64.500$	500	Not specified in part 15	40 dBm (average), 43 dBm (max)	-

Note: •BW stands for bandwidth

Therefore, a recent and growing interest in RFID systems that operate above UHF appeared in the research literature. For instance, Guidi *et al.* leveraged the loosely regulated 60-GHz ISM band to design a mm-wave based RFID system that outperforms a microwave-based ultra-wide band (UWB) system in terms of the number of pulses needed to achieve similar reader-tag read distance [34].

Current RFID systems may not benefit directly from the bandwidth increase since the UHF band provides an ample bandwidth for these low-rate applications. However, the long history of innovative research tells us that the availability of technologies can stimulate new kind of applications. For instance, without the invention of the laser, optical fiber communications would not exist. In fact, the co-inventor of the laser, Arthur Schawlow once said: *"We thought it [the laser] might have some communications and scientific uses, but we had no application in mind. If we had, it might have hampered us and not worked out as well"* [35]. Therefore, the relationship between technologies and applications is not always one way.

1.6 Dissertation Roadmap

The main focus of this dissertation is on backscatter systems—in general—and specifically RFID systems that operate at the 5.8-GHz ISM band. The results and analyses obtained in this work can be readily extended to RFID systems that operate at other frequency bands that are greater than 5.8 GHz. However, for frequencies below 5.8 GHz, the extension might not be practical because of the system physical dimensions, which is inversely proportional to the operating frequency.

This dissertation addresses two points: First, since retrodirective arrays play a pivotal role in backscatter systems operating at 5.8 GHz (or beyond), the type (or design) of retrodirective array should be chosen to minimize both the tag power consumption and physical dimension, and to increase the backscatter communication data throughput. Therefore, this dissertation investigates various retrodirective arrays and proposed selection criteria with which a system designer can choose the most suited design for the designer specific application. Second, this dissertation theorizes and measures the small-scale fading characteristics

when a standard single-antenna backscatter tag is replaced by a retrodirective tag.

Structurally, this dissertation is divided into seven chapters, which can be summarized as (excluding Chapter 1):

- Chapter 2 derives the electromagnetic theory of backscatter communications and how it relates to both the change in the tag antenna impedance and communication modulation schemes
- Chapter 3 reviews the statistical theory of backscatter communications assuming that the RFID tag is not equipped with a retrodirective array.
- Chapter 4 reviews the electromagnetic theory of retrodirective arrays in general and specifically derives the retrodirectivity conditions for the antenna arrays used in this work.
- Chapter 5 derives a new small-scale fading channel model for backscatter tags equipped with retrodirective arrays.
- Chapter 6 outlines and discusses the channel-sounding measurement campaign used to test the proposed theory in Chapter 5
- Chapter 7 draws a conclusion based on the analyses and results from the previous chapters. In addition, Chapter 7 discusses potential work that stems from this dissertation work.

Some of the aforementioned chapters have experiments associated with them; so, instead of dedicating a chapter for experiments (with the exception of Chapter 6), they are embedded within the chapters, which maintains context coherence.

CHAPTER 2
BACKSCATTER COMMUNICATIONS

Chapter 1 states that RFID tags communicate with RFID readers using a type of communications called *backscatter* communications. Although not explicitly stated, the word backscatter emphasizes two properties: First, tags are *controlled* scatterers. Second, communications become more reliable when the scattering electromagnetic waves are directed back towards the source of these waves, which is in most cases the RFID reader.

This chapter investigates various aspects of backscatter communications, which can be summarized as:

- The relationship between the scattering properties of antennas and the backscattered electric field. In particular, the dependence of the scattered electric field on the antenna load impedance.
- The modulation limit of passive and semi-passive backscatter systems.

2.1 From Scattering Theory to Communication Theory

The concept of backscatter communications appeared first in the work of Stockman [5], who showed that the modulated reflected microwave and optical power can be used to carry information. Therefore, as the title of that paper states, communications took place using the reflected power. The information coveyed by the reflected power is not limited to communication applications. In fact, one of the earliest applications of backscatter power is for field measurements [36, 37] in which the underlying concept is that the amount of scattered field from resonant objects is greater than that from non-resonant objects [36]. This concept is illustrated in Figure 2.1 in which the normalized radar cross section (RCS) of a short dipole is plotted for three cases: an open-circuit, a short-circuit, and a resonant load.

Modern backscatter systems rely on the theory of scattered field by the antenna, also

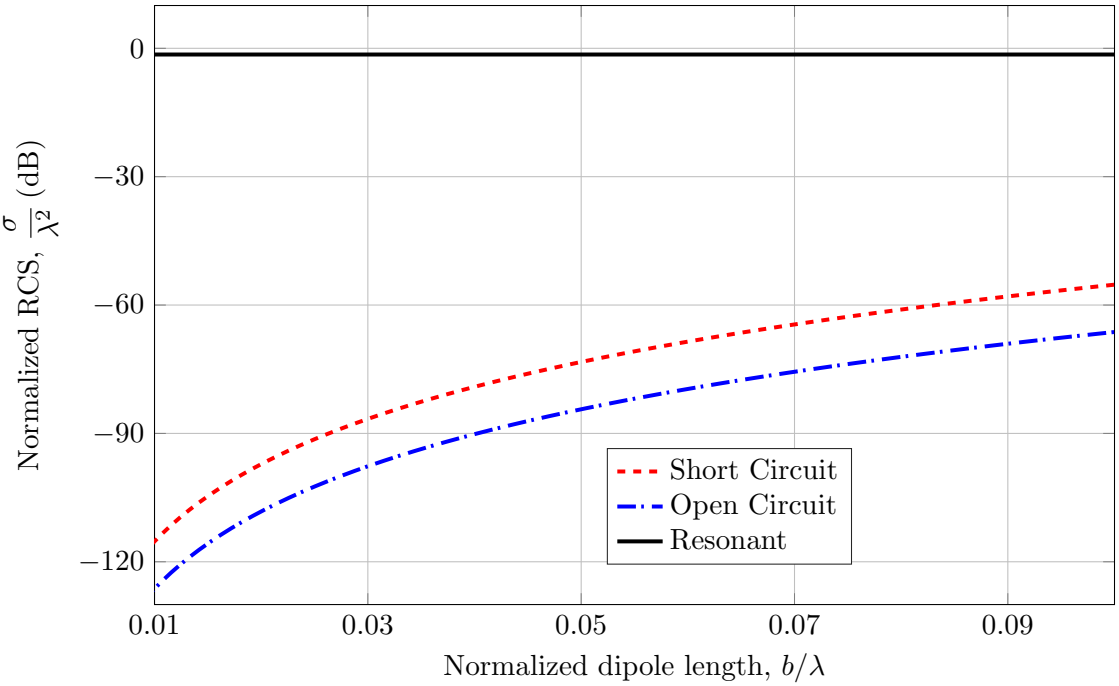

Figure 2.1: Normalized RCS for a short dipole of length b normalized by the wavelength. This figure is adapted from [36].

known as the theory of loaded scatterers. To illustrate this concept, consider the half-wave dipole in Figure 2.2 whose terminals are connected to an arbitrary load, Z_L, the scattered complex electrical field can be decomposed into two components [38]:

$$\widetilde{\mathbf{E}}(Z_L) = \underbrace{\widetilde{\mathbf{E}}(Z_a^*)}_{\text{structural mode}} + \underbrace{\Gamma^* I(Z_a^*)\,\widetilde{\mathbf{E}}_r}_{\text{antenna mode}}, \tag{2.1}$$

where:

$\widetilde{\mathbf{E}}(Z_L)$: is the scattered field as a function of the load impedance (V/m).

$\widetilde{\mathbf{E}}(Z_a^*)$: is the scattered field when the antenna is conjugate matched to the load (V/m). This field results from only the structure of the antenna.

$\widetilde{\mathbf{E}}_r$: is the radiated field form the antenna per unit current $(V/(m \cdot A))$.

Z_a: is the impedance of the antenna (Ω).

$I(Z_a^*)$: is the conjugate-matched current at the antenna terminal (A).

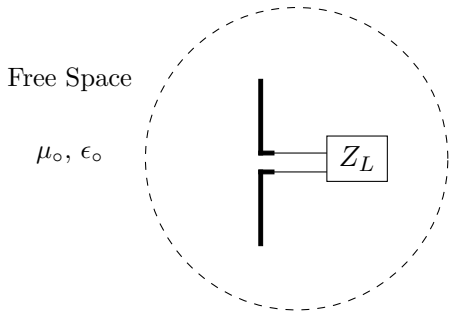

Figure 2.2: A half-wave dipole connected to an arbitrary load Z_L. The circular dashed area represents the starting points of a two-dimensional equivalent far-field area.

Γ^*: is the conjugate-matched reflection coefficient given by Equation (2.2) [39][1]

$$\Gamma^* = \frac{Z_a^* - Z_L}{Z_a^* + Z_L}. \tag{2.2}$$

The first part in Equation (2.1) represents the scattered electric field caused by the structure of the antenna and not by the fact that the antenna is actually a radiating element. This term carries no information other than the indication that the antenna exists, which is useful for detection and less useful for communications. The first term also exists for every value of Z_L. When this term is absent, the antenna is called a minimum scattering antenna [41, 42].

On the other hand, the second term in Equation (2.1) is directly related to the antenna terminating impedance. Therefore, it changes when the antenna impedance changes; hence, it can be used to backscatter information. To illustrate this with an example, consider the antenna in Figure 2.3 and assume $N = 2$; that is, two loads. The scattered electric field when the antenna is connected to Z_1 is

$$\widetilde{\mathbf{E}}\left(Z_1\right) = \widetilde{\mathbf{E}}\left(Z_a^*\right) + \Gamma_1^* I\left(Z_a^*\right) \widetilde{\mathbf{E}}_r, \tag{2.3}$$

[1] In [40], the authors use the negative of Equation (2.2); however, using either forms result in an identical differential RCS.

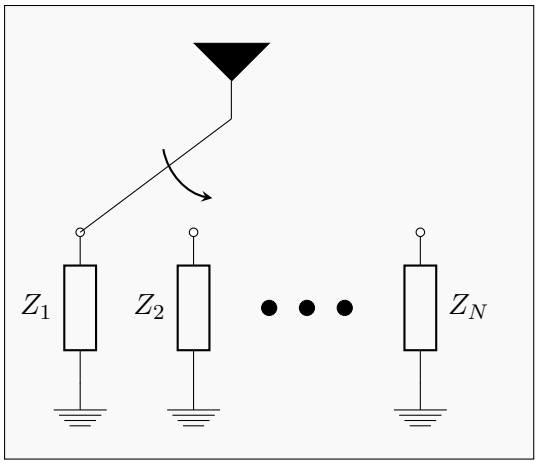

Figure 2.3: A simple RFID Tag. The tag antenna connects to N distinct impedance values, which changes the tag RCS.

and it is

$$\widetilde{\mathbf{E}}\left(Z_2\right) = \widetilde{\mathbf{E}}\left(Z_a^*\right) + \Gamma_2^* I\left(Z_a^*\right) \widetilde{\mathbf{E}}_r, \tag{2.4}$$

when the antenna is connected to Z_2, where $\Gamma_{1,2}^*$ are similar to Γ^* in Equation (2.2) but with Z_L is replaced by $Z_{1,2}$. If we plot Equations (2.3) and (2.4) in the complex plane and make the $\widetilde{\mathbf{E}}\left(Z_a^*\right)$ term as the plane center, we get Figure 2.4, which is akin to the binary phase-shift keying (BPSK) signal constellation. Therefore, by switching between distinct impedances, the tag communicates with reader.

In general, wireless propagation is characterized by variants of Friis transmission equation [43]. Since backscatter communication is akin to the radar problem, a radar-like range equation is used to specify the received power at the reader, which results from the backscattered power by the tag. In the radar literature, the power of the received echo, P_R, at the radar antenna is (assuming free-space propagation) [44]

$$P_R = \frac{P_T G_T^2 \lambda^2 \sigma}{(4\pi)^3 r^4}, \tag{2.5}$$

where:

P_T: is the transmitted power (W).

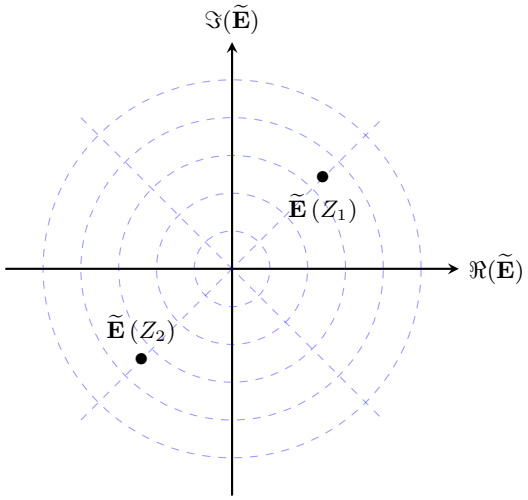

Figure 2.4: A complex-plane representation of the scattered field by an antenna. The plane center is set to the first term in Equations (2.3) and (2.4).

G_T: is the gain of the transmitting antenna, which is the receiving antenna.

λ: is the free-space wavelength (m).

σ: is the target RCS (m^2).

r: is the radial distance (m).

Equation (2.5), when the target is the RFID tag, is similar to that of backscatter communication power link-budget formula. However, the presence or absence of the tag in general does not convey useful information. Instead, the differential RCS is used.

To derive the differential RCS, $\Delta\sigma$, let us define the differential scattered electric field, $\widetilde{\mathbf{E}}_\Delta$, by subtracting Equation (2.4) from Equation (2.3), which yields

$$\widetilde{\mathbf{E}}_\Delta = \underbrace{(\Gamma_1^* - \Gamma_2^*)}_{A} \underbrace{I\,(Z_a^*)\,\widetilde{\mathbf{E}}_r}_{B}. \tag{2.6}$$

Term A is a function of the load and antenna impedances while term B is a linear function of the incident field, $\widetilde{\mathbf{E}}^i$, since it is the source of excitation and inversely proportional to

radial distance, r . In addition, recall that the RCS is defined as

$$\sigma = \lim_{r\to\infty} 4\pi r^2 \frac{\left\|\widetilde{\mathbf{E}}\right\|^2}{\left\|\widetilde{\mathbf{E}}^i\right\|^2}. \tag{2.7}$$

In the case of the differential field, $\widetilde{\mathbf{E}}_\Delta$, Equation (2.7) can be rewritten as [38]

$$\Delta\sigma = \lim_{r\to\infty} 4\pi r^2 \frac{\left\|\Gamma_1^* - \Gamma_2^*\right\|^2 \left\|I\left(Z_a^*\right)\widetilde{\mathbf{E}}_r\right\|^2}{\left\|\widetilde{\mathbf{E}}^i\right\|^2} \tag{2.8}$$

Since the scatterer in this case is an antenna, $\Delta\sigma$ can be defined in terms of the tag antenna gain, G_t [38, 45] ; that is,

$$\Delta\sigma = \xi\frac{\lambda^2}{4\pi} G_t^2 \left\|\Gamma_1^* - \Gamma_2^*\right\|^2 \tag{2.9}$$

where $0 \leq \xi \leq 1$, which accounts for aperture efficiency and polarization mismatch. Therefore, substituting Equation (2.9) into Equation (2.5) yields the monostatic free-space backscatter power link budget

$$P_R = \frac{P_T G_T^2 G_t^2 \lambda^4 \xi \left\|\Gamma_1^* - \Gamma_2^*\right\|^2}{(4\pi r)^4} = \frac{P_T G_T^2 G_t^2 \lambda^4 \xi M}{(4\pi r)^4}. \tag{2.10}$$

The bistatic case link budget is similar to that of the monostatic but G_T^2 is replaced by $G_T G_R$, where G_R is the gain of reader receiving antenna. Furthermore, term M is known as the modulation factor and can be written as

$$M = \frac{1}{4}\left\|\Gamma_1^* - \Gamma_2^*\right\|^2. \tag{2.11}$$

The value of M ranges between 0 and 1 for tags without amplifiers; however, when the tag is equipped with a reflection-type amplifier such as a tunnel diode [46]; M exceeds 1.

2.2 Backscatter Modulation

In Equation (2.11) of the previous section, the modulation factor sets an upper and lower limit on the maximum achievable range at fixed antenna gains and transmitted power. Often, backscatter systems utilize binary modulation such as on-off keying (OOK) or binary phase-shift keying (BPSK). The former is common amongst passive RFID tags that require a time interval for harvesting energy. To illustrate this concept, let us assume that one of the tag impedances (say Z_1) in Figure 2.3 is an energy harvesting circuitry such as those discussed in [47]. Therefore, the harvesting efficiency reaches its peak when $Z_1 = Z_a^*$. Solving for Γ^* in Equation (2.2) yields $\Gamma_1^* = 0$, which corresponds to a scatter electric field in the center of Figure 2.4. If the second impedance is a short circuit, then $\Gamma_2^* = 1$ and the modulation factor M in Equation (2.11) is equal to 0.25. On the other hand, BPSK is common amongst semi-passive tags in which one impedance is a short circuit ($\Gamma_1^* = 1$) and the other impedance is an open circuit, which results in $\Gamma_2^* = -1$; thus, the modulation factor is $M = 1$.

Moving beyond binary modulation requires re-defining the modulation factor M to account for more than two states. Therefore, M is defined as

$$M = \min \left\{ \frac{1}{4} \left\| \Gamma_i^* - \Gamma_j^* \right\|^2 \right\}, \quad \forall i \neq j \text{ and } i, j = 1, \ldots, N. \tag{2.12}$$

Unlike other forms of communications, the energy in the constellation diagram is set by the maximum value of $\|\Gamma_i^*\|$, which is 1 for tags without reflection amplifiers. That is, the constellation points—in terms of Γ^*—should lie within a unit circle in the complex plane. This limit has a direct implication on the maximum distance between modulation states, which is related to the signal-to-noise-ratio (SNR). In other words, when the distance between the constellation points decreases, the SNR decreases. To better illustrate this implications, let us assume that we have a tag with a fixed antenna gain, G_t, and can connect to one of L single-pole m-throw switches (SPmT), where m is the number of modulation states. If the reader is sending the same power for all L cases, then the SNR—under m-ary phase-shift keying (PSK)—decreases by a factor of $4\sin^2(\pi/m)$ [48]. This reduction

is plotted in Figure 2.5, which shows that increasing the modulation order above $m = 4$ is not practical. Similarly, the SNR reduction can be observed if m-quadrature amplitude modulation (QAM) is used. In this case, the SNR reduces by a factor of $1/(\log_2(m) - 1)^2$. This reduction is also plotted in Figure 2.5.

The RFID literature has some theoretical, experimental, and simulation-based implementations of non-binary modulation. For instance, Thomas *et al.* [49] experimentally showed that 4 QAM can be implemented with various inductor-capacitor combinations. A later implementation by the same authors appeared in [50] in which they experimentally tested a 16-QAM semi-passive RFID tag. In addition, Boyer and Roy [51] discussed—theoretically—the advantage of having coded QAM. Furthermore, Ebrahimi-Asl *et al.*[52] showed that when a T-match bow-tie antenna is used instead of a half-wave dipole, a quasi 32-QAM can be implemented.

In practise, RFID systems do not have a pure OOK modulation for two reasons: First, finding an exact matching state is near impossible since some electric field backscatters when the the antenna is imperfectly matched to the load. Second, a pure OOK requires a non-zero mean baseband signal. However, RFID readers usually have DC blocks mainly for blocking the unmodulated carrier frequency. Therefore, the mean of the baseband signal is usually removed. As an example, we conducted two experiments, one of which the tag implements OOK modulation while it implements BPSK in the second experiment. We used the setup in Chapter 4 with 1 MHz square wave. In the OOK experiment, the tag connects to an RF switch (ZFSWA2-63DR+) whose outputs are terminated with a short-circuit and 50-Ω load. However, the tag in the BPSK experiment connects also to the same RF switch but the outputs of the switch are terminated with an open- and short-circuit load. The signal constellations of these experiments are shown in Figure 2.6, which shows that both OOK and BPSK have zero mean but the distance between the constellation points is approximately doubled in the latter compared to the former.

2.3 Chapter Summary

This chapter focused on several aspects of backscatter communications. The take away points from this chapter are:

- The scattered electric field by an antenna has two components: Structural, which depends on the structure of the antenna, and antenna-mode, which is a function of the antenna impedance. The structural part is mainly responsible for determining the presence or absence of the antenna and has limited use in communications. On the other hand, the antenna-mode scattered electric field can be utilized for data exchange.

- The differential RCS of the RFID tag, which results from the differential scattered electric field, is a function of the antenna gain, frequency, and more importantly, the modulation. The dependence on the modulation is characterized by the the modulation factor, M, which in general has an upper limit of one. The limit is approached when the tag switches between an open- and short-circuit load. However, the modulation factor can be greater than one if a reflection-type amplifier is used on the tag.

- RFID tags without reflection amplifiers have a tradeoff between the spectral efficiency and SNR. That is, increasing the spectral efficiency comes at the price of decreasing the SNR. A reasonable compromise design is to use either QPSK or 4QAM.

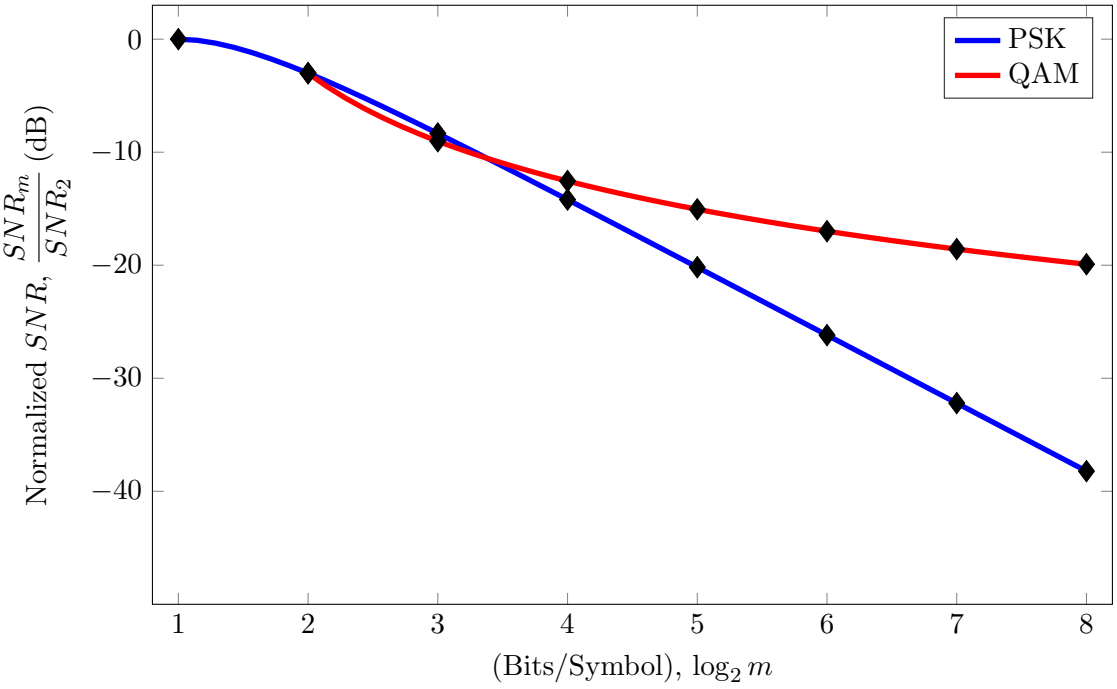

Figure 2.5: Normalized Reduction is the SNR per modulation order for uncoded m-ary PSK and QAM. The normalization is with respect to the SNR when $m = 2$.

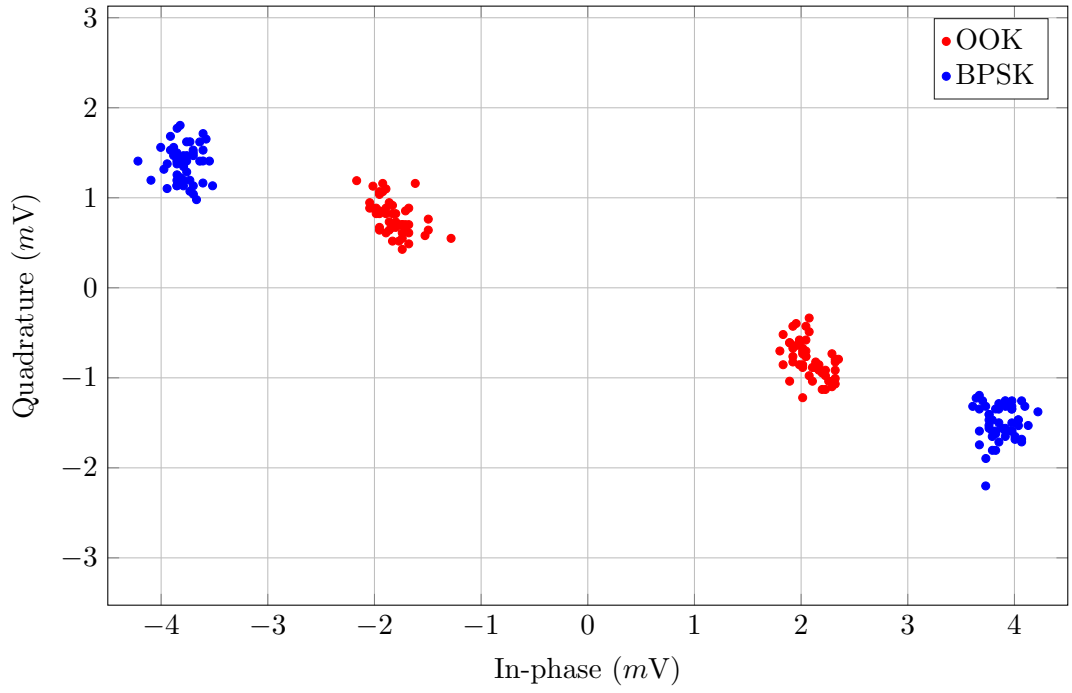

Figure 2.6: Measured IQ signal constellation for an RFID tag using two modulation schemes: OOK and BPSK.

CHAPTER 3
BACKSCATTER CHANNELS

In the previous chapter, several aspects of backscatter communications are discussed. This chapter tackles the operation of backscatter systems in multipath environments. Understanding the operation of these systems requires a deep understanding of the electromagnetic wave behavior in multipath scenarios. Therefore, this chapter is dedicated to reviewing the basic physical and statistical properties of multipath propagation. In particular, this chapter addresses the following points:

- The general mathematical form of multipath electromagnetic waves along with the simplified form.
- The stochastic models of special backscatter channels.
- The bounded performance of general backscatter channels.

3.1 Wireless Systems in Realistic Environments

In typical wireless scenarios, the total far-field complex electric field impinges upon the receiving antenna is a combination of many complex-weighted electric field components having the following form [53]:

$$\widetilde{\mathbf{E}}(f,t,\boldsymbol{r}) = \sum_{i=1}^{N} \mathbf{E}\left(f,t,\boldsymbol{r},L_i\right) \exp\left[-j\left(\Phi_i + \boldsymbol{k}_i\cdot\boldsymbol{r} + 2\pi(f+f_c)\left(\tau_i + \frac{v_i}{c}t\right)\right)\right]\hat{\boldsymbol{e}}_i, \qquad (3.1)$$

where:

- L_i: is the overall traveled path of the i^{th} multipath component as in Figure 3.1. This distance impacts the magnitude of the electric field since it is inversely proportional to the distance, L_i. In addition, using the distance, we define the delay of the i^{th} component; that is, $\tau_i = L_i/c$, where c is the free-space speed of light.
- $\boldsymbol{k}_i$: is the i^{th} multipath wavevector. In free space, $\|\boldsymbol{k}_i\| = (2\pi/\lambda_i)$. The direction of $\boldsymbol{k}_i$ depends on the the polarization of the wave and its interaction with scartterers in

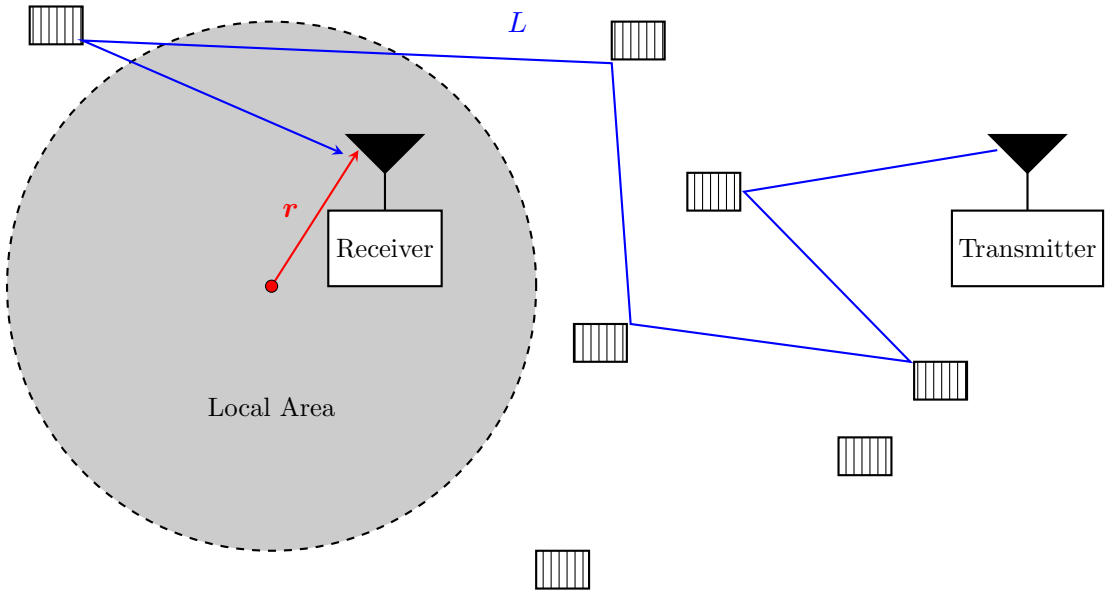

Figure 3.1: Illustration of multipath propagation. The hashed rectangles are scatterers.

the scene. However, Since Equation (3.1) has a non-zero bandwidth, a useful way to write $\boldsymbol{k}_i$ is in terms of bandwidth; that is, $\boldsymbol{k}_i = 2\pi(f + f_c)/c\ \hat{\boldsymbol{k}}_i$, where $\hat{\boldsymbol{k}}_i$ is the unit vector in the direction of $\boldsymbol{k}_i$.

- v_i: is the velocity of the i^{th} scatterer. The sign and the value of v_i depend on the direction and speed of motion, respectively.
- $\hat{\boldsymbol{e}}_i$: represents the polarization of the electric field. In practise $\hat{\boldsymbol{e}}_i = a_i\hat{\theta} + b_i\hat{\phi}$ such that $\|\hat{\boldsymbol{e}}_i\| = 1$.
- Φ_i is a random phase results from various processes such as transmitter frequency synthesizer, power amplifier, to name a few.

In reality, studying individual multipath components is cumbersome and impractical. A useful way is to define a stochastic local area channel (SLAC) [53] akin to the shaded circle in Figure 3.1. Within this area, the electric field components in Equation (3.1) are assumed to result from homogeneous plane waves that have constant magnitude and constant phase front; that is, $\mathbf{E}\left(f, t, \boldsymbol{r}, L_i\right) \longrightarrow E_i$.

The phase component in Equation (3.1), however, is a bit complicated and necessitates careful analyses. First, when the scatterers are stationary or slowly moving with respect to the communication time so the channel appears to be stationary, then $v_i = 0$ and the time

dependence is eliminated. In addition, when the communication bandwidth is below the channel coherence bandwidth—defined as the bandwidth at which the channel frequency response is constant—then the term $2\pi(f+f_c)\tau_i \longrightarrow 0$. For example, the reported coherence bandwidth at 5.8 GHz is 9.6 MHz for an LoS geometry and 4 MHz for an obstructed LoS geometry [54]. Finally, the term $\boldsymbol{k}_i \cdot \boldsymbol{r}$ can be expressed as [53]

$$\boldsymbol{k}_i \cdot \boldsymbol{r} = \frac{2\pi\left(f_c + f\right)}{c}\hat{\boldsymbol{k}}_i \cdot \boldsymbol{r} = \underbrace{\frac{2\pi f_c}{c}\hat{\boldsymbol{k}}_i \cdot \boldsymbol{r}}_{\text{Spatial term}} + \underbrace{\frac{2\pi f}{c}\hat{\boldsymbol{k}}_i \cdot \boldsymbol{r}}_{\text{Spatio-frequency term}} . \tag{3.2}$$

The spatio-frequency term becomes insignificant when the following condition is satisfied [53]:

$$L_A \leq \frac{f_c}{BW}\lambda, \tag{3.3}$$

where BW is the signal bandwidth and L_A is the local area size. In this work, we assume that the size of the local area satisfies the condition in Equation (3.3).

With the previous simplifications, Equation (3.1) may rewritten as

$$\widetilde{\mathbf{E}}(\boldsymbol{r}) = \sum_{i=1}^{N} E_i \exp\left[-j\left(\Phi_i + \boldsymbol{k}_i \cdot \boldsymbol{r}\right)\right]\hat{\boldsymbol{e}}_i. \tag{3.4}$$

Although simple compared to Equation (3.1), Equation (3.4) is a two-dimensional equation with respect to wave polarization and a three-dimensional equation with respect to the spatial location. Therefore, we simplify it further by considering only the radial dimension; that is, $\boldsymbol{r} = (r, \theta, \phi) \longrightarrow r$, where θ and ϕ, are the elevation and azimuth angle, respectively. This simplification is equivalent to the dot product of the received electric field, Equation (3.4), with the antenna pattern factor, $\boldsymbol{p}(\theta, \phi)$, [53, 55, 56]. The result of this product is the open-circuit voltage, V_{oc} at the antenna terminals; mathematically,

$$V_{oc} = \widetilde{\mathbf{E}}(\theta, \phi) \cdot \boldsymbol{p}^*(\theta, \phi). \tag{3.5}$$

Therefore, we can rewrite Equation (3.4) as [53]

$$V_{\text{oc}}(r) = \sum_{i=1}^{N} V_i \exp\left(j\Phi_i\right), \tag{3.6}$$

where the simplified form of the term $\boldsymbol{k}_i \cdot \boldsymbol{r}$ is lumped with the Φ_i term along with dropping the negative sign. This process is just to make Equation (3.6) and the subsequent equations mathematically compact.

Equation (3.6) is the key equation for the subsequent analyses since it conveys all of the multipath information needed to study the envelope distribution of the received voltage. In addition, Equation (3.6) can be modeled as a complex random variable, $Z = X + jY = P\angle\Phi$. The nature of this random variable is what this chapter intends to study.

The first step in analyzing the random variable Z in Equation (3.6) is to notice that it can be divided into the sum of random components; that is,

$$V_{\text{oc}}(r) = Z = \sum_{i=1}^{N} Z_i, \tag{3.7}$$

where the phase of each Z_i is uniformly distributed on $[0, 2\pi)$. The magnitude V_i can be either deterministic or random. However, only the multipath component that has a variance $2\sigma_i^2$ that is comparable to the variance of the random variable Z, which is $2\sigma^2$, has an impact on the distribution of Z [57]. In this dissertation, we only consider the case when at most one component has a variance that is comparable to that of the total sum (i.e. one component with $2\sigma_i^2$ that is comparable to $2\sigma^2$). In particular, this dissertation is interested in the following random variable [53]:

$$V_{\text{oc}}(r) = \underbrace{V_1 \exp\left(j\Phi_1\right)}_{\text{Specular}} + \underbrace{\sum_{i=2}^{N} V_i \exp\left(j\Phi_i\right)}_{\text{Diffuse}} = V_1 \exp\left(j\Phi_1\right) + \mathcal{CN}\left(0, 2\sigma^2\right) \tag{3.8}$$

which is known as a uniformly distributed phasor plus a Rayleigh random variable [57].

The envelope of this random variable has a Rician distribution; that is,

$$f(\rho) = \frac{\rho}{\sigma^2} \exp\left(\frac{-\rho^2}{2\sigma^2} - K\right) I_0\left(\frac{\rho\sqrt{2K}}{\sigma}\right), \tag{3.9}$$

where $I_0(\cdot)$ is the zeroth order modified Bessel function of the first kind and K is the Rician K-factor, defined as

$$K = \frac{\text{Specular Power}}{\text{Diffuse Power}} = \frac{V_1^2}{2\sigma^2}. \tag{3.10}$$

In the absence of the specular component, the envelope is reduced to a Rayleigh distribution. In other words,

$$f(\rho) = \frac{\rho}{\sigma^2} \exp\left(\frac{-\rho^2}{2\sigma^2}\right). \tag{3.11}$$

In the literature, the random variable Z in Equation (3.7) is often assumed to be a complex Gaussian random variable with non-zero mean. However, in this dissertation, we followed the assumption in [53], which results in a completely different random variable. If Z is a complex Gaussian, then Z is not circularly symmetric and the use of Hankel transform is not permissible [53, 58, 59]. Although both assumptions result in the same envelope distribution, the latter is more generic and realistic. In fact, the phase randomness of the specular component captures some drastic effects such as the cancellation of the specular power in the case of two-wave with diffuse power (TWDP) [60].

Although the previous analyses are drawn mainly from [53], re-presenting the fundamental concepts is critical for better understanding of the subsequent analyses—specifically, in Chapter 5—that pertain to fading in retrodirective channels. In these channels, the physics of multipath propagation is a key factor for simplifying the derivations of the channel stochastic model.

3.2 Backscattering in Multipath Scenarios

Backscatter systems are two-way communication systems. The first link is from the reader to the tag, which is called the forward link or downlink. The second link is from the tag to

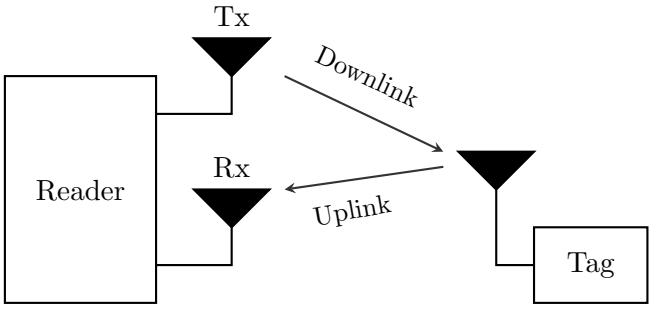

Figure 3.2: A generic RFID system. The tag antenna can be either a single element or an array.

the reader, which is called the backward link or uplink. These links are shown in Figure 3.2.

To study the envelope statistics of the received signal at the receiving antenna of the reader, we make the following cosmetic changes to Equation (3.6):

$$V_{\text{oc}}(r) \longrightarrow V_x(r), \tag{3.12}$$

$$V_i \longrightarrow \beta_i. \tag{3.13}$$

where x is either T when we refer to the voltage at the tag or R when when we refer to the voltage at the reader. Now, the open circuit voltage at the tag antenna is similar to Equation (3.6); that is,

$$V_T = \sum_{i=1}^{N} \beta_i \exp(j\Phi_i) \sim Z_f. \tag{3.14}$$

The backscattered voltage at the reader receiving antenna is given by

$$V_R = \sum_{\ell=1}^{L} \alpha_\ell \exp(j\Psi_\ell) V_T \sim Z_b V_T. \tag{3.15}$$

Effectively, the received voltage at the reader can be rewritten as

$$V_R = \left(\sum_{\ell=1}^{L} \alpha_\ell \exp(j\Psi_\ell) \right) \left(\sum_{i=1}^{N} \beta_i \exp(j\Phi_i) \right) \sim Z = Z_b Z_f. \tag{3.16}$$

Therefore, studying spatial fading in backscatter channels is equivalent to studying the

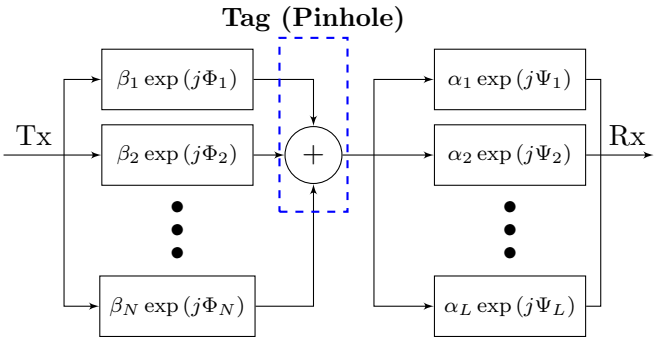

Figure 3.3: A signal-flow graph for backscatter channels (The figure is adapted from [14], © IEEE 2019).

distribution of the random variable Z in Equation (3.16). The nature of this random variable Z depends on the nature of Z_f and Z_b along with the RFID system configurations [15]. Overall, we have three major categories of Z each of which corresponds to a different RFID system configuration.

A graphical and descriptive way of representing backscatter channels—or equivalently, Equation (3.16)—is by using the signal-flow diagram in Figure 3.3. The tag in backscatter systems behaves akin to a pinhole (keyhole) in which multipath components converge. This behavior has a drastic impact on the link quality of these channels. One way to mitigate this behavior is by introducing spatial diversity in the reader and tag [61].

3.2.1 Monostatic Channels

In this configuration, we use the same antenna for transmitting and receiving at the reader. Therefore, the forward and backward channels are fully correlated ($\varrho = 1$) since they are essentially identical. Mathematically, the received voltage at the reader is given by

$$V_R = \left(\sum_{i=1}^{N} \beta_i \exp(j\Phi_i) \right)^2 \sim Z = Z_f^2. \tag{3.17}$$

The envelope distributions of Z for LoS (the underlying channel is Rician) and nLoS (the underlying channel is Rayleigh) are listed in Table 3.1. These distributions can be easily derived using that fact that the envelope PDF, P, is defined as P_f^2, where P_f is the forward

channel envelope PDF.

For the monostatic case, we can also derive the Rician K-factor [62, 14]. We can re-arrange Equation (3.17) as

$$V_R(r) = \left(\beta_1 \exp\left(j\Phi_1\right) + \sum_{i=2}^{N} \beta_i \exp\left(j\Phi_n\right) \right)^2 = \beta_1^2 \exp\left(2j\Phi_1\right) + \mathcal{A}, \tag{3.18}$$

where $\mathcal{A}$ is the lumped sum of the remaining $(N^2 + N - 2)/2$ terms that result from the multinomial expansion. The root mean square (RMS) power is given by

$$\begin{aligned} \rho_{\text{rms}}^2 = E\{|V(r)|^2\} &= E\{\left(\beta_1^2 \exp\left(2j\Phi_1\right) + \mathcal{A}\right) \ \left(\beta_1^2 \exp\left(-2j\Phi_1\right) + \mathcal{A}^*\right)\} \\ &= \underbrace{\beta_1^4}_{\text{Specular}} + \underbrace{\beta_1^2 E\{\exp\left(2j\Phi_1\right)\mathcal{A}^* + \exp\left(-2j\Phi_1\right)\mathcal{A}\} + E\{\mathcal{A}\mathcal{A}^*\}}_{\text{Diffuse}}, \end{aligned} \tag{3.19}$$

where $E\{\cdot\}$ is the mathematical expectation. Therefore, we can rewrite the K-factor ratio in Equation (3.10) as

$$K_{\text{mono}} = \frac{\beta_1^4}{\rho_{\text{rms}}^2 - \beta_1^4}. \tag{3.20}$$

To find ρ_{rms}^2, we solve the following integral:

$$\rho_{\text{rms}}^2 = \int_0^\infty \rho^2 \frac{1}{2\sigma^2} \exp\left(\frac{-\rho}{2\sigma^2} - K\right) I_0\left(\frac{\sqrt{2K\rho}}{\sigma}\right) d\rho, \tag{3.21}$$

which resembles the following integral:

$$\rho_{\text{rms}}^2 = \gamma \int_0^\infty \rho^{\mu - \frac{1}{2}} \exp\left(-\alpha\rho\right) I_{2\nu}\left(2b\sqrt{\rho}\right) \mathrm{d}\rho \tag{3.22}$$

with $\mu = 5/2$, $\nu = 0$, $\alpha = 1/(2\sigma^2)$, $b = \sqrt{K}/(\sqrt{2}\sigma)$ and $\gamma = \exp\left(-K\right)/(2\sigma^2)$. The solution to the integral in Equation (3.22) is ([6.643.2 pp. 716] in [63])

$$\rho_{\text{rms}}^2 = \frac{2\gamma}{b} \exp\left(\frac{b^2}{2\alpha}\right) \alpha^{-5/2} M_{-5/2,0}\left(\frac{b^2}{\alpha}\right), \tag{3.23}$$

Table 3.1: PDF's of double Rayleigh and Rician [1, 62] ($\varrho = 1$)

Underlying Channel	PDF of Z_f	PDF of Z	PDF plot
Rayleigh	$f(\rho) = \frac{\rho}{\sigma^2}\exp\left(-\frac{\rho^2}{2\sigma^2}\right)$	$f(\rho) = \frac{1}{2\sigma^2}\exp\left(-\frac{\rho}{2\sigma^2}\right)$	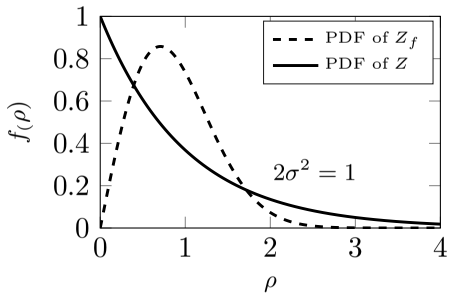
Rician	$f(\rho) = \frac{\rho}{\sigma^2}\exp\left(\frac{-\rho^2}{2\sigma^2} - K\right) I_0\left(\frac{\rho\sqrt{2K}}{\sigma}\right)$	$f(\rho) = \frac{1}{2\sigma^2}\exp\left(\frac{-\rho}{2\sigma^2} - K\right) I_0\left(\frac{\sqrt{2K\rho}}{\sigma}\right)$	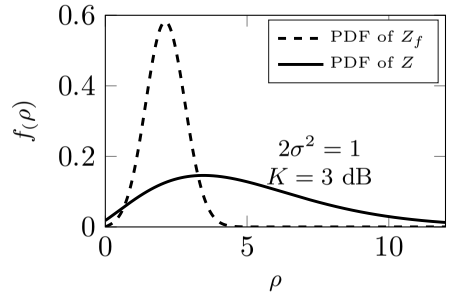

where $M_{\lambda,\eta}(x)$ is the Whittaker function, which is related to the confluent hypergeometric function of the first kind, ${}_1F_1\left(a;b;x\right)$, using the following identity ([9220.2 pp. 716] in [63]):

$$M_{\lambda,\eta}(x) = x^{\eta+\frac{1}{2}} \exp\left(-\frac{x}{2}\right) {}_1F_1\left(\eta-\lambda+\frac{1}{2};2\eta+1;x\right). \tag{3.24}$$

Therefore,

$$\rho_{\text{rms}}^2 = 8\sigma^4 \exp\left(-K\right) {}_1F_1\left(3;1;K\right). \tag{3.25}$$

The last step is to write β_1 in terms of K and σ; that is,

$$\beta_1 = \sigma\sqrt{2K}. \tag{3.26}$$

Therefore, substituting Equations (3.25) and (3.26) into Equation (3.20) yields a monostatic K-factor of the following form:

$$K_{\text{mono}} = \frac{K^2}{2\exp\left(-K\right) {}_1F_1\left(3;1;K\right) - K^2}. \tag{3.27}$$

The relationship between the monostatic Rician K-factor of a backscatter channel and that of its underlying one-way Rician channel is plotted in Figure 3.4. In the logarithmic scale, Figure 3.4 shows an approximate 8 dB difference between K and K_{mono}.

3.2.2 Dislocated Bistatic Channels

In this case, not only the reader receiving antenna is different from the transmitting antenna, but they are also spatially apart. That is, we can assume the forward and backward channels are independent and hence; decorrelated ($\varrho = 0$). The separation distance at which the two channels are decorrelated is deferred to Chapter 6.

To derive the envelope statistics of the decorrelated channels, we start with the voltage at the reader receiving antenna. This voltage is similar to Equation (3.16) and the resulting random variable, Z, is a product of two *independent* random variables, Z_f and Z_b. Although Z_f and Z_b can be any two random variables that are physically possible, we only consider

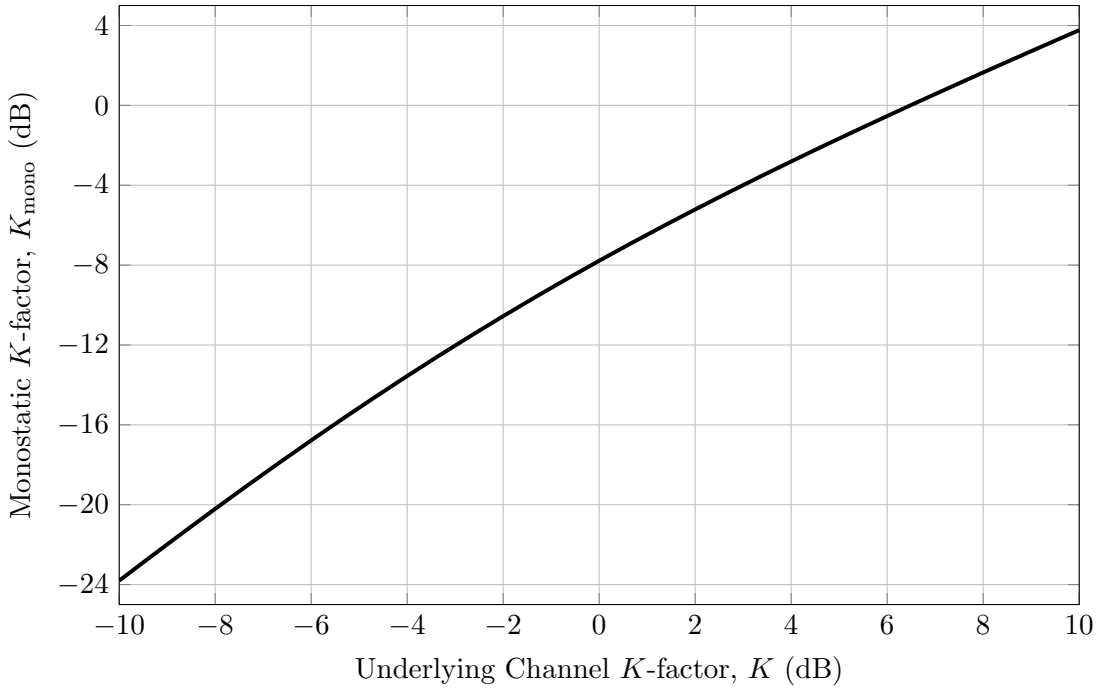

Figure 3.4: The monostatic Rician K-factor, K_{mono} versus the underlying channel K-factor (This figure is adapted from [62], © IEEE 2019)

the case when Z_f and Z_b have the same distribution but with different moments. With such restriction, the envelope distributions of Z for LoS (the underlying channel is Rician) and nLoS (the underlying channel is Rayleigh) are listed in Table 3.2

3.2.3 Co-located Bistatic Channels

In the case of co-located bistatic configuration, the reader transmitting antenna is different from the receiving antenna but they are spatially closed. Therefore, the forward and backward channels are correlated; that is, $0 < \varrho < 1$. However, finding a closed form expression for such distributions is not always feasible especially for LoS propagation in which the underlying channels are Rician. In the case of nLoS, however, the envelope distribution is given by [64]

$$f(\rho) = \frac{\rho}{\sigma_f^2 \sigma_b^2} I_0\left(\frac{\rho\,|\varrho|}{\sigma_f \sigma_b (1-\varrho^2)}\right) K_0\left(\frac{\rho}{\sigma_f \sigma_b (1-\varrho^2)}\right). \tag{3.28}$$

Table 3.2: PDF's of double Rayleigh and Rician [64, 1, 62] ($\varrho = 0$)

Underlying Channel	PDF's of Z_f and Z_b	PDF of Z	PDF plot
Rayleigh	$f_f(\rho) = \frac{\rho}{\sigma_f^2}\exp\left(-\frac{\rho^2}{2\sigma_f^2}\right)$, $f_b(\rho) = \frac{\rho}{\sigma_b^2}\exp\left(-\frac{\rho^2}{2\sigma_b^2}\right)$	$f(\rho) = \frac{\rho}{\sigma_f^2\sigma_b^2}K_0\left(\frac{\rho}{\sigma_f\sigma_b}\right)$	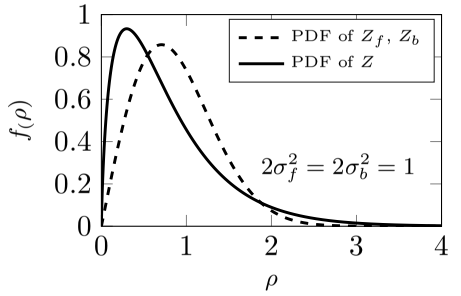
Rician	$f_f(\rho) = \frac{\rho}{\sigma_f^2}\exp\left(\frac{-\rho^2}{2\sigma_f^2} - K_f\right)I_0\left(\frac{\rho\sqrt{2K_f}}{\sigma_f}\right)$, $f_b(\rho) = \frac{\rho}{\sigma_b^2}\exp\left(\frac{-\rho^2}{2\sigma_b^2} - K_b\right)I_0\left(\frac{\rho\sqrt{2K_b}}{\sigma_b}\right)$	$f(\rho) = \frac{1}{\sigma_f^2\sigma_b^2}\exp\left(-K_f - K_b\right)\times \sum_{i=0}^{\infty}\sum_{\ell=0}^{\infty}\frac{1}{i!\ell!\Gamma(i+1)\Gamma(\ell+1)}\times \left(\frac{K_f}{2\sigma_f^2}\right)^i\left(\frac{K_b}{2\sigma_b^2}\right)^\ell\left(\frac{\sigma_f}{\sigma_b}\right)^{i-\ell}\times \rho^{1+i+\ell}K_{i-\ell}\left(\frac{\rho}{\sigma_f\sigma_b}\right)$	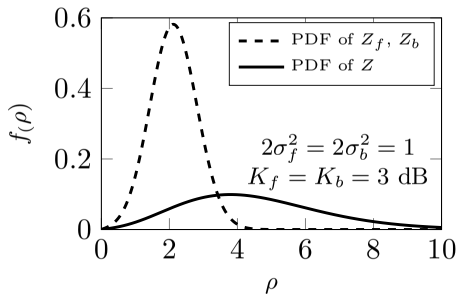

Notes: •$K_0(\cdot)$ is the modified zeroth order Bessel function of the second kind. •$\Gamma(\cdot)$ is the gamma function.
•$(\cdot)!$ is the factorial operator.

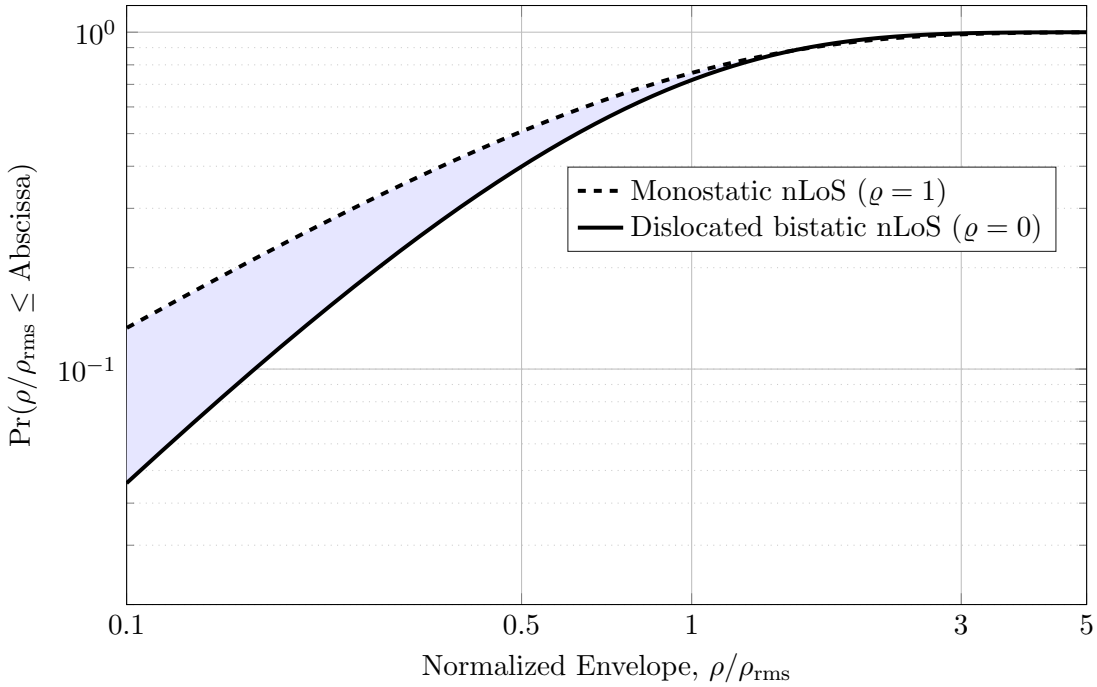

Figure 3.5: Bounded CDF for a product-Rayleigh distribution (nLoS propagation). The shaded area represents the possible locations for the CDF of correlated channels.

3.3 A Better Way to Study Correlated Channels

In the previous section, the case of correlated forward and backward channels does not always yield a simple intuitive distribution. Therefore, it might be practical to study the bounded performance of backscatter systems. In the research literature, fading—in space and time—worsens with correlation as proven by Griffin and Durgin [65], and Arnitz *et al.* [66]. Therefore, the best case scenario is when the forward and backward channels are decorrelated ($\varrho = 0$) while the worst case scenario is when these channels are fully correlated ($\varrho = 1$). Using this information, Figures 3.5 and 3.6 plot an upper and lower bound on the cumulative distribution function (CDF) for the nLoS and LoS geometry, respectively.

The bounded behavior is true for any metric that depends on the PDF. For instance, we can derive and plot the bounded behavior using the average bit-error-rate (BER) as a function of the SNR, which is defined as [67]

$$P_b(\bar{\gamma}) = \int_0^\infty P_{\text{AWGN}}(\gamma) f(\gamma)\, \mathrm{d}\gamma, \tag{3.29}$$

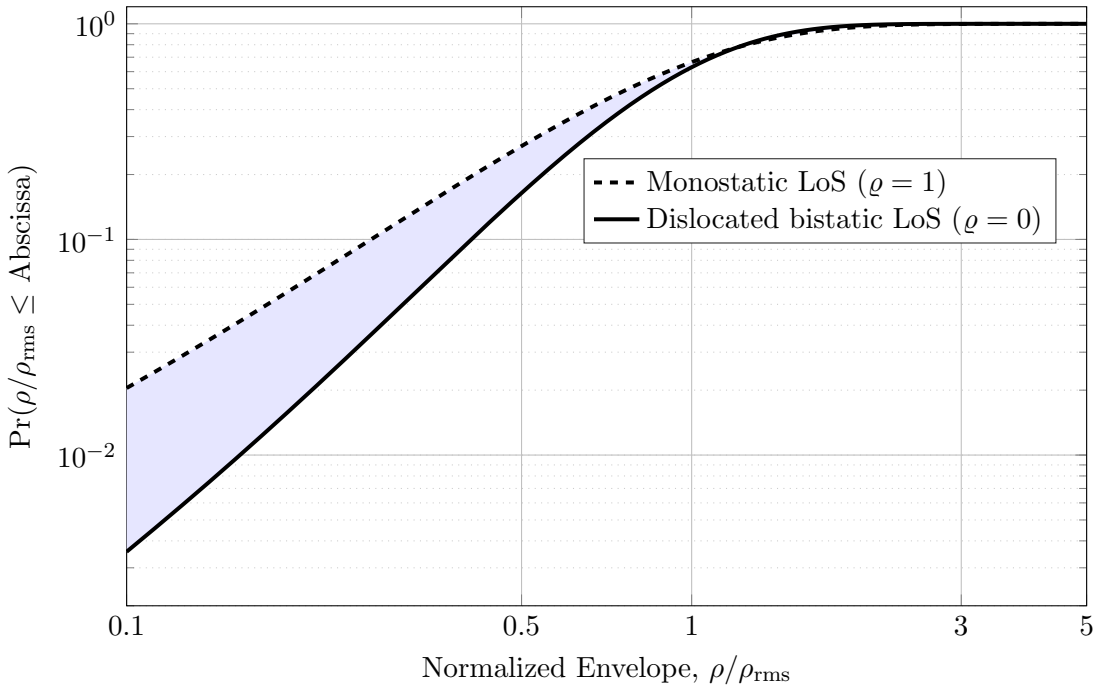

Figure 3.6: Bounded CDF for a product-Rician distribution (LoS propagation). The shaded area represents the possible locations for the CDF of correlated channels.

where $\bar{\gamma}$ is the average SNR per bit, γ is the instantaneous SNR per bit, and $P_{\text{AWGN}}(\gamma)$ is the additive white Gaussian noise (AWGN) BER, which depends on the modulation type. Let us assume that we use BPSK, then $P_{\text{AWGN}} = Q(\sqrt{2\gamma})$, where $Q(\cdot)$ is the complementary error function defined as $Q(y) = (2/\pi) \int_y^\infty \exp(-x^2)\, \mathrm{d}x$. Furthermore, $f(\gamma)$ can be derived from the envelope PDF using the following change of variable [68]:

$$f_\gamma(\gamma) = \frac{1}{2\sqrt{\gamma\bar{\gamma}}} f_\rho\left(\sqrt{\frac{\gamma}{\bar{\gamma}}}\right). \tag{3.30}$$

The integral in Equation (3.29) is solved numerically for all of the distributions in Tables 3.1 and 3.2 and the results are shown in Figures 3.7 and 3.8 [62].

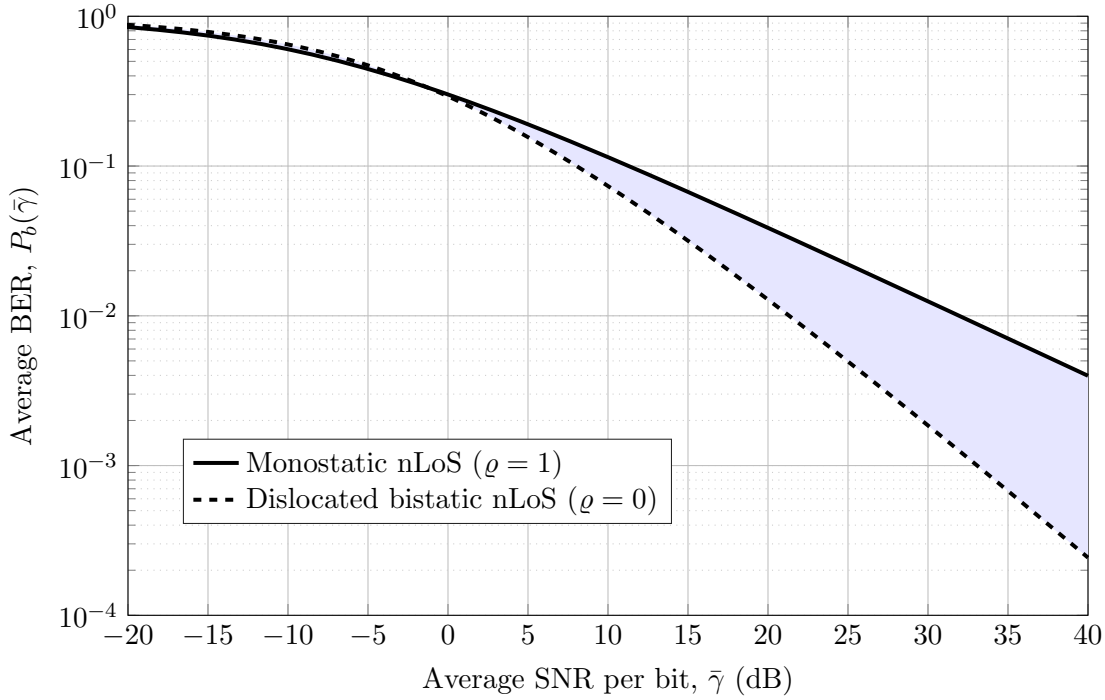

Figure 3.7: BER versus SNR for nLoS propagation. The shaded area represents the BER for correlated forward and backward channels; i.e., $0 < \varrho < 1$ (This figure is adapted from [62], © IEEE 2019).

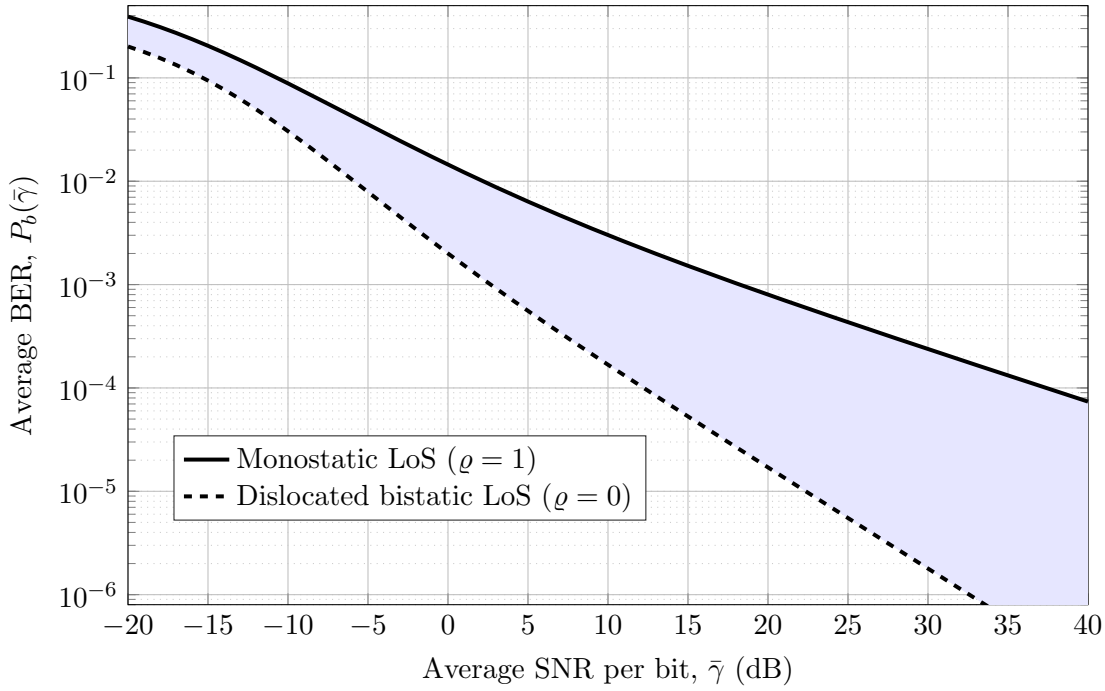

Figure 3.8: BER versus SNR for LoS propagation. The shaded area represents the BER for correlated forward and backward channels; i.e., $0 < \varrho < 1$ (This figure is adapted from [62], © IEEE 2019).

3.4 Chapter Summary

This chapter introduced the concept of fading in wireless channels in general and specifically, fading in backscatter channels. The take away points from this chapter are:

- Wireless signals fade with respect to time, frequency, and/or space. In particular, this chapter focused only on spatial fading in which the transmitter, receiver, and scatterers are static (stationary); and the signal bandwidth is below the channel coherence bandwidth, known as narrowband communications.
- In LoS propagation, the envelope of the received signal follows a Rician distribution while in nLoS, the envelope follows a Rayleigh distribution.
- Backscatter channels are composite channels; that is, they are made of two one-way channels.
- The envelope distribution of the received voltage at the reader depends on the the distribution of the underlying channels as well as the RFID system configuration.
- In the monostatic configuration, the forward channel is exactly the backward channel and we say that these channels are fully correlated.
- In the dislocated bistatic configuration, the forward and backward channels are decorrelated.
- Backscatter link reliability decreases with the increase in the forward and backward channel correlation.
- Correlated backscatter channels under any metric are bounded by the fully correlated and decorrelated channels.

CHAPTER 4
RETRODIRECTIVE ARRAYS

The previous chapters presented some of the challenges associated with backscatter systems. These challenges can be divided into two parts: Electromagnetic- and communication-based challenges. The former refers to the reduction in the communication distance as a result from the low backscattered power by the tag. The later, however, refers to the severe fluctuations in the received signal envelope at the reader receiving antenna.

This chapter focuses on improving the electromagnetic performance of RFID systems operating at microwave and mm-wave frequencies using retrodirective arrays.; that is, this chapter discusses the improvement in the range of backscatter communications when a retrodirective tag is used instead of a single-antenna tag. In particular, this chapter addresses the following points:

- The role of retrodirective arrays in future microwave and mm-wave RFID systems.
- The general theory of retrodirective arrays and in particular, the theory of passive retrodirective arrays.
- The design and analysis of hybrid-based retrodirective arrays.

4.1 Ways to Increase Backscatter Range

In Chapter 2, the free-space backscatter link budget formula—given by Equation (2.10)—has several parameters that can be controlled. The first one is the transmitted power, P_T, which has an upper limit set by the regulatory agencies such as the FCC in the US. The second, third, and forth parameters are the gains of the reader transmitting antenna (G_T), the reader receiving antenna (G_R), and the tag antenna (G_t), respectively. The fifth parameter is the modulation factor, which can be set to values greater than 1 so backscatter systems can communicate over extreme distances such 1200 meters [46]. The last parameter is the carrier frequency (or equivalently, the carrier wavelength). If every parameter is fixed but

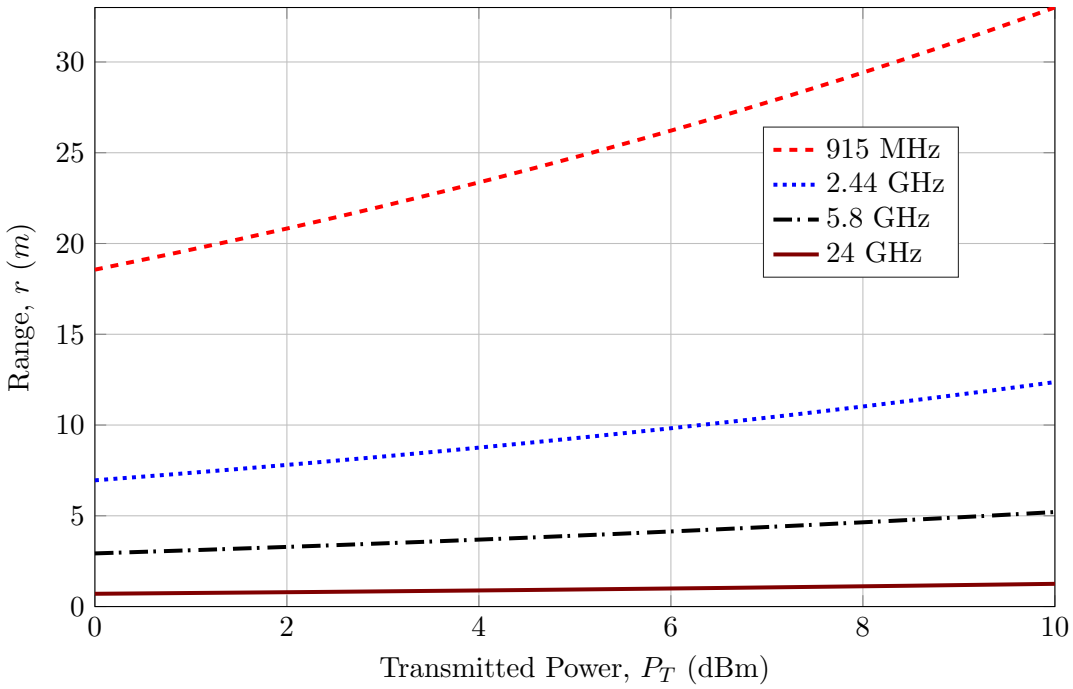

Figure 4.1: Maximum achievable ranges of four tags operating at 0.915, 2.4. 5.8, and 24 GHz. All antennas are identical with a gain of 6 dBi (i.e., $G_T = G_R = G_t = 6$ dBi) and the sensitivity of the reader is -90 dBm (power level below the reader sensitivity is treated as noise) (This figure is adapted from [69]; © IEEE 2019).

the carrier frequency, the maximum achievable range versus the transmitted power for four RFID systems operating at 0.915, 2.4. 5.8, and 24 GHz is depicted in Figure 4.1. Therefore, one approach to increase the communication range is to operate at lower frequencies.

Another approach is to increase the reader antenna gains, G_T and G_R. Such approach requires the use of directive antennas or beamforming networks (i.e., phased arrays). In the research literature, the use of beamforming antennas on the reader appeared in the work of Lee *et al.* [17] in which a modified 4×4 Butler matrix is proposed to achieve a 180° beam coverage with gain. Other use cases are discussed in [70, 71, 72]. In the reader, the use of such advanced techniques is plausible since readers in general are not power-source limited devices. However, tags have no or limited access (via batteries) to power sources; therefore, active beamforming techniques are not feasible.

In this dissertation, we focus on finding ways by which the tag antenna gain can increase without adhering to the fundamental antenna theory tradeoff; that is, when the antenna gain increases, its field-of-view narrows. When the tag is equipped with a retrodirective array,

the impinging electromagnetic waves upon the tag are reflected where they come; that is, the array acts as a *passive* beamformer. In other words, the array reflects the impinging electromagnetic waves back towards the direction of incidence with maximal gain. To illustrate this impact, let us rewrite Equation (2.10) in terms of the communication range; that is,

$$r = \frac{\lambda}{4\pi}\left(\frac{G_T(\theta,\phi)G_R(\theta,\phi)G_t^2(\theta,\phi)P_T\xi M}{P_R}\right)^{1/4}, \tag{4.1}$$

where we expressed each antenna gain as a function of the elevation (θ) and azimuth(ϕ) angles, respectively. Furthermore, we can assume that $\xi = M = 1$. If the tag is equipped with an N-element array, then $G_t = \eta f(\theta,\phi)G_t(\theta,\phi)$, where η accounts for the array efficiency, $f(\theta,\phi)$ is the array angular taper, and $G_t(\theta,\phi)$ the array constituent element gain. However, when the tag is retrodirective, $f(\theta,\phi) = N^2$. The impact of this constant taper is depicted in Figure 4.2, which shows the same four systems in Figure 4.1 but the tags are now equipped with N-element retrodirective arrays. For fair comparison, we fix the physical area of all tags to that of a tag equipped with a square patch antenna operating at 915 MHz. Furthermore, Figure 4.2 shows that, contrary to Figure 4.1, ranges are comparable. In fact, high-frequency ranges can be further increased beyond that of the 915-MHz system if the reader is equipped with phased arrays.

4.2 General Theory of Planar Retrodirective Array

In this section, the theory of retrodirective arrays is derived using two approaches: The first approach uses the array factor of a uniform-linear array. The second approach treats the N-element array as an $N \times N$ system and studies the scattering matrix of that system. Most of the derivations are adapted from [73, 74, 75, 69].

Historically, the first retrodirective array was proposed by Van Atta [73], which was intended to be used as radar chaff since retrodirective arrays increase the RCS of the object to which they are attached; therefore, falsifying the recorded echo [76]. Unlike radar, RFID targets—the tags—benefit from the increase in the RCS since the communication distance increases with the increase in the RCS.

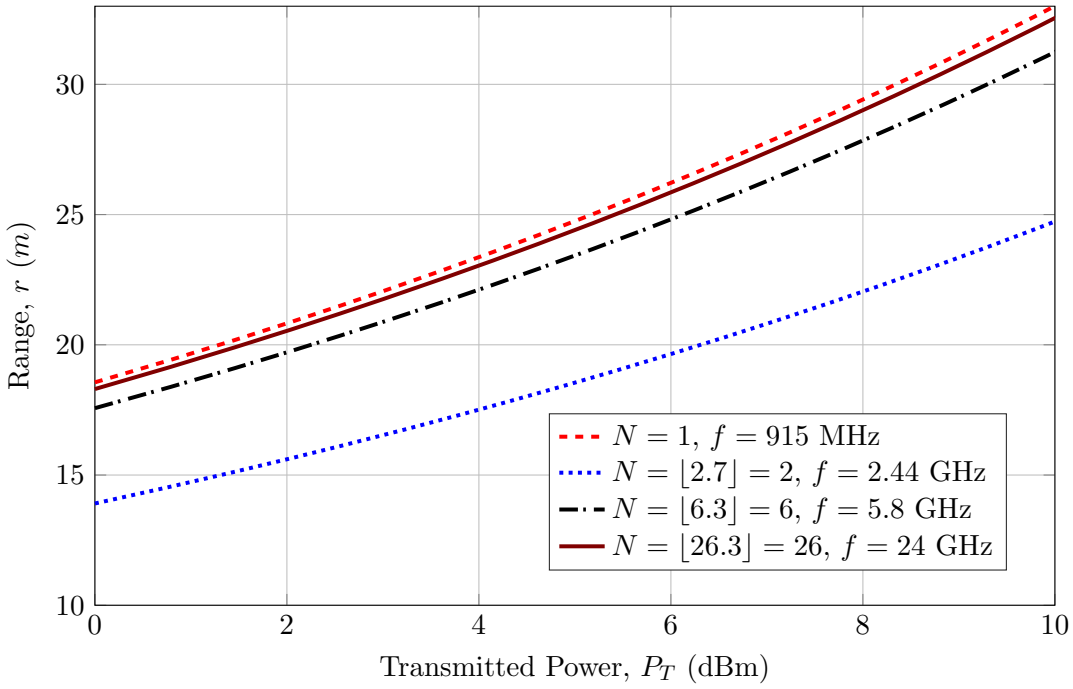

Figure 4.2: Maximum achievable ranges of four tags operating at 0.915, 2.4. 5.8, and 24 GHz all equipped with retrodirective arrays. All of the reader antennas are identical with a gain of 6 dBi (i.e., $G_T = G_R = 6$ dBi) and the sensitivity of the reader is -90 dBm (power level below the reader sensitivity is treated as noise). The floor operation is used to ensure that the physical area of the array does not exceed that of a single antenna at 915 MHz (This figure is adapted from [69]; © IEEE 2019).

An array becomes retrodirective if it conjugates the phase of the impinging electromagnetic wave. This condition is equivalent to reversing the space since the radiation pattern of an antenna (wavenumber domain) and the current distribution (space domain) are Fourier-transform pairs. Therefore, testing whether an array is retrodirective or not is equivalent to testing if the array conjugates the phase of the impinging waves.

4.2.1 Array Factor Approach

Let us assume that we have a linear, uniformly-spaced N-element array such as those in Figure 4.3. The array receives a two-dimensional oblique plane wave. The array factor of such an array is

$$AF(\theta) = \sum_{n=1}^{N} \tilde{a}_n e^{-j[(n-1)k_\circ d \sin\theta]} \leq \sum_{n=1}^{N} |\tilde{a}_n| \,, \tag{4.2}$$

where $\tilde{a}_n$ is the complex excitation of the n^{th} element. Furthermore, the antenna gain, G, is proportional to the magnitude-squared of the array factor; that is, $G \propto \|AF(\theta)\|^2$. The goal of any array is to maximize the gain at a specific angle, θ_s, which is equivalent to finding values under which the inequality in Equation (4.2) is an equality. In standard arrays, this goal can be accomplished with proper phasing of the input waveform. However, in the reflection-type array, the complex excitation coefficients are functions of the impinging waves. Therefore, the only way to maximize Equation (4.2) at θ_s is if

$$\tilde{a}_n = a_\circ e^{+j(n-1)k_\circ d \sin\theta_s}, \tag{4.3}$$

where $a_\circ$ is an arbitrary constant. In the case of retrodirective arrays, this maximization is necessary for all angles that fall under the supporting angular range of the array constituent element, $[\theta_L, \theta_U]$. Therefore, the complex excitation coefficients *must* have the following form:

$$\tilde{a}_n = a_\circ e^{+j(n-1)k_\circ d \sin\theta_i}, \quad \forall n = 1, \ldots, N \quad \text{and} \quad \forall \theta_i \in [\theta_L, \theta_U]. \tag{4.4}$$

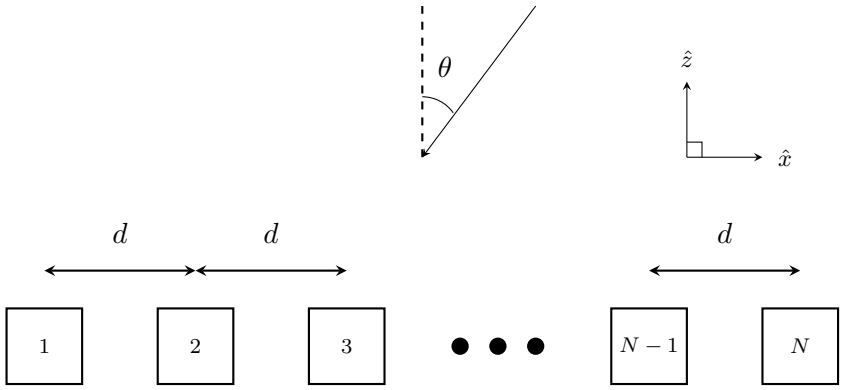

Figure 4.3: A linear, uniformly-spaced N-element array (This figure is adapted from [69]; © IEEE 2019).

The phase of the impinging wave is identical to the argument of the exponent in Equation (4.2) by antenna reciprocity. Thus, the phases of the coefficients, $\tilde{a}_n$, in Equation (4.4) are the *complex-conjugate* to that of the impinging waves, which is the retrodirectivity condition.

4.2.2 Scattering Matrix Approach

Another approach is to model an N-element array as an $N \times N$ system—such as that in Figure 4.4—and study the transmission or the scattering matrix of the system. Since retrodirective arrays are reflection-based arrays, each antenna captures and reflects waves. The reflected wave from antenna i, $a_{i,\text{out}}$, in terms of the captured wave by antenna j, $a_{j,\text{in}}$, is given by

$$\begin{aligned}
\tilde{a}_{1,\text{out}} &= \tau_{11}\tilde{a}_{1,\text{in}} + \tau_{12}\tilde{a}_{2,\text{in}} + \ldots + \tau_{1N}\tilde{a}_{N,\text{in}} \\
\tilde{a}_{2,\text{out}} &= \tau_{21}\tilde{a}_{1,\text{in}} + \tau_{22}\tilde{a}_{2,\text{in}} + \ldots + \tau_{2N}\tilde{a}_{N,\text{in}} \\
\vdots \quad &\quad \vdots \qquad\qquad\qquad \vdots \\
\tilde{a}_{N,\text{out}} &= \tau_{N1}\tilde{a}_{1,\text{in}} + \tau_{N2}\tilde{a}_{2,\text{in}} + \ldots + \tau_{NN}\tilde{a}_{N,\text{in}},
\end{aligned} \tag{4.5}$$

where τ_{ij} represents the portion of the captured wave by antenna j that is reflected by antenna i. The transmission coefficients τ_{ij} in Equation (4.5) can be written in a matrix

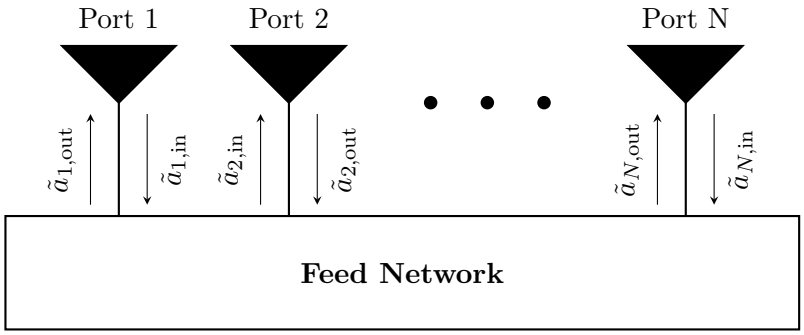

Figure 4.4: An N-port system representation of an N-element reflection-based array (This figure is adapted from [69]; © IEEE 2019).

form as

$$S = \mathcal{T} = \begin{bmatrix} \tau_{11} & \tau_{12} & \dots & \tau_{1N} \\ \vdots & \vdots & \vdots & \vdots \\ \tau_{N1} & \tau_{N2} & \dots & \tau_{NN} \end{bmatrix}, \tag{4.6}$$

where $\mathcal{T}$ is the transmission matrix, which is identical to the array scattering matrix, S. In the subsequent analyses, only the term scattering matrix is used.

When the array is retrodirective, the scattering matrix in Equation (4.6) is anti-diagonal. Ideally, the anti-diagonal entries should have a unity transmission coefficient, τ. However, the deviation from the ideal behavior is caused by one two reasons: First, other entries are non-zeros. Second, the anti-diagonal entries have transmission coefficients that are less than one. The former is caused by weak isolation of the antenna ports while the latter is caused by the internal losses of the feed network and/or the impedance mismatch between the antennas and the feed network. In addition, when a reflection-type amplifier is used, the transmission coefficient can be greater than one.

4.3 Non-Planar Retrodirective Arrays

Another well-known method for implementing retrodirective arrays is proposed by Pon [75] in which the phase conjugation property is achieved using a hetordyne technique that mixes the input signal (from the antenna) with a signal from a local oscillator that operates at

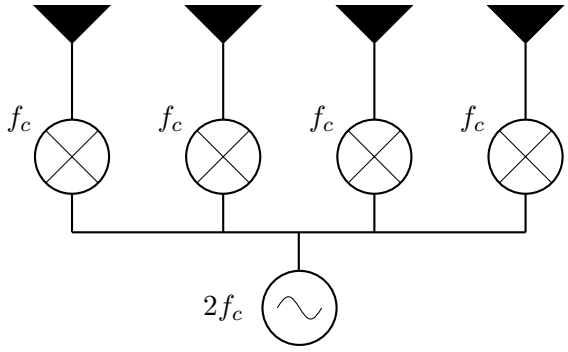

Figure 4.5: A four-element Pon array

twice the carrier frequency. For example, referring to Figure 4.5, if the impinging wave has a carrier frequency f_c, then the output of the mixer has the following form:

$$\begin{aligned} V_{\text{out}} &= \underbrace{\cos(2\pi(2f_c))}_{V_{LO}} \underbrace{\cos(2\pi f_c + \phi_i)}_{V_{IN}} \\ &= \frac{1}{2}\left[\underbrace{\cos(2\pi(3f_c) + \phi_i)}_{\text{Upper sideband}} + \underbrace{\cos(2\pi f_c - \phi_i)}_{\text{Lower sideband}}\right], \end{aligned} \tag{4.7}$$

where ϕ_i is the input phase. From Equation (4.7), the phase of the lower sideband is the negated version of that of the input signal, which is the main property of retrodirective arrays. Therefore, by filtering out the upper-sideband component and feeding the lower-sideband term back to the antenna, one can get a retrodirective response from the array.

Pon arrays offer an extra degree of freedom with regards to the spatial distribution of the array elements. In other words, unlike the elements of a Van Atta array, that of a Pon array need not be on the same plane [75, 77]. However, the need for a mixer makes it more difficult to overcome some of the fundamental losses associated with the mixing process such as conversion loss and isolation. Nevertheless, several studies proposed multiple techniques that tackle this problem. For instance, Pon in his original paper suggested the use of a tunnel diode [75] that—if its oscillation frequency is properly locked [78]—can replace the mixer. Also, Pobanz and Itoh [77] designed a dual-polarization Pon array with a rat-race-based passive mixer that has conversion loss between 5-7 dB. In addition, Barbetz *et al.*

[79] found that if a balanced harmonic mixer that operates at half of the local oscillator frequency[1] is used, conversion loss is reduced to 16 dB.

Since its invention in 1964, Pon arrays are widely used for several purposes besides increasing the backscattered power. For instance, Tuovinen *et al.* used Pon arrays to mitigate deep nulls in multipath environments [80]. In addition, Karode and Fusco [81] showed that Pon arrays can be used to sense both the magnitude and phase of multipath scatterers.

The fundamental limit associated with Pon arrays is that a mixing operation is needed for retrodirectivity, which makes it less common in RFID systems compared to their planar, Van Atta based counterparts. In addition, the feed line from the common double-frequency mixer must introduce identical phase shifts in all paths.

4.4 Designing a Planar Retrodirective Array

This section focuses on the design methodology of planar retrodirective arrays, which can be divided into two subcategories: Van Atta, and hybrid-based arrays. In fact, both categories utilize the same concept proposed by Van Atta [73]. The major distinction between these designs lies on the feed network in which Van Atta arrays use a simple TEM mode transmission line while the hybrid-based arrays use microwave couplers.

4.4.1 Van Atta Arrays

Van Atta arrays, named after its inventor L.C. Van Atta [73], are the most common retrodirective arrays in practice. Theoretically, the Van Atta array conjugates the phase of the impinging waves by connecting each symmetrical antenna pair (with respect to the array center) with transmission lines of equal phase delay as depicted in Figure 4.6. To ensure equal phase delay, each transmission line of an N-element Van Atta array must adhere to the following relation:

$$L_i = L_j \pm n\lambda_m, \quad n \in \mathbb{Z},\ i \neq j, \tag{4.8}$$

[1]Most of the applications of Pon arrays have two distinct frequencies for the receiving ($f_c \pm \delta f$) and transmitting ($f_c \mp \delta f$) mode; therefore, the local oscillator typically operates at $2f_c$.

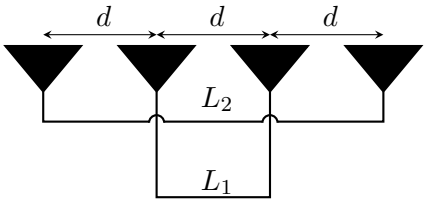

Figure 4.6: A linear four-element Van Atta array

where $i, j = 1, \ldots, N/2$ if N is even; $i, j = 1, \ldots, (N-1)/2$ if N is odd; L_i is the length of the i^{th} transmission line; and λ_m is the transmission line wavelength. However, if N is odd, Equation (4.8) should be modified for the $(N+1)/2$ transmission line. That is,

$$L_{(N+1)/2} = \frac{1}{2}\left(L_j \pm n\lambda_m\right), \quad n \in \mathbb{Z},\ j = 1, \ldots, (N-1)/2. \tag{4.9}$$

Van Atta array can be also designed to achieve retrodirectivity in both the $\hat{x}$- and $\hat{y}$-plane (two-dimensional retrodirective). The two-dimensional retrodirectivity necessitates having an array that is symmetric around the array center. In addition, each element is connected to its spatially reversal counterpart. Graphically, such a connection is shown in Figure 4.7

In most of RFID applications, the tag is planar since planar structures are more compact compared to their non-planar counterparts, which is a key feature for a widespread use of RFID technology. Therefore, the original design, presented by Van Atta, is best implemented on planar structures, which was firstly done by Chung and Chang [82] who proposed a microstrip-based Van Atta array that is retrodirective only on the E-plane. Later, with Tseng, they designed an array that is retrodirective on both E- and H-planes [83].

In the RFID realm, Van Atta arrays have been widely implemented for two main purposes: modulating backscattered signals and increasing the efficiency of the energy harvesting circuits. For the former purpose, Trotter *et al.* and Koo [84, 12] showed the possibility of implementing a quadrature-phase shift keying (QPSK) modulation scheme using a two-element Van Atta array in which the two antennas are switched between four transmission lines that differ in length by $\lambda_m/4$. An alternative option for modulating the backscat-

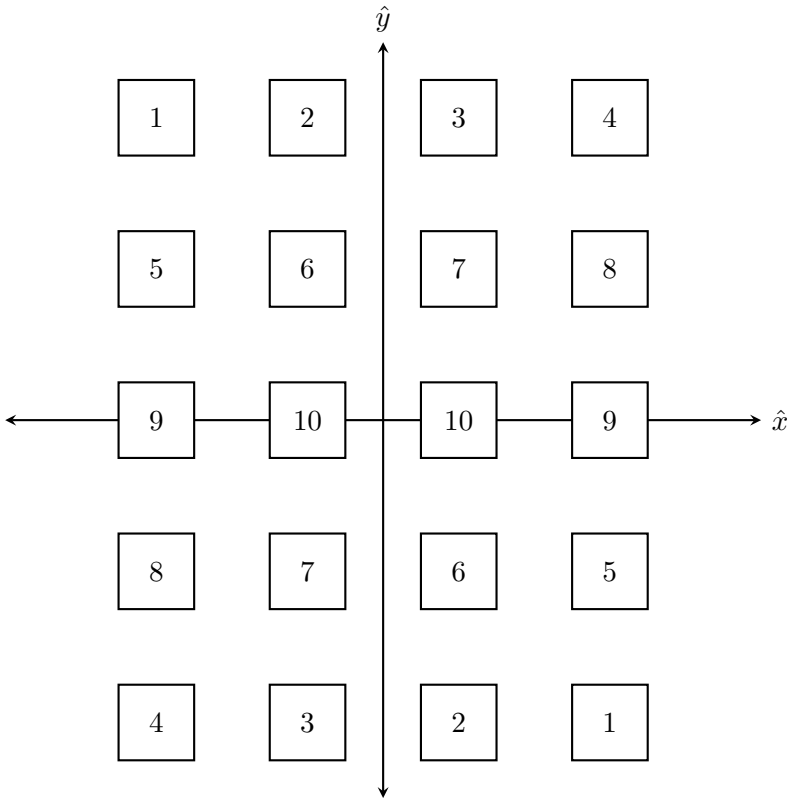

Figure 4.7: A two-dimensional 20-element Van Atta array in which every two squares that share the same number are connected via a transmission line that adheres to Equation (4.8). This figure is adapted from [74] and [75].

tered signal is by using OOK, which appeared in [85] in which four amplifiers each with a gain of 11 dB are placed along the transmission lines that connect each antenna pair of an eight-element Van Atta array. The ON state is when the amplifiers are switched on while the OFF state is when they are switched off. Such switching mechanism results in a power difference of 20 dB between the two states. OOK modulation is also implemented by Chan and Fusco [86] in which the ON state is when the array is retrodirective (no amplification) while the OFF state is obtained by terminating the transmission lines with 50-Ω loads.

The use of Van Atta arrays for the purpose of increasing the harvested energy appeared—for instance—in [87] and [88]. In [87], Ren and Chang designed a 2×2 Van Atta array that harvests RF energy with a conversion efficiency[2] of 73.3%. They also designed a 4×4 Van Atta array that has a conversion efficiency of 55%.

4.4.2 Hybrid Based Retrodirective Arrays

In the research literature, two types of microwave couplers are used as a retrodirective feed network: Branch line (90°) and rat race (also known as ring or 180°). Each type has its own retrodirectivity conditions but they all share the same underlying concept; that is, the array must conjugate the phase of the impinging wave. To derive the retrodirectivity conditions for each coupler, we rely on the scattering matrix approach proposed earlier in this chapter. Therefore, we want the scattering matrix of each coupler to be anti-diagonal.

Branch-Line-Based Retrodirective Arrays

Branch-line couplers are commonly used for power division and beamforming networks. In fact, the well-known Butler matrix [89] is built mainly on branch-line couplers. To be used as a retrodirective feed network, the output ports must be terminated with two loads that have the same reflection coefficients [90].

To derive the retrodirectivity conditions, let us refer to Figure 4.8, which shows a branch-line coupler whose input ports are connected to antennas while the output ports are terminated with two loads whose reflection coefficients are Γ_1 and Γ_2. If the complex input

[2]The conversion efficiency is defined as $\eta = \frac{\text{(Rectified Power (DC Power))}}{\text{(Impinging RF Power)}} \times 100\%$.

vector[3] is given by [69]

$$\tilde{\boldsymbol{a}}_{\text{input}} = \begin{bmatrix} a_\circ \exp(j\phi_1) & a_\circ \exp(j\phi_2) & 0 & 0 \end{bmatrix}^T, \tag{4.10}$$

where $a_\circ$ is a constant magnitude;[4] then, the output complex vector is given by

$$\tilde{\boldsymbol{b}}_{\text{output}} = \underline{\mathbf{S}}\tilde{\boldsymbol{a}}_{\text{input}}, \tag{4.11}$$

where $\underline{\mathbf{S}}$ is the scattering matrix of the branch-line coupler in Figure 4.8, which is given by [90]

$$\underline{\mathbf{S}} = \frac{1}{\sqrt{2}} \begin{bmatrix} 0 & 0 & e^{-j\frac{\pi}{2}} & e^{-j\pi} \\ 0 & 0 & e^{-j\pi} & e^{-j\frac{\pi}{2}} \\ e^{-j\frac{\pi}{2}} & e^{-j\pi} & 0 & 0 \\ e^{-j\pi} & e^{-j\frac{\pi}{2}} & 0 & 0 \end{bmatrix}. \tag{4.12}$$

Now, if ports 3 and 4 are terminated with loads that have complex reflection coefficients, Γ_1 and Γ_2; then, part (or preferably, most) of the waves at these ports reflect back to the coupler. The reflected waves form a secondary source whose complex input vector $\tilde{\boldsymbol{a}}_{\text{ref}}$ is given by

$$\tilde{\boldsymbol{a}}_{\text{ref}} = \begin{bmatrix} \underline{\mathbf{0}} & \underline{\mathbf{0}} \\ \underline{\mathbf{0}} & \underline{\boldsymbol{\Gamma}} \end{bmatrix} \tilde{\boldsymbol{b}}_{\text{output}} = \begin{bmatrix} 0 & 0 & \Gamma_1\tilde{b}_3 & \Gamma_2\tilde{b}_4 \end{bmatrix}^T \tag{4.13}$$

where

$$\underline{\mathbf{0}} = \begin{bmatrix} 0 & 0 \\ 0 & 0 \end{bmatrix} \quad \text{and} \quad \underline{\boldsymbol{\Gamma}} = \begin{bmatrix} \Gamma_1 & 0 \\ 0 & \Gamma_2 \end{bmatrix}. \tag{4.14}$$

This secondary source, $\tilde{\boldsymbol{a}}_{\text{ref}}$, is fed back to the system and multiplied by the scattering

[3] In the derivation, we follow the convention in microwave engineering; that is, the wave that enters the system is denoted by the letter a and the wave that leaves the system is denoted by the letter b.

[4] The fact that the last two entries in Equation (4.10) are zeros is because ports 3 and 4 are not connected to antennas; hence, no input signals exist at these ports.

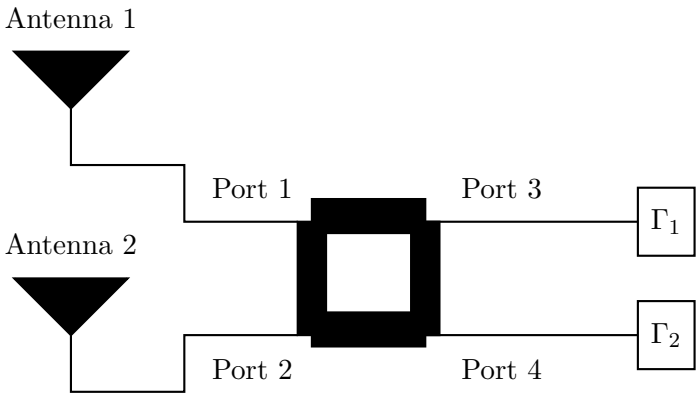

Figure 4.8: A branch-line coupler. The coupler becomes retrodirective if $\Gamma_1 = \Gamma_2$ [90]

matrix in Equation (4.12). Therefore, the output complex vector, $\tilde{\boldsymbol{b}}_{\text{ant}}$, at ports 1 and 2 is

$$\tilde{\boldsymbol{b}}_{\text{ant}} = \underline{\mathbf{S}}\tilde{\boldsymbol{a}}_{\text{ref}} = \underbrace{\underline{\mathbf{S}} \begin{bmatrix} \underline{\mathbf{0}} & \underline{\mathbf{0}} \\ \underline{\mathbf{0}} & \underline{\boldsymbol{\Gamma}} \end{bmatrix} \underline{\mathbf{S}}}_{\text{Total Scattering Matrix}} \tilde{\boldsymbol{a}}_{\text{input}}. \tag{4.15}$$

The sparsity of Equation (4.15) allows the simplification of the 4×4 matrix to a 2×2 matrix of the following form:

$$\begin{bmatrix} b_{\text{ant},1} \\ b_{\text{ant},2} \end{bmatrix} = \frac{1}{2} \begin{bmatrix} (\Gamma_2 - \Gamma_1) & (\Gamma_1 + \Gamma_2)e^{-j\frac{3\pi}{2}} \\ (\Gamma_1 + \Gamma_2)e^{-j\frac{3\pi}{2}} & (\Gamma_1 - \Gamma_2) \end{bmatrix} \begin{bmatrix} a_\circ \exp(j\phi_1) \\ a_\circ \exp(j\phi_2) \end{bmatrix}. \tag{4.16}$$

Thus, the scattering matrix in Equation (4.16) is anti-diagonal if and only if $\Gamma_1 = \Gamma_2$, which is the retrodirectivity condition for branch-line-based retrodirective arrays.

The authors in [90] presented a methodology not only for designing a two-element retrodirective array, but also for designing an N-element array. In fact, they experimentally showed the results for 3, 4, and 6-element array. Historically, the condition in [90] is a generalization of the two-element retrodirective array proposed by Chung *et al.* [91] five years earlier in which the two identical loads are simply reflection-type amplifiers. The authors of [91] also showed that the proposed two-element design has return power that is 4.5 dB more than that of a passive four-element Van Atta array. Building on the theory presented

in [90], Hsu and Ma [92] recently implemented a four-element retrodirective array that uses QPSK modulation scheme to backscatter data at a rate of 4 Mbps. In addition, Islam *et al.* used a branch-line-based retrodirective array to increase the harvested energy [93].

Rat-Race-Based Retrodirective Arrays

Rat-race couplers [94] are also used as power dividers and can be part of a beamforming network. In addition, they can be used as a retrodirective feed network [95, 96, 69]. Referring to Figure 4.9, the retrodirectivity conditions for a rat-race-based feed network is

$$\|\Gamma_1\| = \|\Gamma_2\| \quad \text{and} \quad \angle\Gamma_2 = \angle\Gamma_1 + \pi. \tag{4.17}$$

The derivation of the retrodirectivity conditions is similar to that of the branch-line coupler but with different scattering matrix. That is, the scattering matrix for the coupler in Figure 4.9 is

$$\underline{\mathbf{S}} = \frac{1}{\sqrt{2}} \begin{bmatrix} 0 & 0 & e^{-j\frac{\pi}{2}} & e^{-j\frac{\pi}{2}} \\ 0 & 0 & e^{-j\frac{3\pi}{2}} & e^{-j\frac{\pi}{2}} \\ e^{-j\frac{\pi}{2}} & e^{-j\frac{3\pi}{2}} & 0 & 0 \\ e^{-j\frac{\pi}{2}} & e^{-j\frac{\pi}{2}} & 0 & 0 \end{bmatrix}. \tag{4.18}$$

Following the same process as in the case of the branch-line coupler, the new—simplified—2× 2 matrix is

$$\begin{bmatrix} b_{\text{ant},1} \\ b_{\text{ant},2} \end{bmatrix} = \frac{1}{2} \begin{bmatrix} (\Gamma_1 + \Gamma_2)e^{-j\pi} & (\Gamma_1 - \Gamma_2) \\ (\Gamma_1 - \Gamma_2) & (\Gamma_1 + \Gamma_2)e^{-j\pi} \end{bmatrix} \begin{bmatrix} a_\circ \exp(j\phi_1) \\ a_\circ \exp(j\phi_2) \end{bmatrix}. \tag{4.19}$$

Therefore, the matrix in Equation (4.19) is anti-diagonal; hence, the coupler is retrodirective if the conditions in Equation (4.17) are satisfied. Since one of this dissertation contributions is designing a retrodirective rat-race-based feed network, we are going to delve into the electromagnetic characteristics of such a feed network.

The choice of the terminations in Equation (4.19) is arbitrary; however, switching between possible terminations retains retrodirectivity and allows encoding information in the

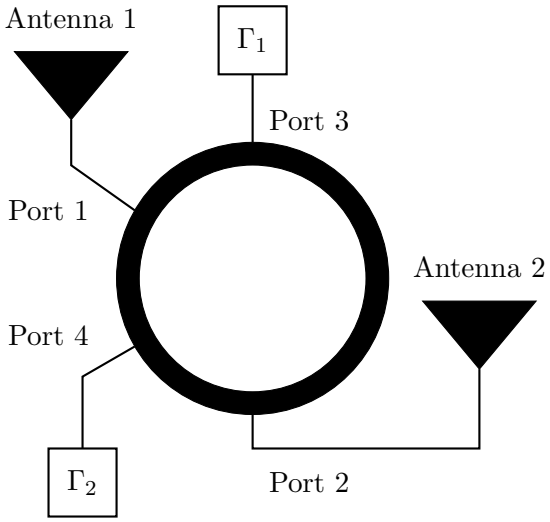

Figure 4.9: A rat-race coupler. The coupler becomes retrodirective if $\Gamma_1 = -\Gamma_2$ [95].

phase of the reflected waves. For example, let us first assume that $\Gamma_1 = 1$, an open-circuit termination, and $\Gamma_2 = -1$, a short-circuit termination. Under this assumption, $b_{\text{ant},1} = a_\circ \exp(j\phi_2)$ and $b_{\text{ant},2} = a_\circ \exp(j\phi_1)$. If we flip the terminations by connecting port 1 to a short circuit and port 2 to an open circuit, then $b_{\text{ant},1} = a_\circ \exp(j\phi_2 + \pi)$ and $b_{\text{ant},2} = a_\circ \exp(j\phi_1 + \pi)$. Because of the 180°-phase change when the terminations are flipped, one can implement a BPSK modulation scheme. The validation of this property was carried out by building a rat-race coupler (pictured in Figure 4.10) operating at 5.8 GHz and measuring its insertion loss, S_{21}, and return losses, S_{11} and S_{22}, for the two cases. The magnitude and phase results, shown in Figures 4.11–4.14, concurred with the expected theory.

We can also quantify the sensitivity of the rat-race coupler to the retrodirectivity conditions in Equation (4.17) by introducing a parameter that we call the *retrodirectivity-loss factor (RLF)* [96], which measures the power ratio of the diagonal terms in Equation (4.19) over that of the off-diagonal terms. Mathematically, we can write the RLF as

$$RLF = \left\| \frac{\Gamma_1 + \Gamma_2}{\Gamma_1 - \Gamma_2} \right\|^2, \quad 0 \leq RLF < \infty \tag{4.20}$$

A true retrodirective coupler must have an anti-diagonal scattering matrix; therefore,

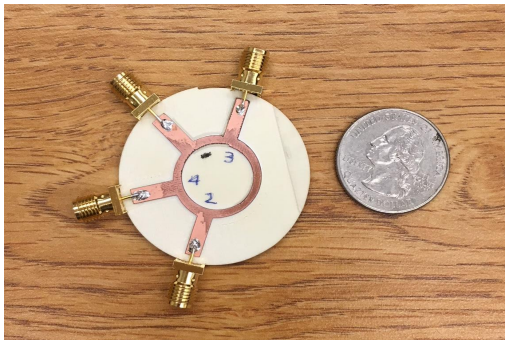

Figure 4.10: A photograph of the designed rat-race coupler (This figure is adapted from [69]; © IEEE 2019).

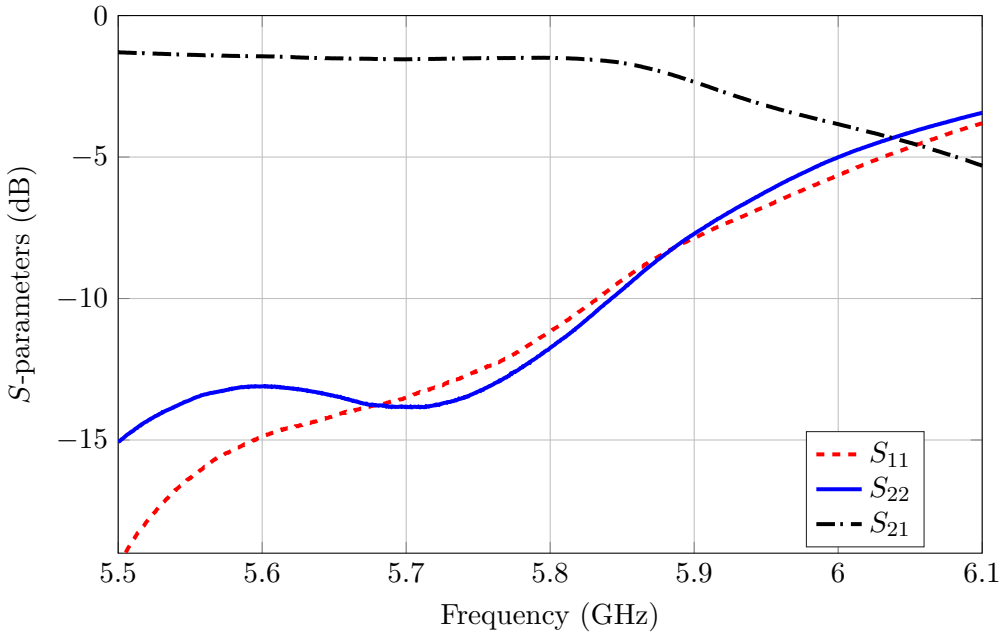

Figure 4.11: The magnitude of the S-parameters for the rat-race in Figure 4.10 when $\Gamma_1 = 1$ and $\Gamma_2 = -1$ (This figure is adapted from [69]; © IEEE 2019).

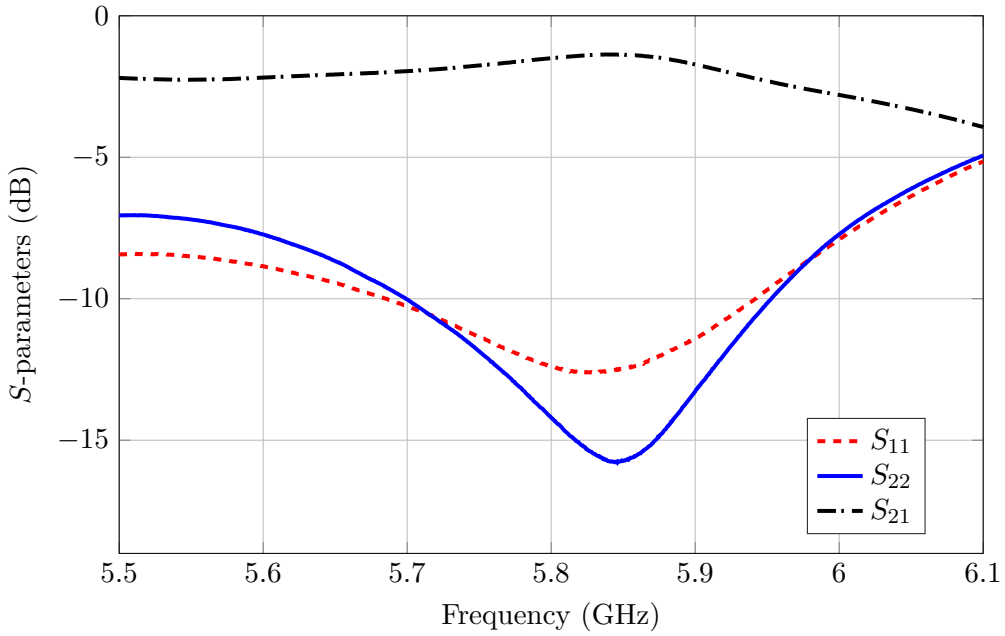

Figure 4.12: The magnitude of the S-parameters for the rat-race in Figure 4.10 when $\Gamma_1 = -1$ and $\Gamma_2 = 1$ (This figure is adapted from [69]; © IEEE 2019).

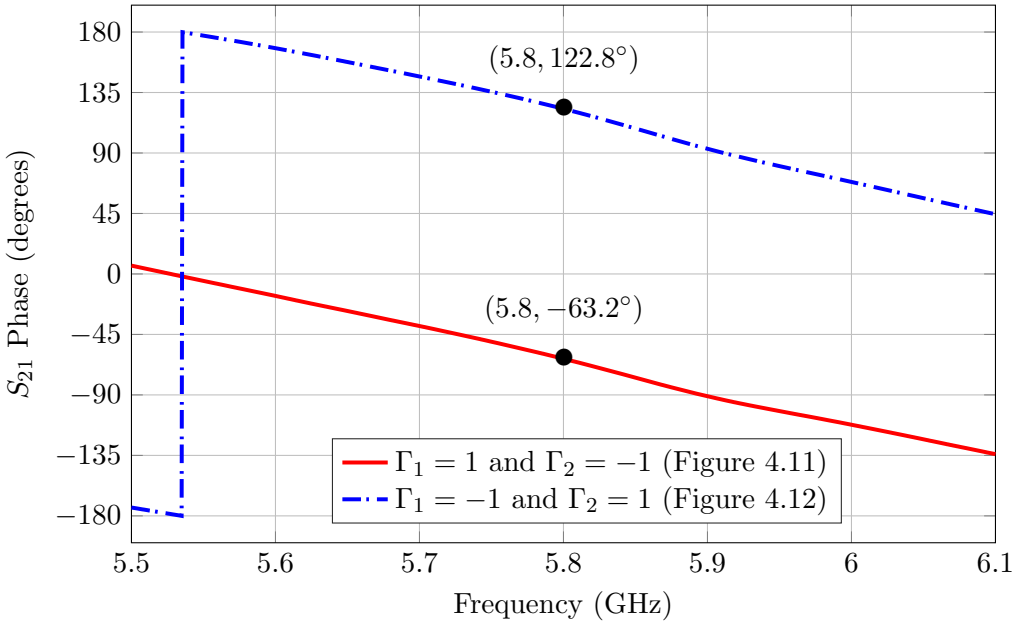

Figure 4.13: The phases of S_{21} for two cases in Figures 4.11 and 4.12. The phase difference between the two states is 174° (This figure is adapted from [69]; © IEEE 2019).

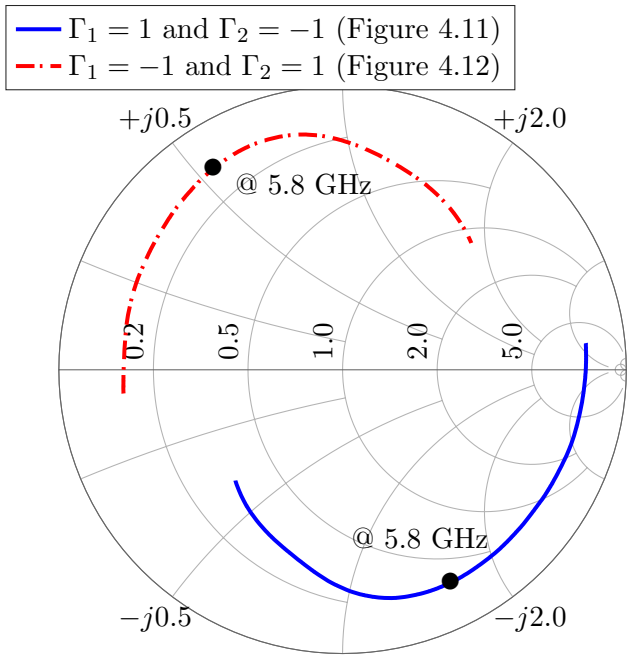

Figure 4.14: Smith chart representation of two possible terminations of ports 3 and 4 (This figure is adapted from [69]; © IEEE 2019).

when $RLF = 0$, the coupler is retrodirective. Since Equation (4.17) constraints both the magnitude and phase of the terminating loads, we can also study each constraint separately and compare the tolerance of the design to the deviation from either constraint. To study the sensitivity to the deviation, we set $\Gamma_1 = \Gamma_\circ \exp(j\phi_\circ)$ and $\Gamma_2 = \alpha\Gamma_\circ \exp(j(\phi_\circ + \pi + \delta))$—where $\Gamma_\circ$ and $\phi_\circ$ are arbitrary magnitude and phase, respectively; and α and $\delta\phi$ are arbitrary magnitude and phase deviation, respectively—then, we can rewrite Equation (4.20) as

$$RLF = \left\| \frac{1 + \alpha e^{j\pi(1+\delta\phi)}}{1 - \alpha e^{j\pi(1+\delta\phi)}} \right\|^2 . \tag{4.21}$$

The heat-map in Figure 4.15 shows that the rat-race coupler is more sensitive to the phase deviation than it is to the amplitude deviation.

Finally, we carried out an open-range experiment on the rooftop the Van Leer building to study the differential radar cross section (RCS) using two modulation schemes, OOK and BPSK. The experimental set-up is shown in Figure 4.16 and the specifications are listed in Table 4.1. The main goal of these experiments is to compare both the beamwidth

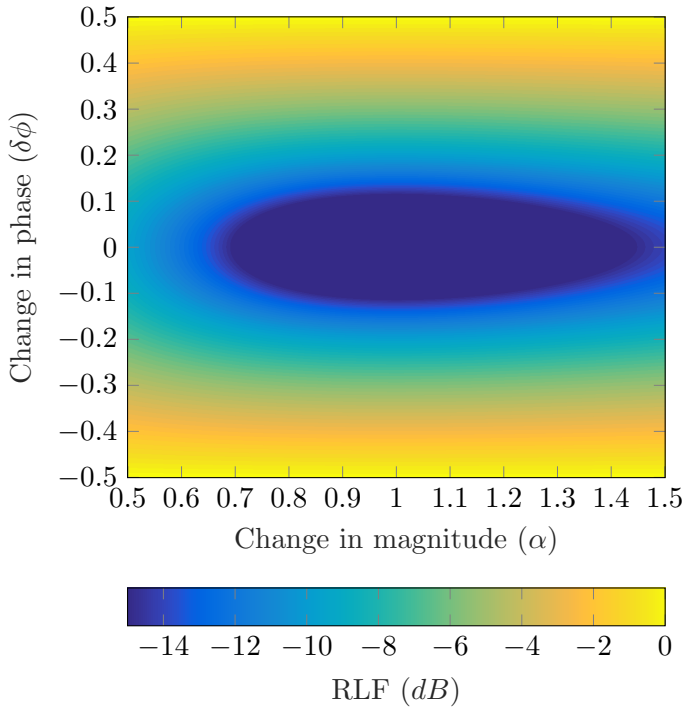

Figure 4.15: A heat-map representation of Equation (4.21) as a function of amplitude and phase deviation, α and δ, in dB scale. Small values (in dB) of RLF occur when Equation (4.20) approaches zero (This figure is adapted from [96], © IEEE 2018).

and magnitude of the differential RCS of a rat-race-based (retrodirective) tag to that of a standard single-antenna tag. In all of these experiments, the response that is recorded is the observed complex insertion loss, S_{21}, in the vector network analyzer (VNA). In addition, the measurement campaign comprises four experiments:

1. Measuring the response with no tags. The data from this measurements are used for background subtraction.

2. Measuring the RCS of a well-known target, which is used to calibrate the measurements. In this experiment, the calibration targets are a sphere and a metallic plate.

3. Measuring the RCS of the retrodirective tag using the permutations listed in Table 4.2.

4. Measuring the RCS of the single-antenna tag using also the permutations listed in Table 4.2.

The measured S_{21} is then *coherently* subtracted from the the background data, which reduces the noise, and scaled by the channel gain obtained from the measured response of the

Table 4.1: The specifications of the open-range experiment in Figure 4.16

Specification	Value
Transmitted power	25 dBm
Frequency span	$(3.8 - 7.8)$ GHz
Separation distance (d)	1.22 m
Angular span	$-90°$ to $90°$
Target height	1.73 m

known targets.

In all of these experiments, the recorded S_{21} response is time-gated. That is, the recorded S_{21}—which is a frequency-domain quantity—is transformed to the time domain using complex IFFT. The time-domain signal is then gated by zeroing out all the values after the desired echo. Then, the gated, complex, signal is transformed back to the frequency domain using FFT and then used for the analyses [96]. Furthermore, the processed data is averaged over the beamwidth of the antenna to obtain the signal constellations in Figures 4.17 and 4.18. The former is for the case of BPSK while the latter is for the OOK scenario. In both cases, the theoretical ratio between the constellation points should be 2; however, the measured ratios are 1.83 and 1.79 for BPSK and OOK modulation, respectively.

The technique used in this experiment campaign is background subtraction with time gating. However, the use of this technique requires operating at lower frequencies or conducting the experiments in an anechoic chamber. The reason behind these requirements is that the technique is coherent, which requires both magnitude and phase calibration. In propagation theory, a slight movement does have a negligible impact on the magnitude but might have a severe impact on the phase; therefore, affecting the system coherence. For instance, at 5.8 GHz—which is the frequency at which these experiments are conducted—a slight movement of 0.5 cm has a 70° round-trip phase error. Therefore, lowering the frequencies reduces the phase error. Also, conducting the experiments in an anechoic chamber reduces the problem of the target movement since the main cause for such movement is

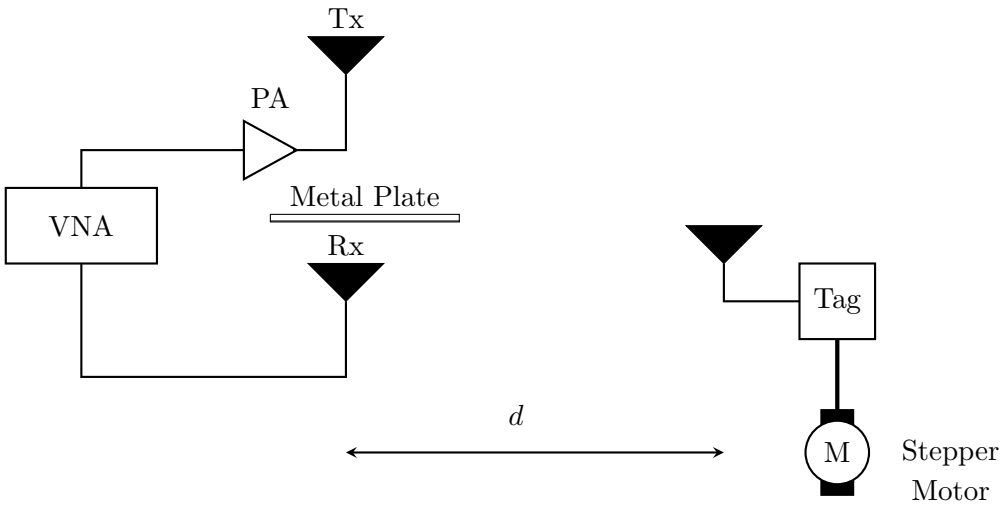

(a)

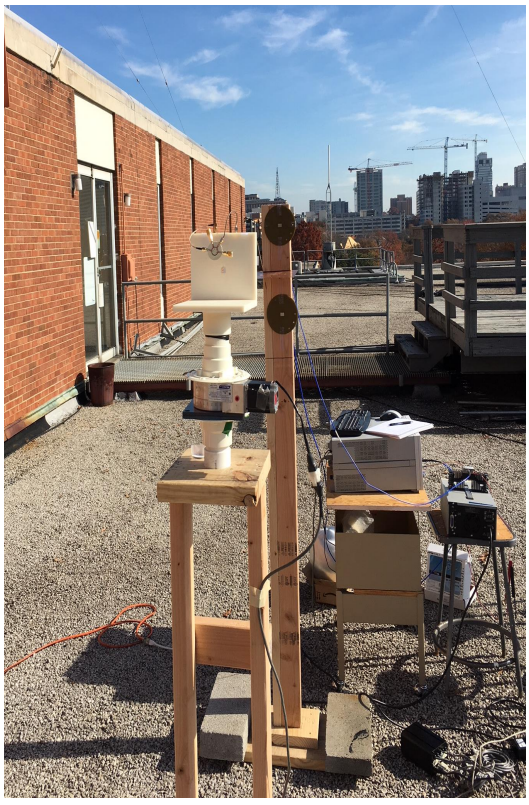

(b)

(c)

Figure 4.16: (a) The experimental set-up used to test the differential RCS of the rat-race-based retrodirective array. (b) and (c) are front and back photograph of the set-up, respectively.

Table 4.2: Termination configurations used for the measurements

Modulation	Tag Type	Port 1	Port 2	Name
BPSK	Retrodirective	Open	Short	Open-Short
		Short	Open	Short-Open
	Single Antenna	Open	-	Open
		Short	-	Short
OOK	Retrodirective	Open	Short	Open-Short
		Short	Short	Short-Short
	Single Antenna	Open	-	Open
		Load	-	Load

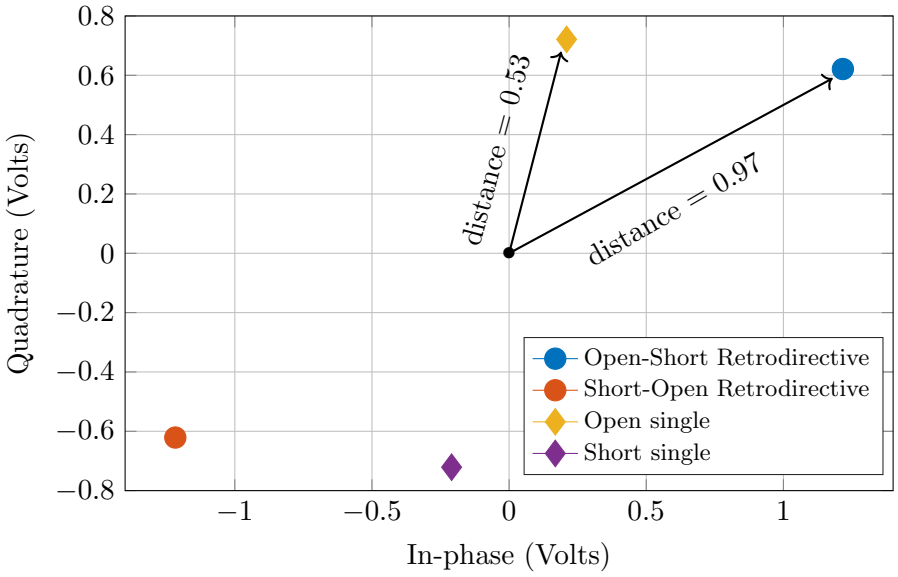

Figure 4.17: BPSK normalized constellation from the measurements using the terminations in Table 4.2 (This figure is adapted from [96], © IEEE 2018).

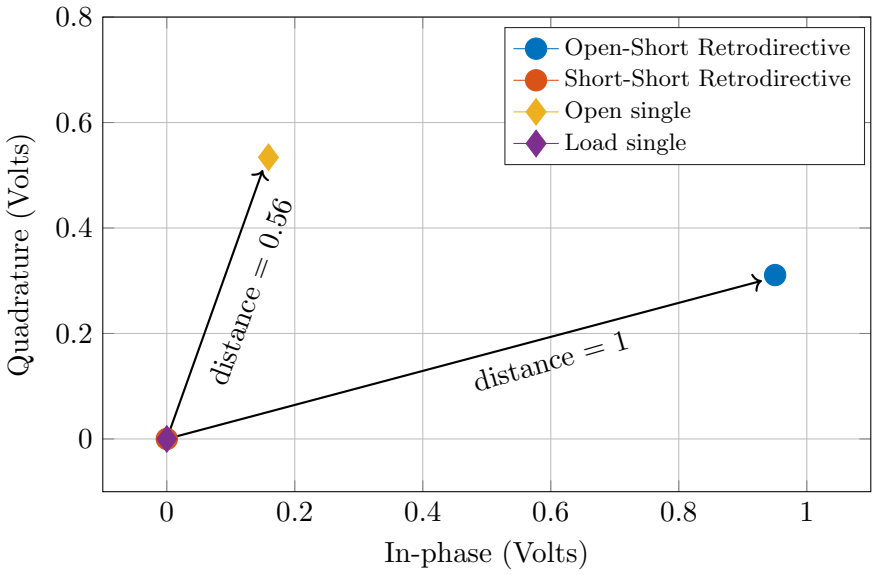

Figure 4.18: OOK normalized constellation from the measurements using the terminations in Table 4.2 (This figure is adapted from [96], © IEEE 2018).

the wind. Nonetheless, averaging the measured data over the target beamwidth yields a-close-to-theory performance.

4.5 Comparisons Between Van Atta and Hybrid-Based Arrays

A standard Van Atta array is relatively easy to design and implement as long as the conditions in Equations (4.8) and (4.9) are satisfied. However, Van Atta arrays have two major limitations. In order to study these limitations, this section compares a printed Van Atta array such as those in [82] and [83] to the rat-race-based retrodirective array in [69]. The following comparisons are also true if a branch-line coupler is used instead of a rat-race coupler but with slight modifications as a result from the difference in the retrodirectivity conditions.

The first point of comparison is the tradeoff between compactness and spectral efficiency. That is, to modulate the retrodirectivity in a standard Van Atta array with PSK, m extra transmission lines must be added, where m is the modulation order. The electric length of those transmission lines must differ at least by a factor of λ_m/m. For example, to implement QPSK, the modulation order is $m = 4$ and four transmission lines should be connected between each antenna pair. In addition, two SP4T switches are needed for

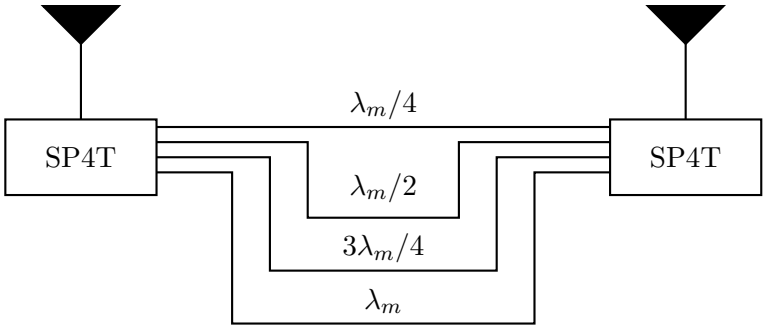

Figure 4.19: A two-element Van Atta array that implements QPSK (This figure is adapted from [12]).

Table 4.3: Load values for a QPSK retrodirective rat-race coupler at 5.8 GHz.

State	Γ_1	Γ_2	Z_1 (Ω)	Z_2 (Ω)
1	$1 + j0$	$-1 + j0$	∞	0
2	$-1 + j0$	$1 + j0$	0	∞
3	$0 + j$	$0 - j$	$j50$ ($L = 1.4\ nH$)	$-j50$ ($C = 0.5\ pF$)
4	$0 - j$	$0 + j$	$-j50$ ($C = 0.5\ pF$)	$j50$ ($L = 1.4\ nH$)

switching between these four transmission lines, which is equivalent to switching between four distinct modulation states. This design is proposed Koo *et al.* [12, 2] and depicted in Figure 4.19. If higher-order modulation is desired, then more transmission lines must be added, which yields an impractical tag size. On the other hand, high-order modulation in the case of rat-race-based retrodirective arrays requires only distinct terminations, which can be any combination of passive circuit elements such as capacitors and inductors—much like the terminations in [50]. For example, Table 4.3 lists the required load terminations for implementing QPSK at 5.8 GHz [95]. To implement higher-order modulation schemes, extra surface-mount passive components are needed, which are significantly smaller in size compared to extra transmission lines.

The second point of comparison is that unlike rat-race-based retrodirective arrays, Van Atta arrays are not compatible with reflection-type amplifiers such as tunnel diodes. The absence of this compatibility stems from the fact that reflection amplifiers should connect

to a single circuit port in which the reflected waves from that port are amplified. To investigate the implication of this compatibility, let us assume that we have two identical tunnel diodes similar to the tunnel diode in [97], which has a modulation factor of $M = 38$ dB (approximately, $M = 6300$ in linear scale). Then, referring to Figure 4.9, if one of these diodes is connected to port 3 and the other is connected to port 4 but that port is extended by a $\lambda_m/4$ to ensure a 180° phase shift between these two ports, then one of two things can be achieved: First, if the modulation is BPSK, then the tag with a tunnel diode has a communication range that is 10 times that of a BPSK tag without a tunnel diode. Second, following the discussions in Chapter 2, we can implement higher-order modulation schemes without compromising the SNR of the system since the distance between modulation states are not restricted by the maximum value of the passive microwave structures reflection coefficient, $\Gamma = 1$. In fact, Γ is much greater than one so that the modulation factor M is greater than one.

4.6 Experimental Comparison Between Hybrid-Based Retrodirective Arrays

In the previous section, the design methodologies of hybrid-based retrodirective arrays are discussed. The previous section also shows that obtaining a clean differential RCS is not feasible with time-gating and background subtraction technique, which is a *frequency-domain* technique. This section, however, focuses on a time-domain technique using a coherent homodyne transceiver (reader). Most of the results and discussions in this sections are drawn from [98]. In all of these experiments, the beamwidth of the normalized differential RCS of retrodirective tags (rat-race- and branch-line-based tag) is compared to that of a standard single-antenna tag. In other words, the latter is used as a baseline. The tag and reader are placed a meter part.

4.6.1 RF Structures

The three antenna systems—single antenna, branch-line-based retrodirective array, and rat-race-based retrodirective array—are simulated using several iterations on both Ansys HFSS and Keysight ADS in which both the circuit and momentum solver are used.

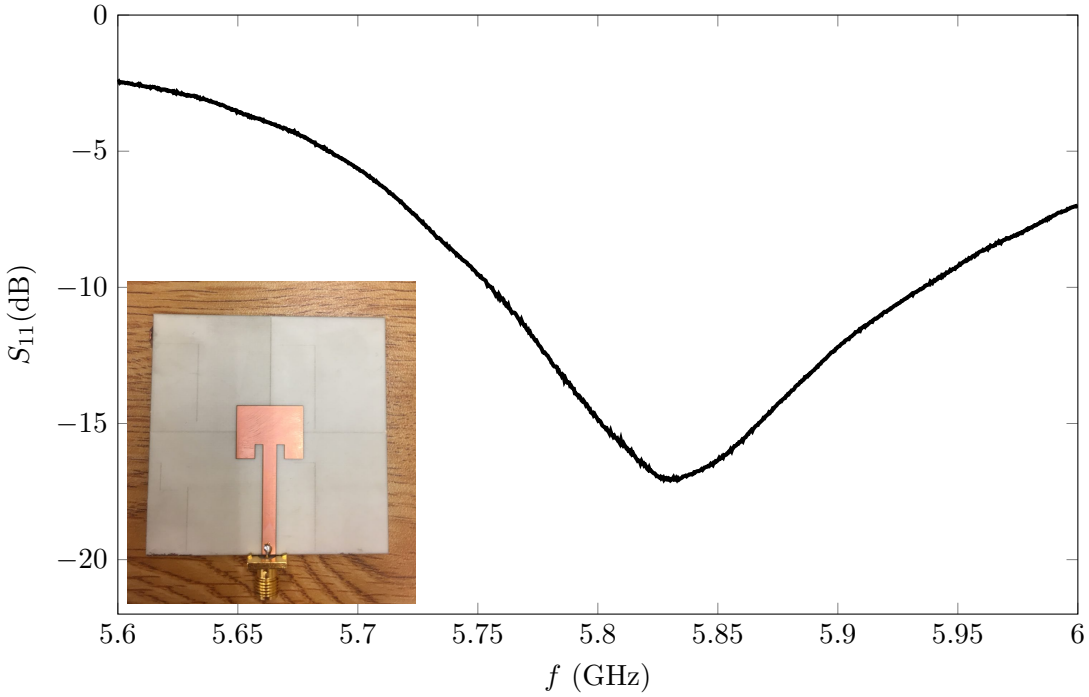

Figure 4.20: S_{11} of the single antenna (This figure is adapted from [98]; © IEEE 2019).

Then, the antenna systems were built on ROGERS 4003C substrate—which has a dielectric constant, ϵ_r, of 3.38 —using the LPKF machine in the Georgia Tech Interdisciplinary Design Commons (IDC). The antenna systems are pictured in Figures 4.20–4.22 as insets to their corresponding scattering parameter plots. The antenna system schematics and layouts are discussed in Appendix D.

4.6.2 RF Modulators

Backscatter modulation takes place using two RF switches that switch between a short-circuit and 50-Ω load. Thus, the modulation scheme is OOK and the theoretical modulation factor M from Equation (2.11) is 0.25 or equivalently −6 dB. However, for the switch components used in this experiment, the actual modulation factor is not similar to the theoretical one. The exact modulation factor depends on the switch part, which is a MINI-CIRCUITS ZFSWA2-63DR+, and the antenna impedance.

To derive the modulation factor from the measured data, we use the measured complex-valued S_{11} and S_{22}. Starting with the RF switches, the measured $S_{11} = \Gamma_L$ is defined

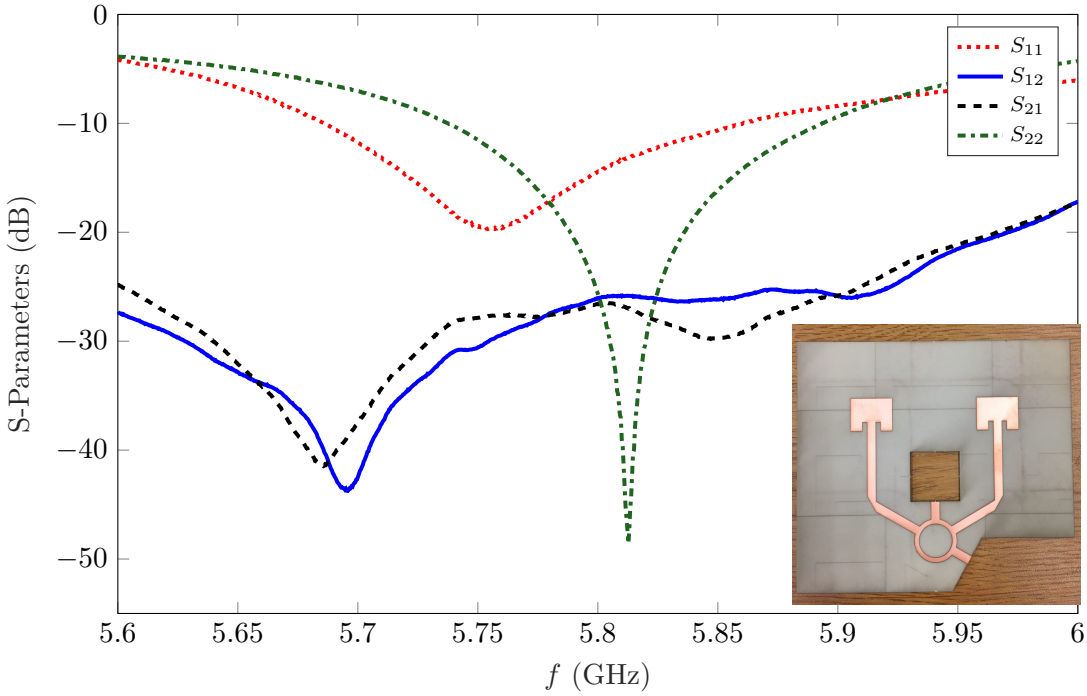

Figure 4.21: S-parameters of the rat-race-based retrodirective array (This figure is adapted from [98]; © IEEE 2019).

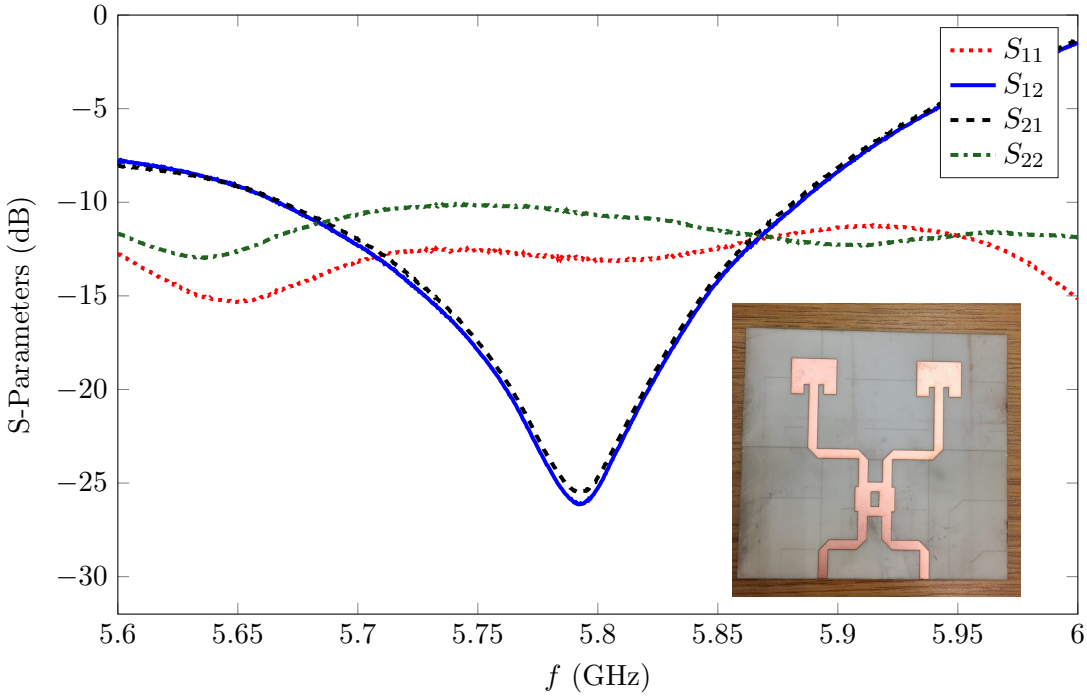

Figure 4.22: S-parameters of the branch-line-based retrodirective array (This figure is adapted from [98]; © IEEE 2019).

as

$$\Gamma_L = \frac{Z_L - Z_{\text{VNA}}}{Z_L + Z_{\text{VNA}}}, \tag{4.22}$$

where Γ_L is the measured reflection coefficient of the load, which can be either short circuit or 50 Ω. In addition, for a calibrated VNA, which is the case for this experiment, $Z_{\text{VNA}} = 50\ \Omega$. Therefore, we can rewrite Equation (4.22) as

$$Z_L = 50\frac{1+\Gamma_L}{1-\Gamma_L} \quad \Omega. \tag{4.23}$$

Similarly, the measured reflection coefficient of the antenna is either S_{11} or S_{22}. In both cases, the antenna reflection coefficient, $\Gamma_a = S_{11,22}$, is defined as

$$\Gamma_a = \frac{Z_a - Z_{\text{VNA}}}{Z_a + Z_{\text{VNA}}}, \tag{4.24}$$

where Z_a is the antenna input impedance defined for each port. Again, the VNA is calibrated, which implies that $Z_{\text{VNA}} = 50\ \Omega$. Therefore, Equation (4.24) can be rewritten as

$$Z_a = 50\frac{1+\Gamma_a}{1-\Gamma_a} \quad \Omega. \tag{4.25}$$

Finally, we can write the conjugate-matched reflection coefficient, to be used in the modulation factor calculation, in terms of the measured reflection coefficients as

$$\Gamma^* = \frac{Z_a^* - Z_L}{Z_a^* + Z_L} = \frac{\left(\frac{1+\Gamma_a}{1-\Gamma_a}\right)^* - \left(\frac{1+\Gamma_L}{1-\Gamma_L}\right)}{\left(\frac{1+\Gamma_a}{1-\Gamma_a}\right)^* + \left(\frac{1+\Gamma_L}{1-\Gamma_L}\right)}. \tag{4.26}$$

This experiment RF switches are characterized in Appendix D.

In this experiment, the RF switches are connected to an Agilent 33250A arbitrary waveform generator (AWG) that sends a square-wave TTL signal. The frequency of that

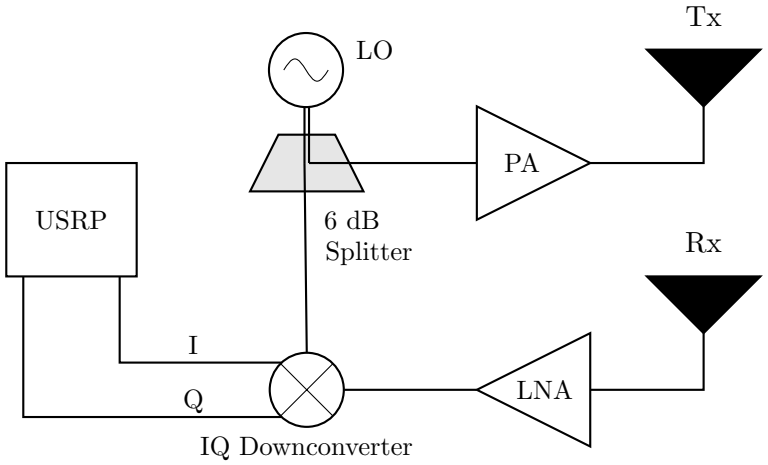

Figure 4.23: The block diagram of the time-domain experiment reader whose specifications are listed in Table 4.4 and Appendix C (This figure is adapted from [98]; © IEEE 2019).

control signal is 1 MHz and it has a 50 % duty cycle. In each experiment, the tag is rotating along its antenna (antennas) H-plane with one-degree increment to ensure fine angular spectra. The tag rotates from -90° to 90° referenced to the point were the tag antenna faces the reader transmitting and receiving antenna. Each experiment lasts about 75 minutes.

4.6.3 Reader

In this experiment, we used a custom-deigned reader based on that proposed by Qi *et al.* [19]. The block diagram of the reader components is depicted in Figure 4.23 and the component specifications are listed in Table 4.4. The received baseband complex signal is sampled in an N200 universal software radio peripheral (USRP) interfaced with GNU Radio. Since we are interested in the SNR per angle relative to other angles rather than the actual data, we applied Goertzel algorithm [99], a DFT-based algorithm, to extract only a small neighborhood of the frequency of interest (1 MHz).

Table 4.4: The specifications of the time-domain differential RCS experiment.

Component	Model	Notes
LO	Agilent E8247C	$P_{\text{out}} = 9$ dBm
Splitter	ZFRSC-183+	-
PA	HMC451LP3	Gain (G)= 12 dB
LNA	HMC902LP3E	Gain (G)= 13 dB
IQ Downconverter	HMC951BLP4E	Gain (G)= 12 dB

4.6.4 Results

The results of this experiment are shown in Figures 4.24 and 4.25. Since the goal of this experiment is to prove that the retrodirective tags have the same beamwidth as the signal-antenna tag, the absolute differential RCS, $\Delta\sigma$, is not of great importance; therefore, all plots are normalized by their maximum $\Delta\sigma$. As shown in Figures 4.24 and 4.25, all of the antenna systems share *approximately* the same beamwidth. The slight deviation is caused by the mutual coupling between antennas as well the deviation from the retrodirectivity conditions.

4.6.5 Port Isolation

Retrodirective arrays have two distinct radiation patterns: Receiving and transmitting (reflection) pattern [100]. In the receiving mode, each antenna behaves as a standalone antenna with minimal interaction with its neighbors; therefore, each antenna preserves its radiation pattern characteristics. However, in the transmitting mode, the antennas combine together to form an array that steers the main lobe towards the direction of incidence. This discrepancy is a clear violation of the antenna reciprocity; which states that the antenna behavior in the receiving mode is identical to that in the transmitting mode and vice versa. In order to violate antenna reciprocity, more than one port is needed and these ports *must* be isolated. Failure to isolate these ports destroys retrodirectivity.

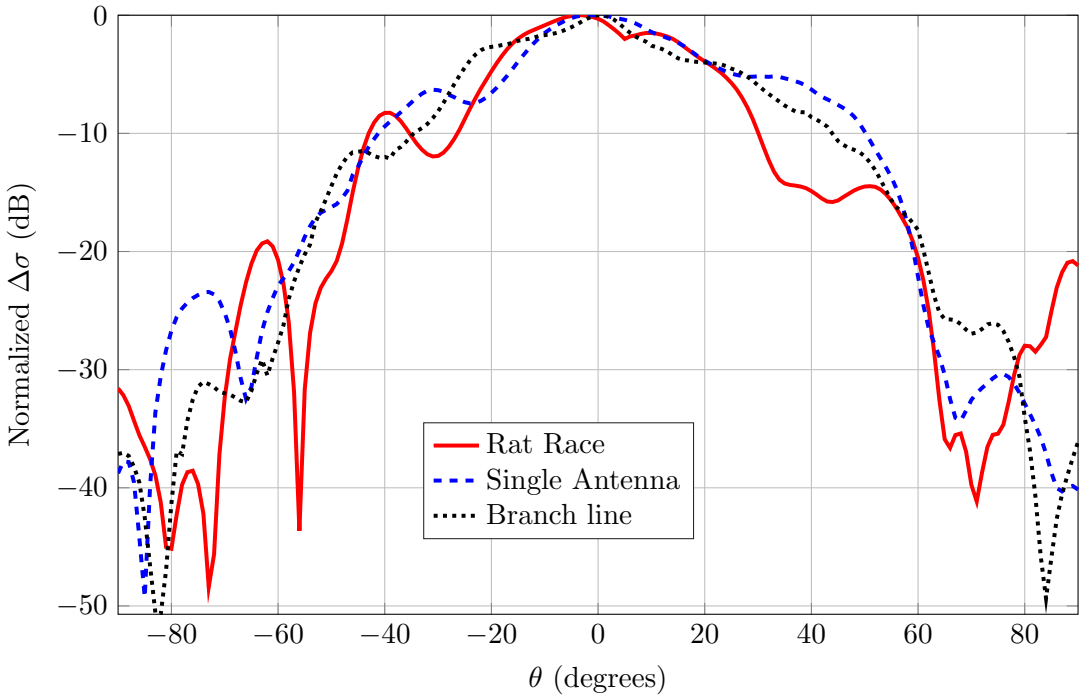

Figure 4.24: The normalized $\Delta\sigma$ for the three antenna systems (This figure is adapted from [98]; © IEEE 2019).

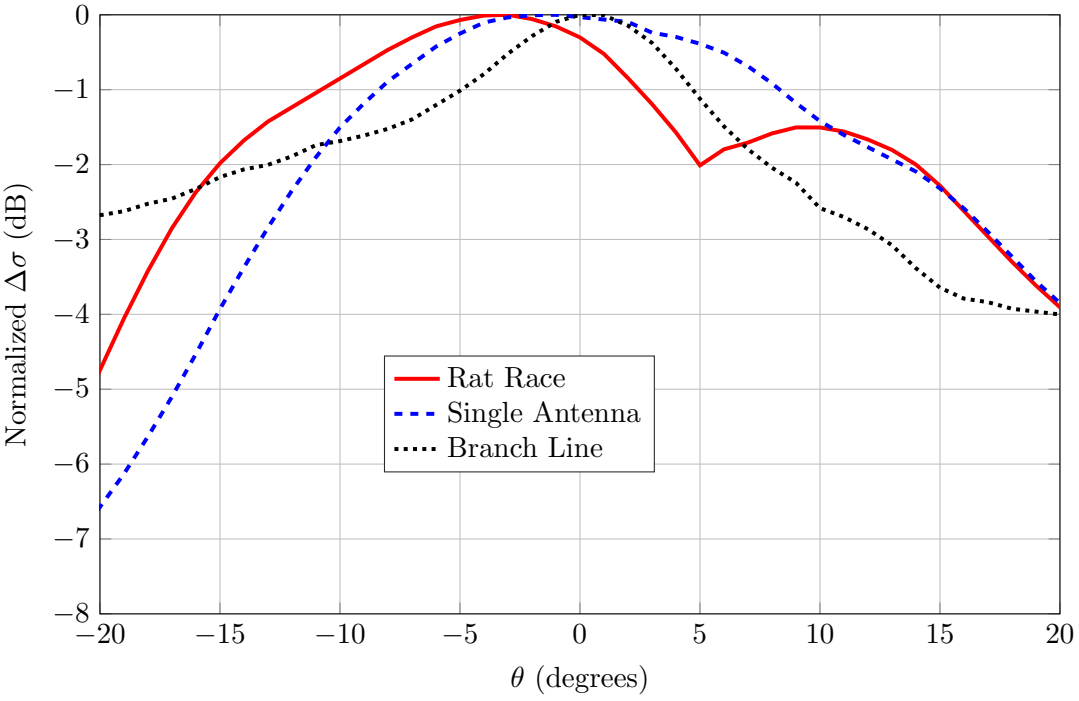

Figure 4.25: The zoomed-in version of Figure 4.24 (This figure is adapted from [98]; © IEEE 2019).

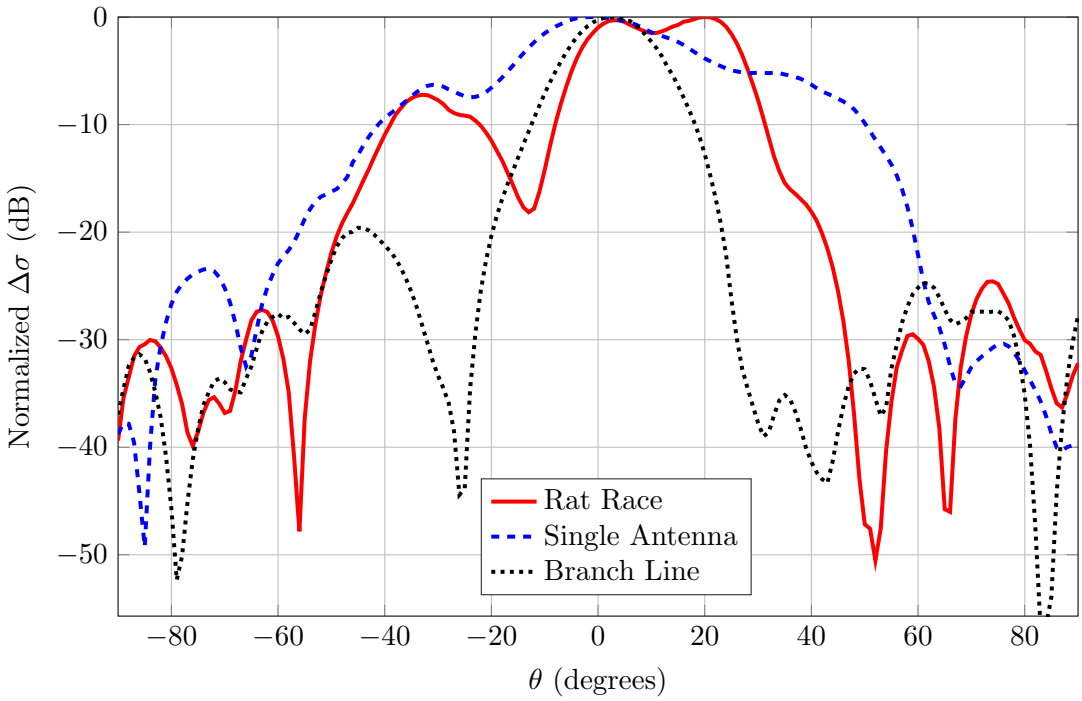

Figure 4.26: The normalized $\Delta\sigma$ for the three antenna systems when the rat-race and branch-line coupler ports are not isolated (This figure is adapted from [98]; © IEEE 2019).

Looking back into Figures 4.21 and 4.22, we conclude that the input ports are isolated since S_{21} and S_{12} in both cases are below -25 dB. To study the impact on retrodirectivity when the ports are not isolated, we conducted an experiment in which the two ports are connected to a power divider than that divider is connected to one RF switch. Therefore, the two ports share the same RF switch. The results of that experiment is depicted in Figure 4.26, which show that what are supposed to be retrodirective arrays are now standard arrays.

4.7 Hybrid-Based Retrodirective Arrays: Which One to Use?

Thus far, two designs of hybrid-based retrodirective arrays are discussed and experimental tested. The use of either one depends on the specific application. The advantages of using the rat-race design over its branch-line counterpart can be summarized as:

1. The standard rat-race coupler —in general—has more bandwidth than the standard branch-line coupler [94]. This can be useful for wideband applications.

2. The absence of sharp edges in the rat-race coupler makes it more appealing when a better signal integrity is desired [101].

3. For a two-element array, a rat-race coupler can be made compact if the termination ports are routed into the center of the ring [96].

On the other hands, the advantages of using the branch-line design over its rat-race counterpart can be summarized as:

1. Branch-line couplers are easier to route in a planar printed circuit board (PCB) since the input ports and the output ports are on different sides.

2. Since the ports are on different sides, expanding the retrodirective array to $N > 2$ is feasible and less complicated [90].

3. Branch-line couplers can easily become a retrodirective feed network since the retrodirectivity condition requires ports 3 and 4 be terminated with two identical loads. On the other hand, the retrodirectivity conditions of a rat-race coupler requires a 180° phase-shift between the loads, which makes the design slightly challenging especially for OOK modulation scheme. In fact, we used additional rat-race couplers to ensure that the phase shift between ports 3 and 4 is as close to 180° as possible

4.8 Chapter Summary

This chapter focuses on the theory of retrodirective arrays along with showing experimental results that support the theory. The take away points from this chapter are:

- Retrodirective arrays are a special type of arrays in which the impinging electromagnetic waves upon the array are reflected back towards the direction of incidence with maximal gain. This property increases the gain of the RFID tag antenna and yet retain the same field-of-view of the array constituent element. In other words, retrodirective arrays are passive, adaptive beamformers.

- Retrodirective arrays can be divided into two categories: Van-Atta-like and Pon-like retrodirective arrays. The former should be planar and requires no mixers while the latter need not be planar but the use of a mixer is necessary.

- One family of Van-Atta-like arrays is the hybrid-based retrodirective arrays in which either a rat-race or branch-line coupler is used in the feed network. This family of retrodirective arrays is more versatile than the standard Van Atta array and can be used to implement wide variety of modulation schemes without expanding the physical dimensions of the system.

- The designer of hybrid-based retrodirective arrays should consider port isolation in addition to return losses. If the designer is faced with the choice of either better matching or better isolation; then, the priority should be given to the latter since losing few dB's will be uniform for all angles; however, not losing those few dB's will be true for only a small subset of angles since the array will not be retrodirective.

CHAPTER 5
RETRODIRECTIVE CHANNELS

The design of a backscatter system requires both electromagnetic- and communication-based analyses. The electromagnetic-based analyses pertain mostly to the link budget formula and the radiation characteristics of the antenna, which was the topic of Chapter 2. On the other hand, the communication-based analyses mostly focus on the statistics of the received signal envelope; that is, fading in backscatter channels, which was the topic of Chapter 3. Both Chapters 2 and 3 show some of the challenges associated with backscatter communications. In particular, Chapter 2 shows that operating at higher frequencies reduces either the communication range or field-of-view of the system. To tackle this problem, Chapter 4 shows that when a retrodirective array is used instead of either a single antenna or a standard antenna array, backscatter tags preserve both the field-of-view of their constituent element and the gain of the array.

On the other hand, this chapter shows that when using a retrodirective array at the backscatter tag, backscatter channels fade akin to their underlying channels. Therefore, retrodirective arrays not only solve the electromagnetic-based challenge (reduction in the communication distance), but they also solve the communication-based challenge (deep spatial nulls). Therefore, this chapter focuses on the backscatter channel statistics when the tag is retrodirective. In particular, this chapter addresses the following points:

- The concept of ideal retrodirective arrays.
- The stochastic model of ideal retrodirective channels.
- The diffuse disparity and its usage in multipath approximations.

5.1 Ideal Retrodirective Arrays

When designing a retrodirective array in a free-space or free-space-like environment, whether the array is ideal or not is not of great importance. However, the non-ideality of the array is

critical when the array operates in a multipath environment since it gives rise to scattering in undesired directions, which in turn contributes to the multipath voltage at the reader receiving antenna. The measurement results in Figures 4.24 and 4.25 do not show this behavior since that type of measurements is monostatic. To study the non-ideality of the array, bistatic measurements should be conducted. The difference between monostatic and bistatic measurements is graphically shown in Figure 5.1. As an example of bistatic measurements, Figure 5.2 shows four plots of the received differential RCS from Pon's original paper [75] in which a four-element retrodirective array is constructed using a dipole antenna as the array constituent element. The plots in Figure 5.2 show the existence of small peaks (and grating lobes) in the directions other than that of the incidence. The contribution of those peaks cannot be ignored since some of them have comparable magnitude to the retrodirective peak. However, those peaks are reduced when the array has a large number of elements.

For an ideal retrodirective array, the array factor in Equation (4.2) should behave akin to the Dirac delta function, $\delta(\cdot)$. This asymptotic behavior is achieved when $N \to \infty$. Therefore, from [102]

$$|AF(\theta)|_{\text{ideal}} = \lim_{N\to\infty} |AF(\theta)| = \frac{\lambda}{\pi d}\delta(\sin\theta - \sin\theta_\circ), \tag{5.1}$$

where the array geometry is identical to that in Figure 4.3. This condition results from the fact the antenna current distribution and its radiation pattern are Fourier-transform pairs. In practice, this condition requires an array with an infinite number of elements; however, the limit can be approached with a finite number of elements if the frequency of operation is increased. For instance, if we have have two systems of patch antennas—such as that in Figure 5.3—in which one of them is operating at 915 MHz (where current RFID systems operate) and the other is operating at 60 GHz (another ISM) band. Then, the array aperture for the first system is 33×0.49 square meters while it is 0.5×0.0075 square meters for the latter. The first design is an impractical RFID tag while the second is more realistic.

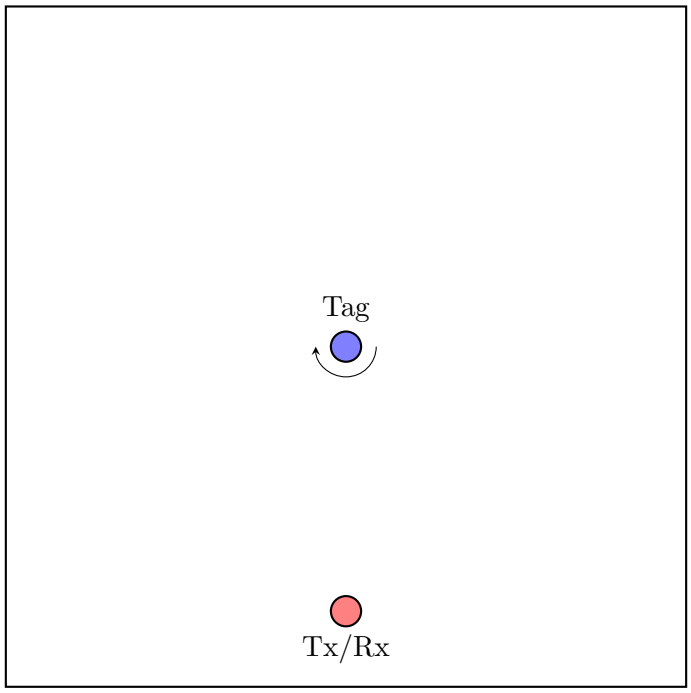

(a)

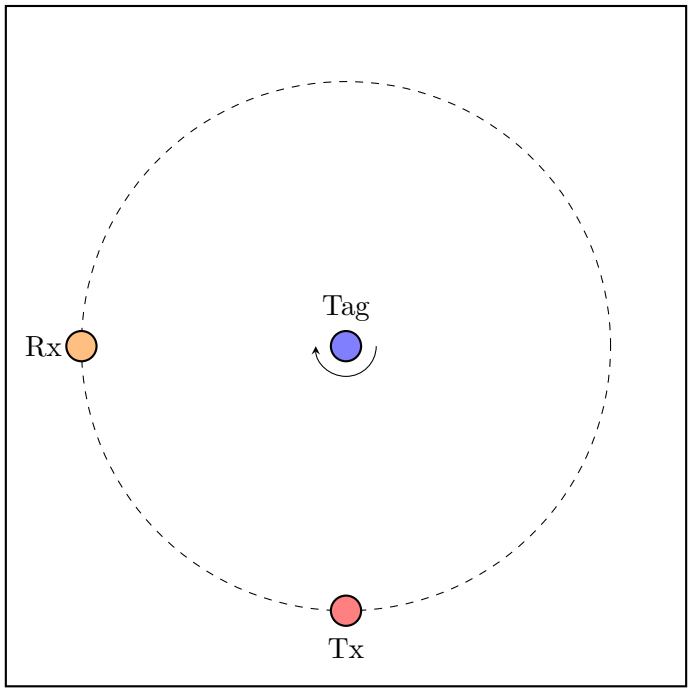

(b)

Figure 5.1: (a) A typical monostatic measurement configuration; the tag is rotating around its axis while the reader transmitting (Tx) and receiving (Rx) antenna are stationary. (b) A typical bistatic measurements; the tag also rotates around its axis but now for every tag rotational angle, the receiving antenna of the reader traces the dashed circle and records the reflected signal for each point. In fact, (a) is a subset of (b) in which Rx is co-located with Tx.

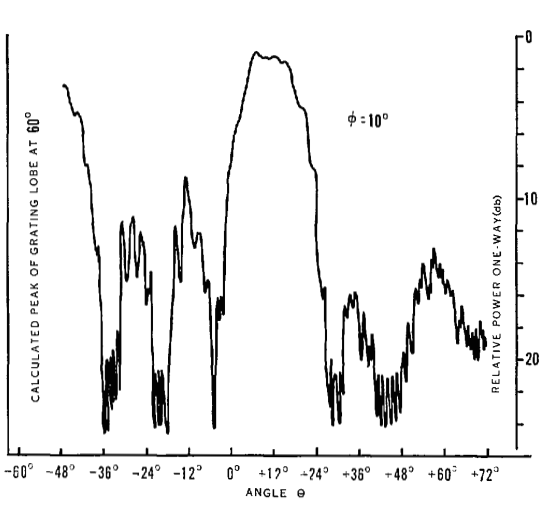

Fig. 9—Measured patterns.

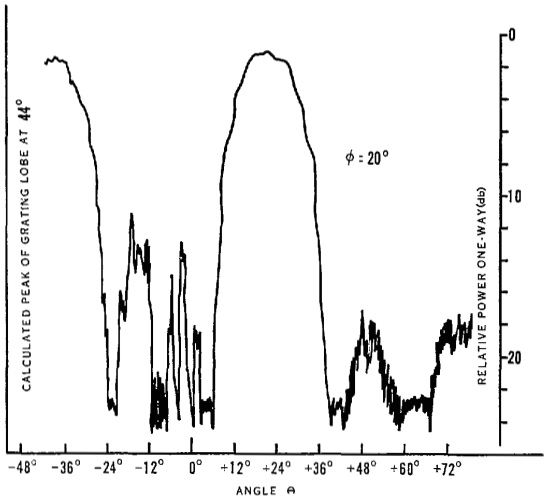

Fig. 10—Measured patterns.

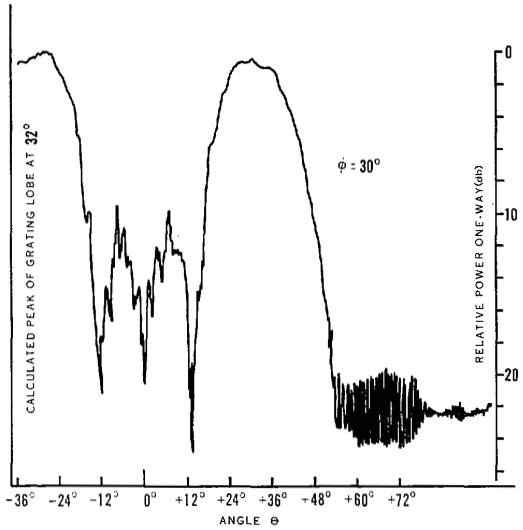

Fig. 11—Measured patterns.

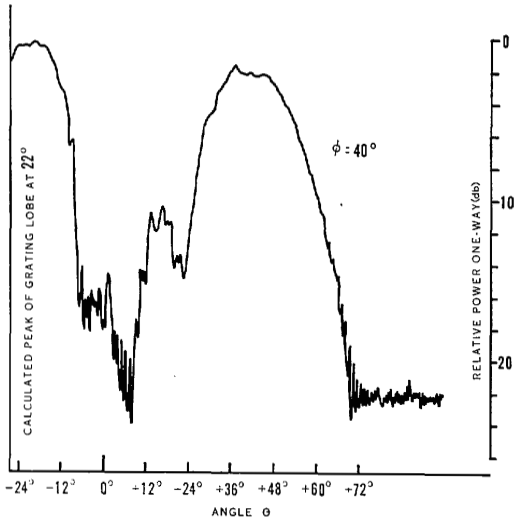

Fig. 12—Measured patterns.

Figure 5.2: The non-ideal response of a finite number of antennas ($N = 4$). The angle of incidence is ϕ (The figure is taken from [75] © IEEE 1964).

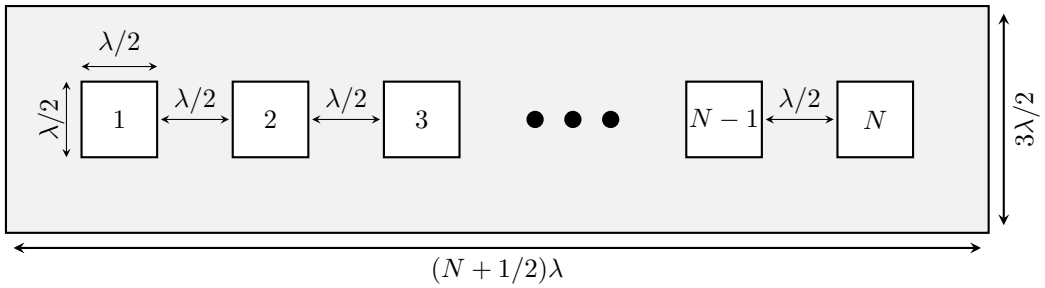

Figure 5.3: A 100-element ($N = 100$) array made of identical square-patch antennas (This figure is adapted from [14]; © IEEE 2019).

5.2 Physical Model of Retrodirective Channels

This section and the subsequent section assume that the antenna array is an ideal retrodirective (IR). Under this assumption, the backscattered complex-electric field from a retrodirective array is [14]

$$\widetilde{\mathbf{E}} = AF(\theta)_{\text{ideal}} N \widetilde{\mathbf{E}}_e, \tag{5.2}$$

where $\widetilde{\mathbf{E}}_e$ is the scattered field by the array constituent element. The open-circuit voltage at the reader receiving antenna can be found from Equation (3.5). In the presence of multipath propagation such as that in Figure 5.4, each multipath component will experience the same reflection but with different value of $\widetilde{\mathbf{E}}_e$. Therefore, the total voltage at the reader antenna has the following form:

$$V_R = \sum_{i=1}^{N} \beta_i^2 \exp\left(j2\Phi_i\right). \tag{5.3}$$

Before proceeding with the analysis, we should make the following points:

- The letter N refers to the number of elements in the array whenever the array factor or the electromagnetic properties of an array are discussed; for instance, Equation (5.2). However, in the context of multipath propagation, N refers to the number of multipath components; for instance, Equation (5.3)

- Equation (5.3) assumes that the RFID system is in the monostatic configuration. In addition, Equation (5.3) can be also used for co-located bistatic systems but with

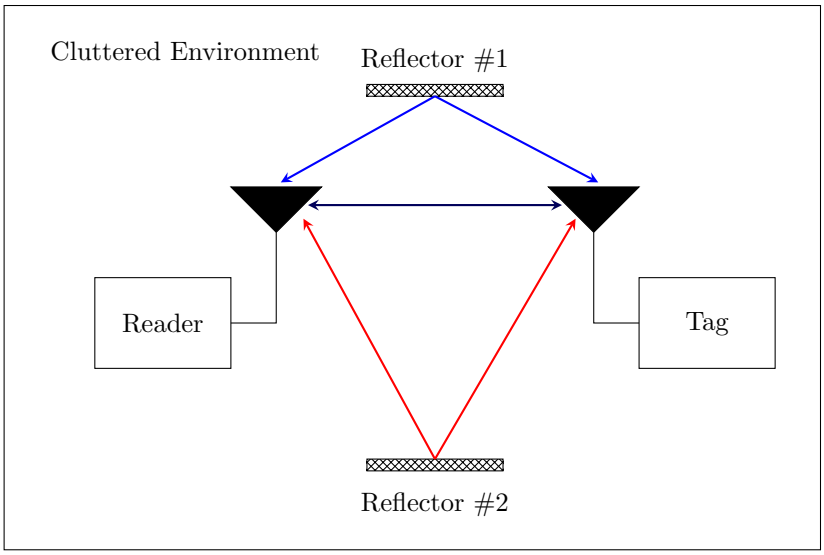

Figure 5.4: A graphical representation of ideal retrodirective arrays in multipath propagation. The tag antenna is a retrodirective array (This figure is adapted from [14]; © IEEE 2019).

a small error, which decreases with the decrease in the distance between the reader transmitting and receiving antenna.

Recall that the tag in a standard backscatter channel discussed in Chapter 3 acts as a pinhole; however, when the tag is *ideally* retrodirective, the pinhole phenomenon does not exist. This observation can deduced directly from Equation (5.3) or from the signal-flow diagram in Figure 5.5. Compared to that in Figure 3.3, the signal flow in Figure 5.5 shows that the only convergence point for multipath components is the reader antenna.

5.3 Statistical Model of Retrodirective Channels

In this section, we derive the *theoretical* stochastic model of backscatter channels when the RFID tags in these channels are equipped with an ideal retrodirective array. The terms ideal retrodirective array and ideal retrodirective channel are used interchangeably in this section. Before delving into the derivation, let us make the following assumptions:

1. The channel is static and frequency flat, which is the same assumption in Chapter 3. Therefore, we consider only spatial fading.

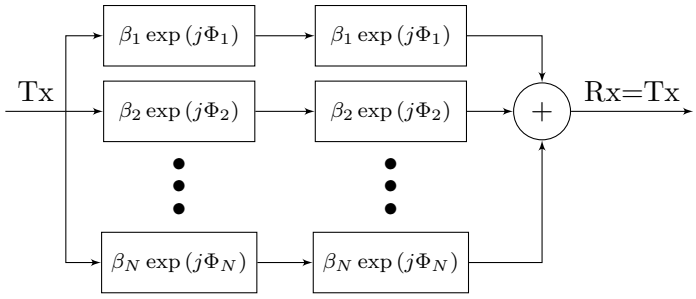

Figure 5.5: A signal-flow diagram for ideal retrodirective channels (This figure is adapted from [14]; © IEEE 2019).

2. The RFID system operates in the monostatic configuration.

3. Multipath waves are modelled locally as independent plane waves.

4. The magnitudes of the multipath components in Equation (5.3) are deterministic quantities.

5. The phases in Equation (5.3), $\Phi_1, \ldots, \Phi_N$, are uniformly distributed between 0 and 2π.

The previous assumptions are consistent with the SLAC model [53].

Let us start with the case of LoS propagation in which we can rewrite Equation (5.3) as

$$V_R = \underbrace{\beta_1^2 \exp(j2\Phi_1)}_{\text{Term A}} + \underbrace{\sum_{i=2}^{N} \beta_i^2 \exp(j2\Phi_i)}_{\text{Term B}}. \tag{5.4}$$

Now, let us statistically compare term A with the specular component in Equation (3.8). Both terms have a constant envelope multiplied by a uniformly-distributed phasor. Furthermore, the phase in term A is uniformly distributed between 0 and 4π, which is not the case for the specular component in Equation (3.8). However, since the phase of a complex signal is a 2π-modulus, both random variables have the same phase distribution. Therefore, we conclude that term A and the specular component in Equation (3.8) have the same distribution but with different moments.

On the other hand, term B can be compared with the diffuse term in Equation (3.8).

The fact that each phasor in term B is multiplied by β_i^2 instead of β_i does change only the moments of each phasor. Furthermore, the phase distribution in term B is similar to that in term A. Therefore, we can leverage the modulus 2π nature of the phase and conclude that the phase is uniformly-distributed between 0 and 2π; hence, term B can be modeled as a complex-circularly symmetric Gaussian random variable.

Since Equation (3.8) is statistically similar to Equation (5.4), we can model the latter as

$$V_R = \underbrace{\beta_1^2 \exp\left(j2\Phi_1\right)}_{\text{Specular}} + \underbrace{\sum_{i=2}^{N} \beta_i^2 \exp\left(j2\Phi_i\right)}_{\text{Diffuse}} = \beta_1^2 \exp\left(j2\Phi_1\right) + \mathcal{CN}\left(0, 2\sigma_{\text{ret}}^2\right) \sim Z_{\text{ret}}. \tag{5.5}$$

The envelope of the random variable Z_{ret} is similar to that in Equation (3.9); that is,

$$f(\rho) = \frac{\rho}{\sigma_{\text{ret}}^2} \exp\left(\frac{-\rho^2}{2\sigma_{\text{ret}}^2} - K_{\text{ret}}\right) I_0\left(\frac{\rho\sqrt{2K_{\text{ret}}}}{\sigma_{\text{ret}}}\right), \tag{5.6}$$

where K_{ret} is

$$K_{\text{ret}} = \frac{\beta_1^4}{2\sigma_{\text{ret}}^2}. \tag{5.7}$$

Note that neither K_{ret} nor σ_{ret} are in general equal to K or σ in Equation (3.9), respectively.

The similarity between the distribution of the ideal retrodirective channel and its underlying one-way channel is not unique to the LoS case. In fact, all of the distributions discussed in [53] should exhibit the same behavior since they all share the same underlying physical model. For instance, when the underlying channel has a Rayleigh fading distribution similar to that in Equation (3.11), the ideal retrodirective channel has also a Rayleigh distribution of the following form:

$$f(\rho) = \frac{\rho}{\sigma_{\text{ret}}^2} \exp\left(\frac{-\rho^2}{2\sigma_{\text{ret}}^2}\right). \tag{5.8}$$

5.4 Statistical Comparison Between the Three Channels

The statistical significance of using a retrodirective array on the RFID tag instead of a single-antenna or even a standard array is better explained with a comparison between three systems that operate under the same multipath environment. We only assume that we have a LoS propagation geometry . Those three systems (depicted in Figure 5.6) are:

1. A standard wireless system such as a cellular user. This system replaces the RFID tag and the statistics are derived (or measured) at the system antenna. The channel where this type of system operates is called the standard one-way (SOW) channel. The envelope distribution of this system is given in Equation (3.9).

2. A standard backscatter system in which the tag is not retrodirective. The channel where this type of system operates is called the standard backscatter (SB) channel and the envelope distribution is given in Table 3.1.

3. A backscatter system in which the tag is ideally retrodirective. The channel where this type of system operates is called the ideal retrodirective (IR) channel and the envelope distribution is given in Equation (5.6).

Since fading parameters of SOW and SB are identical; namely, both channels have distributions expressed in terms of K and σ, they can be compared fairly. However, IR fading parameters are K_{ret} and σ_{ret}, which are not identical to those of SOW and SB. Therefore, in order to make a fair comparison, K_{ret} and σ_{ret} must be expressed in terms of K and σ.

Let us start by defining a unitless quantity, ζ, that captures the relation between the diffuse components in Equations (3.8) and (5.4); ζ is then defined as

$$\zeta = \frac{\sum_{i=2}^{N} \beta_i^4}{\left(\sum_{i=2}^{N} \beta_i^2\right)^2} = \frac{2\sigma_{\text{ret}}^2}{4\sigma^4} = \frac{\sigma_{\text{ret}}^2}{2\sigma^4}, \qquad 0 < \zeta \leq 1. \tag{5.9}$$

This unitless quantity, ζ, is called the *diffuse disparity* since it peaks when the diffuse

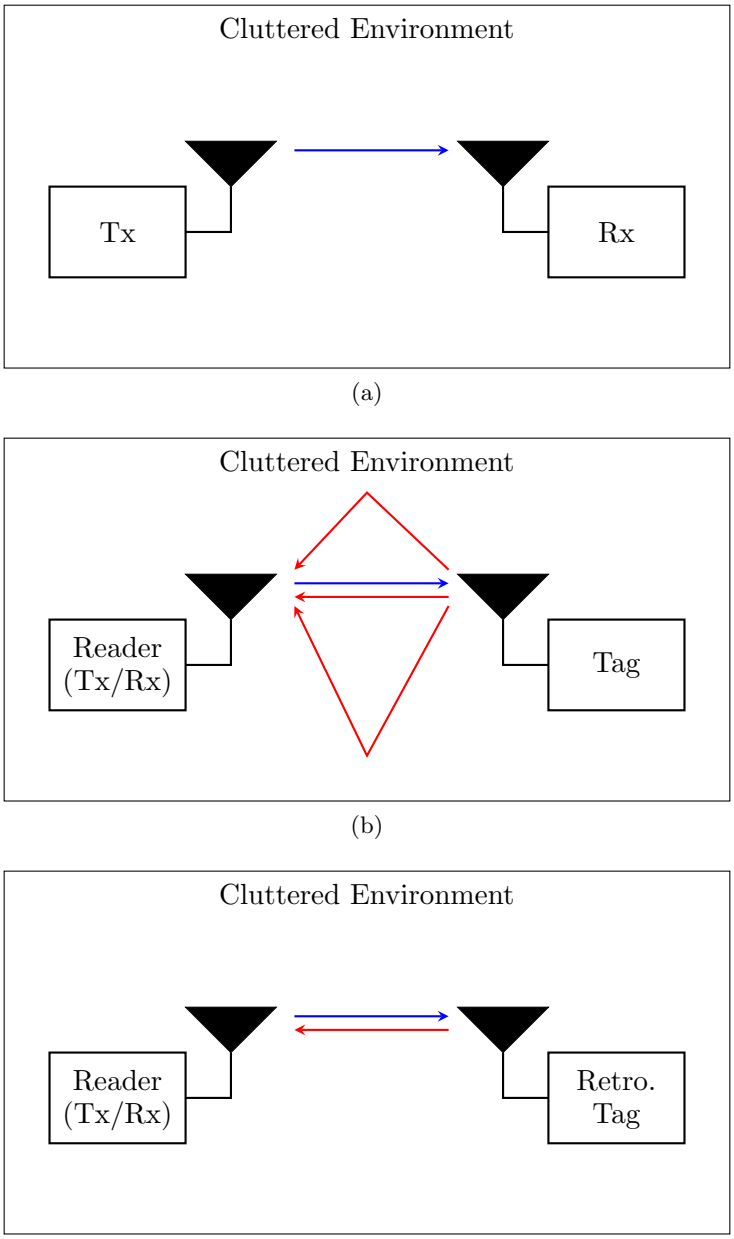

Figure 5.6: A graphical depiction of the three channels: a) SOW, b) SB, and c) IR. To ease visualization, only one multipath component (the direct line of sight) is shown (This figure is adapted from [14]; © IEEE 2019).

components are disparate. With this relation, we can rewrite Equations (5.7) and (5.6) as

$$K_{\text{ret}} = \frac{\beta_1^4}{2\sigma_{\text{ret}}^2} = \frac{4K^2\sigma^4}{4\zeta\sigma^4} = \frac{K^2}{\zeta} \tag{5.10}$$

and

$$f(\rho) = \frac{\rho}{2\zeta\sigma^4} \exp\left(\frac{-\rho^2}{4\zeta\sigma^4} - \frac{K^2}{\zeta}\right) I_0\left(\frac{\rho K}{\sqrt{\zeta}\sigma^2}\right). \tag{5.11}$$

Figures 5.7 and 5.8 plot the PDF's and CDF's of the three systems when the underlying channel has a Rician K-factors of -6 and 6 dB, respectively. In addition, Figures 5.7 and 5.8 show that the impact of the diffuse disparity becomes more pronounced when the K-factor is large. Furthermore, when the K-factor of the underlying channel is greater than 1 (or 0 dB), the K-factor of the IR channel is always greater than that of its underlying channel. This fact can be deduced from Equation (5.10) as well as Figure 5.8. The physical intuition behind this behavior is that when the backscatter channel is equipped with an ideal retrodirective tag, every multipath component is reflected back where it comes; therefore, strong components are reflected towards the strong paths while weak components are reflected towards paths that further weaken them.

5.4.1 Diffuse Disparity

In the case of frequency-selective fading, *some* of multipath components can be measured. These measured components are called resolvable components [68]. However, spatial multipath components in Equations (3.8) and (5.4) can not be measured. With the diffuse disparity, one can gain an intuitive understanding about the diffuse component distribution and use this intuition to find an equivalent diffuse component distribution. Experimentally, we can find the value of the diffuse disparity by conducting two distinct experiments: First, we measure the diffuse power at the tag, from which we can estimate $2\sigma^2$. The second experiment involves measuring the diffuse power at the RFID reader when the tag is ideally retrodirective, from which we can estimate $4\zeta\sigma^4$. Then, we can take the ratio in Equation (5.9) to find the value of ζ. The results from these experiments can be then used

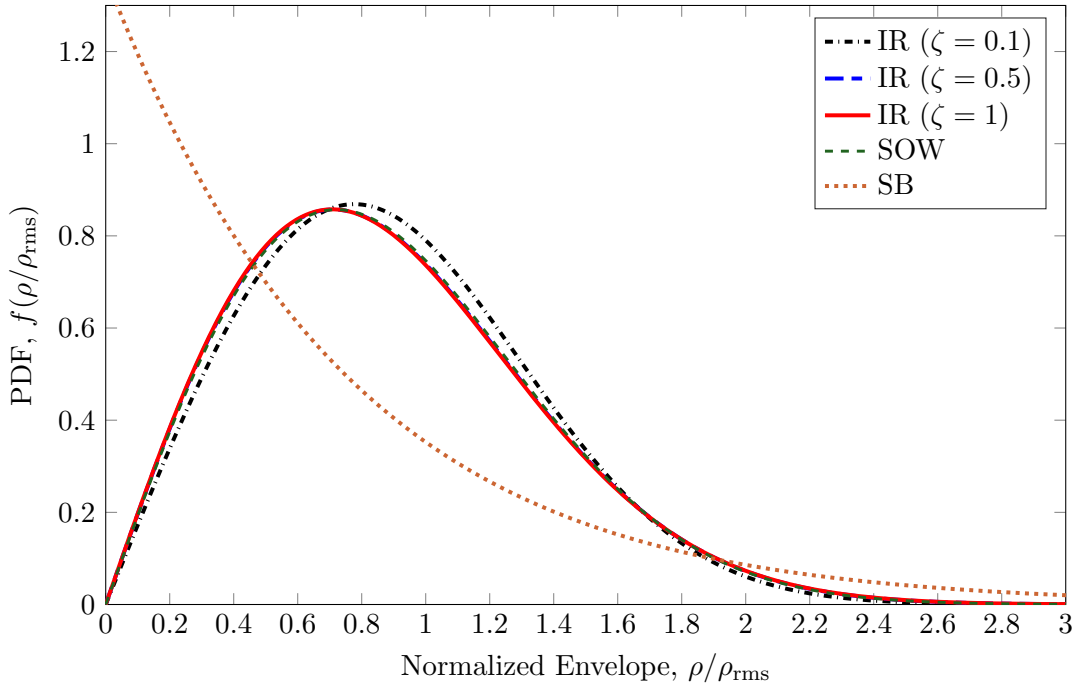

(a)

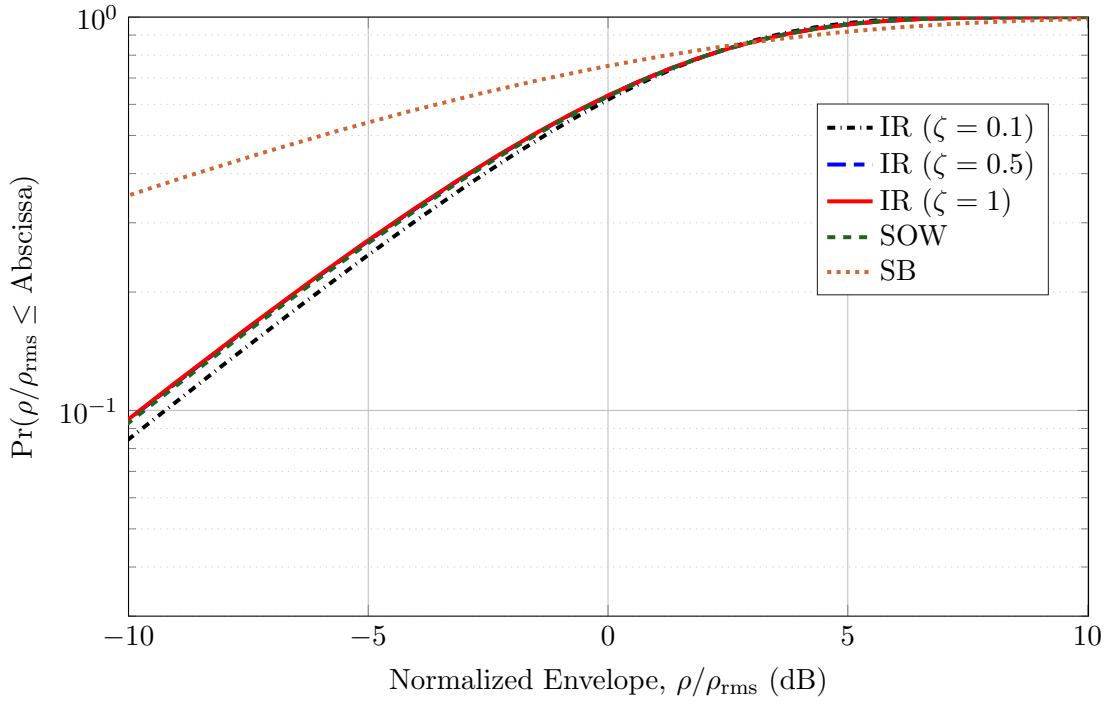

(b)

Figure 5.7: PDF's (a) and CDF's (b) versus the RMS value of the distribution when the underlying channel is Rician with $K = -6$ dB and $\sigma = 1$ (This figure is adapted from [14]; © IEEE 2019).

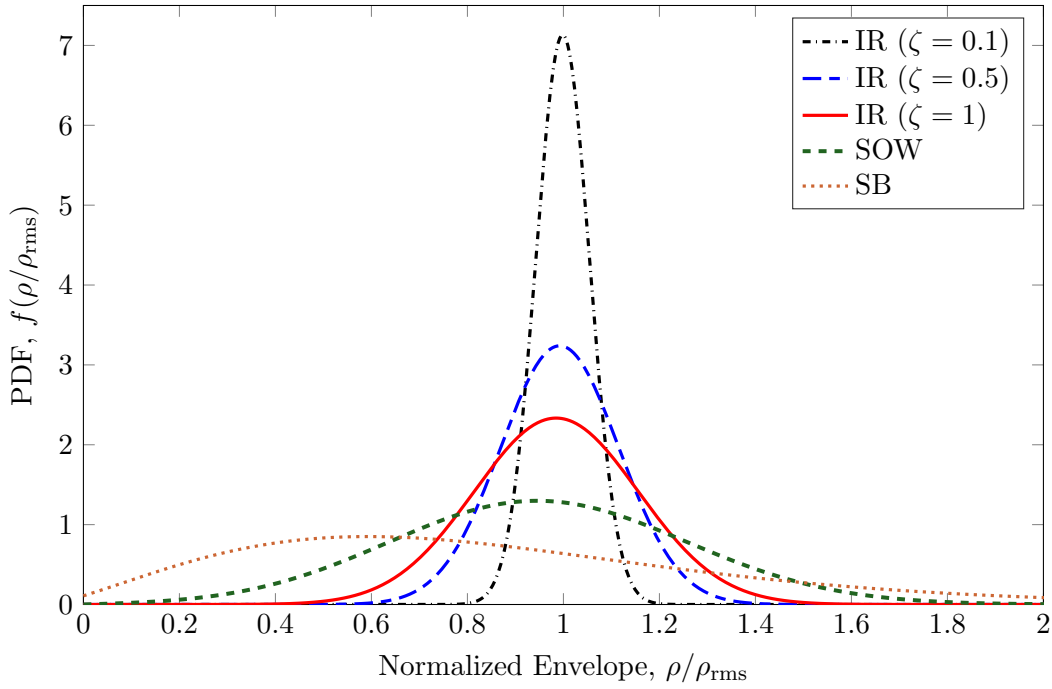

(a)

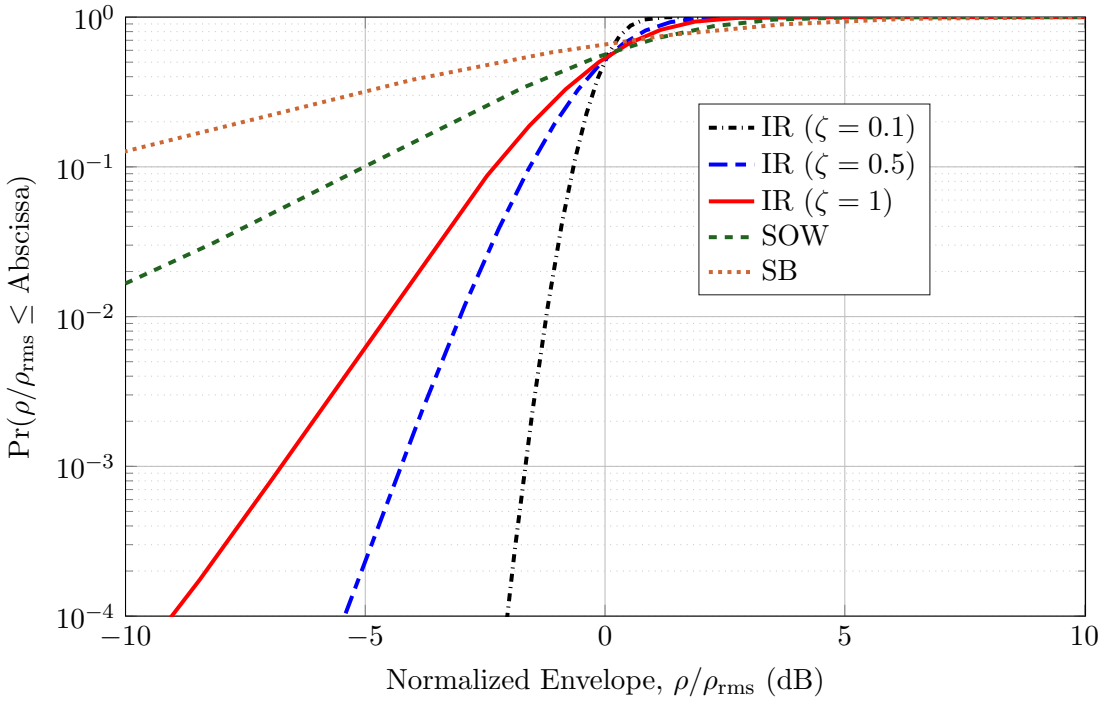

(b)

Figure 5.8: PDF's (a) and CDF's (b) versus the RMS value of the distribution when the underlying channel is Rician with $K = 6$ dB and $\sigma = 1$ (This figure is adapted from [14]; © IEEE 2019).

to find an *equivalent* diffuse component distribution by solving the following optimization problem:

$$\begin{aligned} \min_{\boldsymbol{\beta'}} \quad & \left\|\boldsymbol{\beta'}\right\| - \|\boldsymbol{\beta}\| \\ \text{s.t.} \quad & \left\|\boldsymbol{\beta'}\right\|_2^2 = 2\sigma^2 \\ & \frac{\|\boldsymbol{\beta'} \circ \boldsymbol{\beta'}\|_2^2}{\|\boldsymbol{\beta'}\|_2^4} = \zeta, \end{aligned} \tag{5.12}$$

where $\boldsymbol{\beta'} \in \mathbb{R}^M$ is a vector of the equivalent fading coefficients, $\boldsymbol{\beta} \in \mathbb{R}^{N-1}$ is the vector of the actual fading coefficients in Equation (3.8), and $\circ$ is the Hadamard product (element-wise product). In addition, N need not be the same as M.

Equation (5.12) is a generic way of finding the distributions of the diffuse components. A simpler way is to approximate the $(N-1)$ coefficients in Equation (3.8) with $(N-1)$ identical coefficients. The number of N is then

$$N = 1 + \frac{1}{\zeta}. \tag{5.13}$$

In addition, we can approximate the diffuse component coefficients using a geometric series. That is,

$$V_T = \beta_1 \exp\left(j\Phi_1\right) + \sum_{i=2}^{N} a^{i-2} \exp\left(-\Phi_i\right), \tag{5.14}$$

in which N can be found using

$$N = \ln\left(\frac{\zeta - C}{\zeta + C}\right) / \ln\left(a^2\right) + 1, \tag{5.15}$$

where $C = (1-a^2)/(1+a^2)$ and $\ln(\cdot)$ is the natural logarithm (i.e. $\ln(e) = 1$). The numbers of diffuse components in Equations (5.13) and (5.15) are derived in Appendix A.

Diffuse disparity shows that the statistics of an ideal retrodirective channel not only depend on the the underlying channel, but the statistics also depend on the fine distribution of the diffuse components. For example, assume for a specific multipath environment that

the distribution of the multipath components has the following form:

$$V_T = \beta_1 \exp(j\Phi_1) + \sum_{i=2}^{50} a^{i-2} \exp(j\Phi_i), \tag{5.16}$$

and the underlying SOW channel has a 3 dB Rician K-factor. If $a = 0.9$, then $\sigma^2 = 2.63$ and the diffuse disparity is $\zeta = 0.11$. Therefore, using Equation (5.10), the retrodirective K factor is 16 dB. If a is changed to $a = 0.5$, then $\zeta = 0.6$ and the retrodirective K factor is 8.2 dB . The standard backscatter channel, however, has a K-factor of -4 dB in both cases (using Equation (3.27)). Equation (5.16) is a realized model for multipath that assumes a geometric decay of ordered multipath amplitudes.

5.4.2 Fade Margin Analysis

A useful engineering tool in the characterization of wireless channels is to study the fade margin, which is defined as [15] (in dB scale)

$$F = -10 \log_{10} \left(\frac{[F_\rho^{-1}(\text{Outage Probability})]^2}{\rho_{\text{rms}}^2} \right), \tag{5.17}$$

where F_ρ is the CDF. The fade margin values for three channels (SOW, SB, and IR) are listed in Table 5.1 using various values of outage probability and diffuse disparity. From Table 5.1, we can observe the following:

- If $K = -\infty$ dB, which is the case of Rayleigh fading, retrodirective arrays transform the backscatter channel into a standard one-way channel. In addition, the diffuse disparity becomes irrelevant.
- When $K > 0$ dB, the fade margin of the IR channel is lower than that of its underlying SOW channel. Furthermore, the fade margin of the IR channel decreases with the decrease in the diffuse disparity.
- At moderate K such as $K = 10$ dB, the IR channel becomes almost deterministic especially when $\zeta \to 0$.

Table 5.1: Fade margin comparison between the three channels in Figure 5.6

	Outage Probability	SOW F_1 (dB)	SB F_2 (dB)	IR F_R (dB)			
				$\zeta = 1$	$\zeta = 0.7$	$\zeta = 0.4$	$\zeta = 0.1$
$K = -\infty$ dB	0.1	10	23	10	10	10	10
	0.01	20	43	20	20	20	20
	0.001	30	63	30	30	30	30
$K = 3$ dB	0.1	7	16	5	4	3	1
	0.01	16	34	12	9	6	3
	0.001	26	54	20	15	10	4
$K = 10$ dB	0.1	3	7	0.8	0.7	0.5	0.3
	0.01	6	13	1.6	1.3	1	0.5
	0.001	10	20	2	1.8	1.3	0.6

Notes: •F_1: Fade margin of the SOW channel •F_2: Fade margin of the SB channel •F_R: Fade margin of the IR channel

Graphically, Figure 5.9 sketches the results from the IR channel fade margins in Table 5.1 along with the expected amplitude distribution of the diffuse components. Table 5.1 along with Figure 5.9 are extremely useful engineering tools for gaining a physical intuition on the multipath behavior of wireless channels.

5.5 Chapter Summary

This chapter derived a theoretical model for ideal retrodirective channels. The take away points from this chapter are:

- Ideal retrodirective arrays require an infinite number of antenna elements; however, we can approximate this behavior with a reasonably large number of antenna elements if we operate at microwave and mm-wave frequencies. Since the frequency is high, the size of the array can be made practical.

- When the backscatter channel has an RFID tag equipped with an ideal retrodirective array, the backscatter channel has the same statistics as its underlying one-way channel.

- Not only do ideal retrodirective arrays eliminate the pinhole nature of backscatter channels, but they also make the channel less random compared to the underlying standard one-way channel.

- The statistics of ideal retrodirective channels depend on that of their underlying one-way channel and the amplitude distribution of the diffuse components.

- The diffuse disparity is a useful unitless quantity that can be utilized to approximate the magnitude distribution of the diffuse components.

- Unlike general multi-channel communications, backscatter communication with retrodirective arrays benefit from the correlation between the forward and backward channels. That is, the best performance is when the correlation, ϱ, is equal to one.

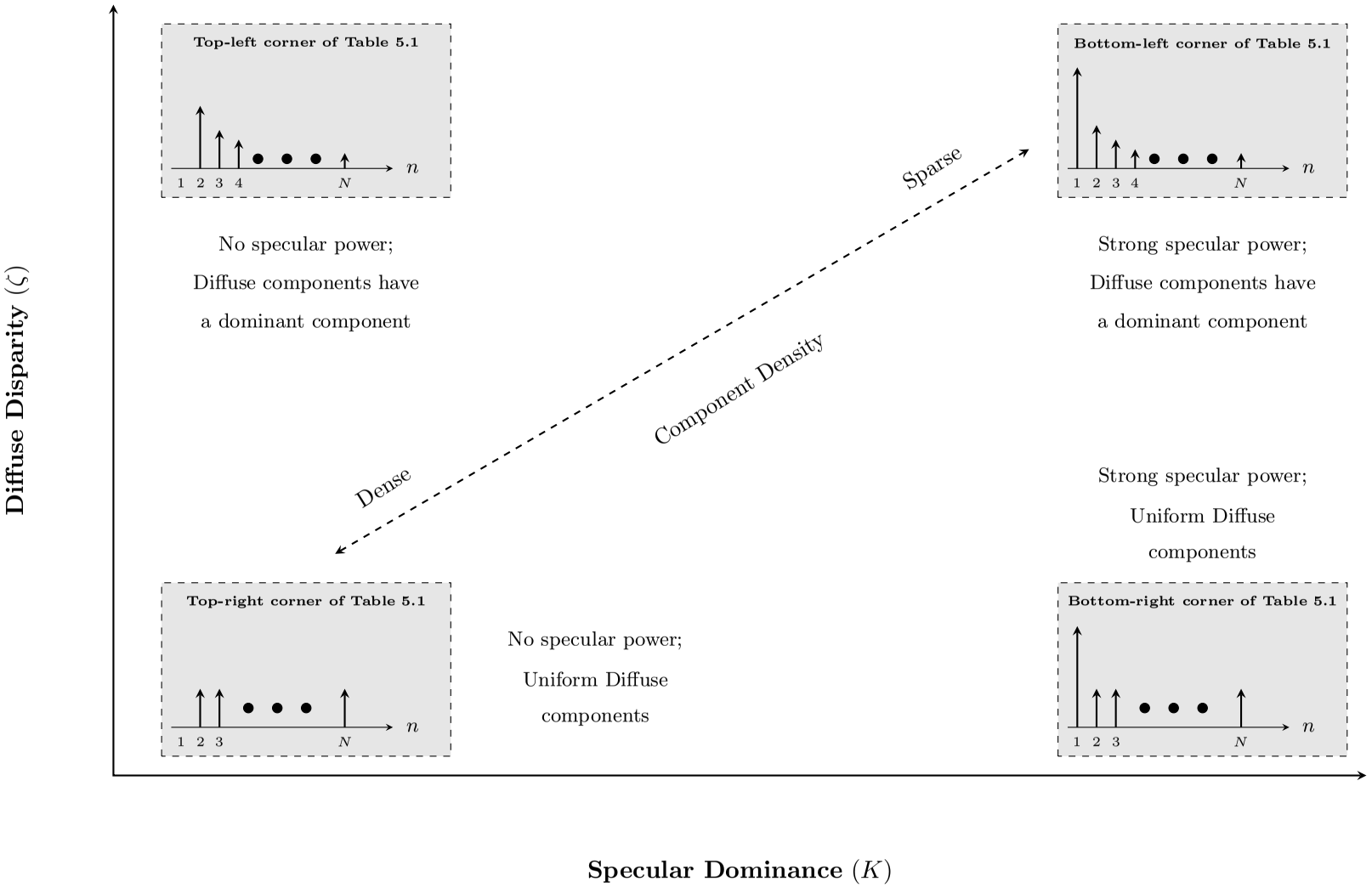

Figure 5.9: Graphical representation of the IR channel fade margin in terms of the specular dominance and diffuse disparity (This figure is adapted from [14]; © IEEE 2019).

CHAPTER 6
RETRODIRECTIVE-CHANNEL SOUNDING

The previous chapter introduced the theory of ideal retrodirective channels along with the characteristics of ideal retrodirective arrays in multipath environments. This chapter builds upon the theoretical analyses discussed in the previous chapter and conducts several channel-sounding experiments. The results in Chapter 5 suggest that retrodirective transponders will dramatically reduce fading, further improving the prospects of long-rang high-rate backscatter communications. Although the theory of the previous chapter is true for ideal retrodirective arrays that are infinite in size, this chapter studies—experimentally—the performance of the least non-ideal retrodirective arrays; that is, a two-element retrodirective array. The theory of the last chapter and the experimental results of this chapter serve as an upper and lower bound on the fading characteristics of retrodirective arrays. In particular, this chapter addresses the following points:

- The challenges associated with backscatter-channel sounding.
- The experimental PDF and CDF of retrodirective tags.
- The estimated Rician K-factors obtained from the measurements.

6.1 General Considerations for Backscatter Channel Soundings

In general, spatial fading is characterized by transmitting a narrowband signal. The narrowest band signal is an unmodulated single-tone signal, which has a bandwidth of zero [1]. However, for backscatter systems, such technique is impractical for two reasons:

1. The carrier frequency (single tone) does not carry any useful information.
2. RFID readers are, in fact, transceivers; that is, they have both transmitting and receiving chain. Therefore, even if a single tone is used, this tone will not be detected since its echo will be masked by the self-jamming signal that leaks from the transmitting to the receiving antenna.

Therefore, a modulated signal must be used.

Backscatter communication is a type of low-power communications; therefore, the SNR in backscatter systems is in general low. One cause of noise in these systems is the reader hardware noise that tends to reside close to DC. In the research literature, this noise is called the orange noise [30]; that is, hardware noise can mask the data signal when backscattering below the cutoff frequency of the orange noise. Therefore, spatial channel-sounding experiments for backscatter systems necessitates choosing a signal bandwidth high enough such that the hardware noise does not mask the desired signal and low enough such that the signal bandwidth does not exceed the channel coherence bandwidth.

Another property of backscatter channels is that the Nyquist spatial sampling is reduced by a factor of two, which results from the round-trip nature of backscatter systems [1]. In standard one-way communication systems, the maximum Nyquist sampling distance is $d_N \leq \lambda/2$. Therefore, for backscatter systems, this distance is reduced by a factor of two; that is, $d_N \leq \lambda/4$. Such reduction makes it harder to —experimentally—study spatial fading in backscatter systems at mm-wave frequencies.

6.2 Experimental Set-Up

Figure 6.1 shows a high-level block diagram of the experimental set-up, which consists mainly of three parts: The reader, tag, and a two-dimensional positioner. The reader (transceiver) is a standard homodyne receiver. This set-up studies the fading characteristics of a standard single-element tag and a two-element retrodirective tag. The following subsections discuss the set-up in further details.

6.2.1 Reader

The reader is a coherent homodyne transceiver. It sends a continuous wave (CW) at 5.8 GHz and receives a backscattered signal from the tag. In these experiments, the signal source is an Agilent (E8247C) signal generator, which generates an 11-dBm CW. The output of the signal generator is split into two parts using a Mini-Circuits (ZFRSC-183+) 6-dB splitter. One output of the splitter is fed to the IQ downconversion board while the other

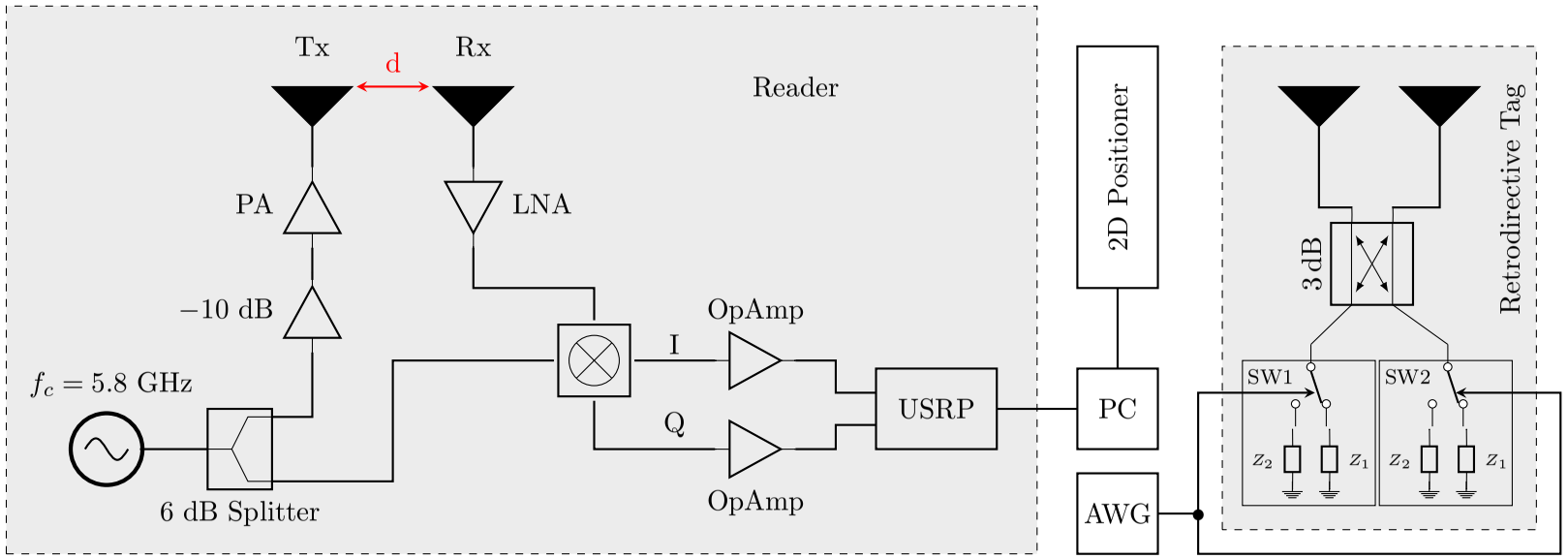

Notes:

1. The standard tag (not shown) is similar to the retrodirective tag but only one antenna and one switch (SW1) are used. Also, the branch coupler (3 dB) coupler is not used. That is, the antenna is connected directly to SW1.
2. The acronyms in the block diagram are defined as follows: •PA: Power Amplifier. •LNA: Low-Noise Amplifier. •I: In-Phase channel. •Q: Quadrature-Phase Channel. •PC: Personal Computer •AWG: Arbitrary-Waveform Generator. •SW: RF Switch

Figure 6.1: A high-level block diagram of the experimental setup.

Figure 6.2: A photograph of the reader.

passes through a Mini-Circuits VAT-10+ 10 dB attenuator. The use of the attenuator is necessary to avoid saturating the power amplifier, which is a 34-dB gain Mini-Circuits ZVE-8G+. The remaining parts of the reader except the USRP are custom built and further discussed in Appendix C. The reader is photographed in Figure 6.2.

6.2.2 Transmitted Data

In the set-up of Figure 6.1, the tag is connected to RF switches (or an RF switch in the case of the single antenna). The TTL signal of these switches is supplied by an arbitrary waveform generator (Agilent 33522A). When choosing the data sequence, two competing strategies are considered:

1. The data sequence should have good correlation properties, which increases the coding (processing) gain and reduces the noise floor since the noise is assumed to be uncorrelated.

2. The data sequence should have a zero mean; in other words, the sequence code should be balanced [103].

If only the first strategy is considered, then the best data sequence would be a pseudo random (PN) m-sequence direct sequence spread spectrum (DSSS). However, one key property of m-sequence codes is that they have more 1's then 0's; hence the code is not balanced. Another option would be to use Walsh-Hadamard codes, which are balanced and have good autocorrelation properties. Recall that the 8×8 Hadamard matrix is [67]

$$\boldsymbol{H}_8 = \begin{bmatrix} 1 & 1 & 1 & 1 & 1 & 1 & 1 & 1 \\ 1 & -1 & 1 & -1 & 1 & -1 & 1 & -1 \\ 1 & 1 & -1 & -1 & 1 & 1 & -1 & -1 \\ 1 & -1 & -1 & 1 & 1 & -1 & -1 & 1 \\ 1 & 1 & 1 & 1 & -1 & -1 & -1 & -1 \\ 1 & -1 & 1 & -1 & -1 & 1 & -1 & 1 \\ 1 & 1 & -1 & -1 & -1 & -1 & 1 & 1 \\ 1 & -1 & -1 & 1 & -1 & 1 & 1 & -1 \end{bmatrix}. \tag{6.1}$$

The last row of Equation (6.1) is used as a TTL signal. That is, the data vector is

$$\boldsymbol{s} = \begin{bmatrix} 1 & -1 & -1 & 1 & -1 & 1 & 1 & -1 \end{bmatrix}. \tag{6.2}$$

In these experiments, the chip rate of the sequence in Equation (6.2) is 1 MHz, which yields a sequence rate of 125 kHz. The chip rate is well below the reported coherence bandwidth of the channel in [104] and [54] at 5.8 GHz; therefore, the communication is narrowband. With these specification, Figure 6.3 plots the time-domain data sequence in Equation (6.2) along with its spectrum, which shows that the sequence has a deep null near DC. In addition, Figure 6.3 plots a simulated spectrum of the carrier frequency. Furthermore, an actual sequence of the received complex data is shown in Figure 6.4

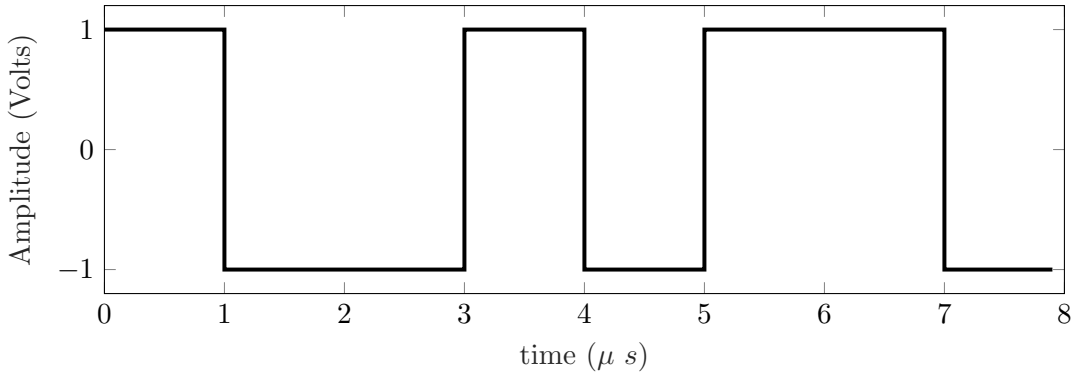

(a)

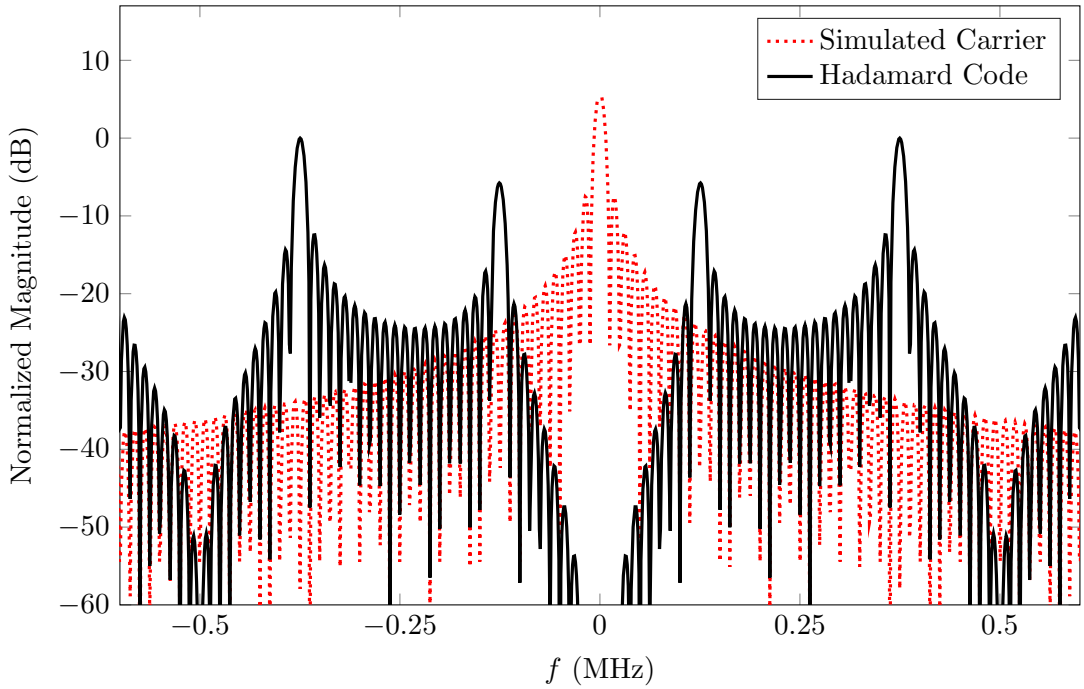

(b)

Figure 6.3: (a) A one-period of Equation (6.2). (b). The normalized spectrum of Equation (6.2) when the sequence is repeated ten times (10 periods of Equation (6.2)) and a simulated carrier location. The simulation is generated by changing the mean of the data in Equation (6.2). The normalization is done with respect to the data spectrum (black curve).

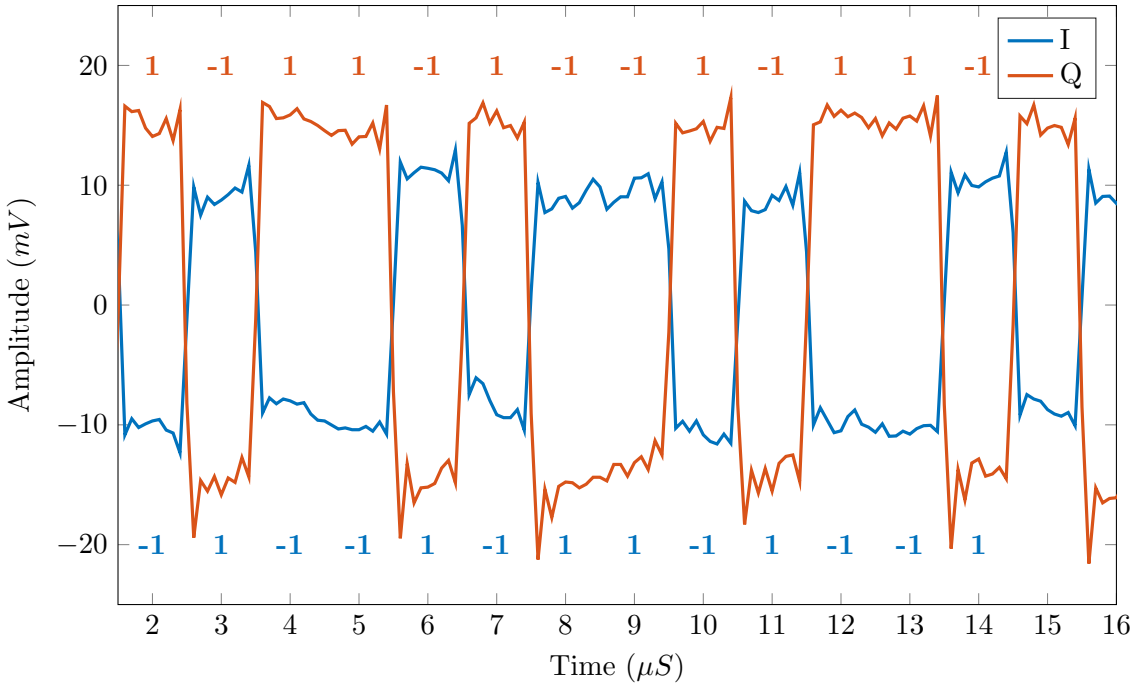

Figure 6.4: Sample in- and quadrature-phase time-domain signals. Those samples are obtained from the measurements when the tag is retrodirective. As shown in the figure, the I channel is 180° out of phase with respect to the Q channel.

6.2.3 Reader Antenna Spacing (d)

The distance between the transmitting and receiving antenna in the RFID reader of Figure 6.1, denoted d, controls the forward and backward channel correlation. Recall from Chapter 3 that for general backscatter systems, fading is less severe when the forward and backward channels are decorrelated. However, Chapter 5 shows that this is not the case when the tag is retrodirective. That is, fading is less severe when the channels are correlated. In these experiments, we used two values of d: $d = 29$ cm and 15.5 cm, which correspond to approximately 5.6λ and 3λ at $f_c = 5.8$ GHz, respectively.

The transmitting and receiving antenna are probe-fed patch antennas aligned along the patch E-plane. Therefore, the angular spread that contributes to the correlation is that of the elevation. To find the decorrelation distance, R_λ, in wavelengths, we use the following

formula [53]:

$$R_\lambda = \frac{1}{\Lambda}\sqrt{\frac{-\ln \varrho}{0.23(1-\gamma)}}, \tag{6.3}$$

where Λ is the shape factor angular spread, γ is the angular constriction, and ϱ is the correlation coefficient. In addition, the mathematical definitions of λ and γ are [53]:

$$\Lambda = \sqrt{1 - \frac{|F_1|^2}{F_0^2}} \tag{6.4}$$

and

$$\gamma = \frac{\left|F_0 F_2 - F_1^2\right|^2}{F_0^2 - |F_1|^2}, \tag{6.5}$$

where F_n is defined as [53]

$$F_n = \int_0^{2\pi} p(\theta) \exp(jn\theta), \tag{6.6}$$

where $p(\theta)$ is the angular distribution of the multipath power. For the antennas in this experiment, the theoretical normalized angular function is [105]

$$p(\theta) = \cos^2(0.2\pi \sin(\theta)), \quad -\pi/2 \leq \theta \leq \pi/2. \tag{6.7}$$

Evaluating Equations (6.3)–(6.6) yields $\Lambda = 0.73$ and $\gamma = 0.31$ and a correlation distance, R_λ, of 2.9λ and 5.2λ for $\varrho = 0.5$ and 0.1, respectively. The reader antennas in both cases are pictured in Figure 6.5.

6.2.4 Tags and RF Modulators

Since from Figure 4.24, both the rat-race- and branch-line-based retrodirective tags have similar behavior, one of them can be used for channel sounding. Thus, for simplicity, we used the branch-line retrodirective array.

The RF switches are those used in Chapter 4. The modulation factor of these switches

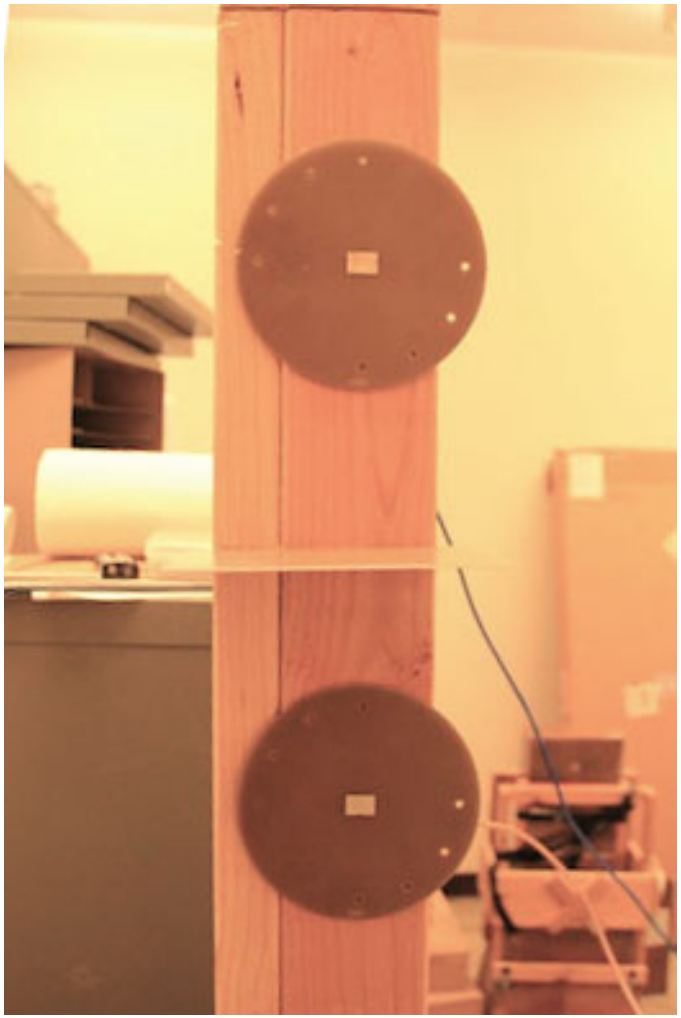

(a)

(b)

Figure 6.5: Photographs of the reader antennas. (a) Decorrelated system ($d = 29\ cm$). (b) Correlated system ($d = 15.5\ cm$). The metal plate is used to further isolate the transmitting and receiving chain.

can be estimated from the measured return loss as outlined by Equation (4.26), which results in an approximately 0.07 or equivalently, -12.4 dB. Tags are pictured in Figure 6.6 and further discussed in Appendix D.

Each tag is mounted atop a two-dimensional positioner that traverses a 21-cm by 21-cm square grid, roughly $4\lambda \times 4\lambda$. The tag moves in a 1-cm increment and the received complex signal is recorded at each spatial location. This incremental movement corresponds to a sampling distance of 0.19λ, well below the Nyquist two-way spatial sampling rate [1], which is $\lambda/4$. This fine sampling results in 484 distinct points where the signal envelope is evaluated.

6.2.5 Two-Dimensional Positioner

The two-dimensional positioner used in these experiments is pictured in Figure 6.7. The positioner is controlled on Python and the control code is in Appendix B. The grid that the positioner traces is labeled following the convention in Figure 6.8. This convention is used throughout the remaining analyses.

6.2.6 Measurement Scenes

To diversify the measurements, four sets of measurements are conducted, which are:

1. An unobstructed LoS geometry with decorrelated forward and backward channels ($d = 29$ cm). This experiment is pictured in Figure 6.9. This experiment is denoted as Experiment #1.

2. A partially blocked LoS geometry with decorrelated forward and backward channels ($d = 29$ cm). The tags and reader are in different rooms. Furthermore, the wall that separates the two rooms contains a steel truss and the receiving antenna of the reader is right in front of one of these truss joints. This experiment is pictured in Figure 6.10. This experiment is denoted as Experiment #2.

3. An obstructed LoS geometry with correlated forward and backward channels ($d = 15.5$ cm). The tags and reader are also in different rooms but neither the transmitting nor the receiving antenna of the reader is facing any of the truss joints. The reader

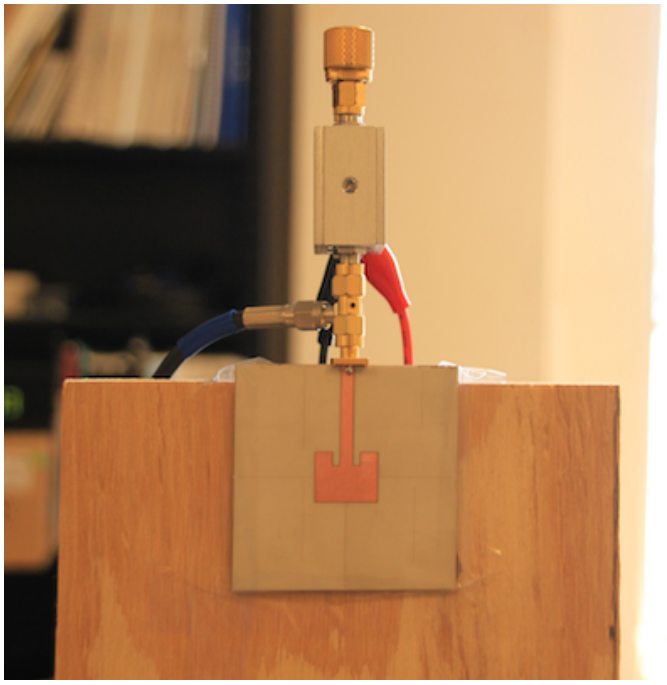

(a)

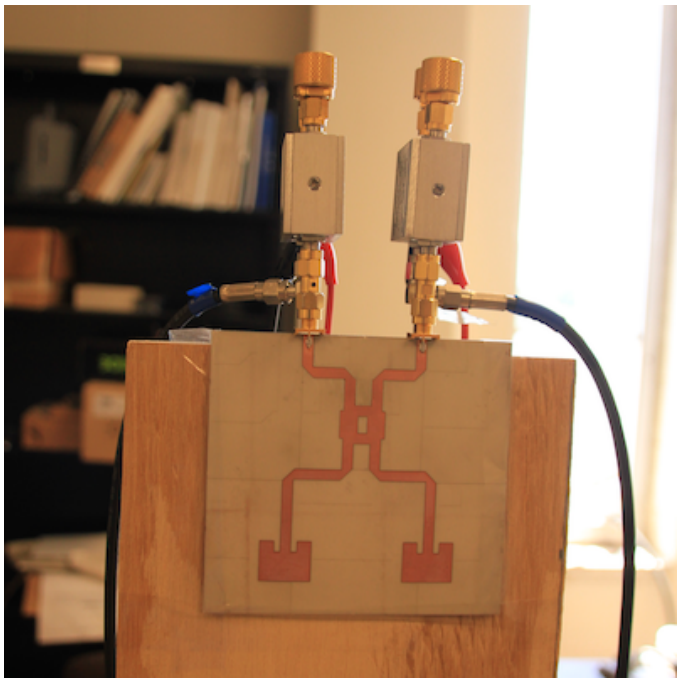

(b)

Figure 6.6: Photographs of the tags used in the experiments. (a) Standard tag. (b) Retrodirective tag.

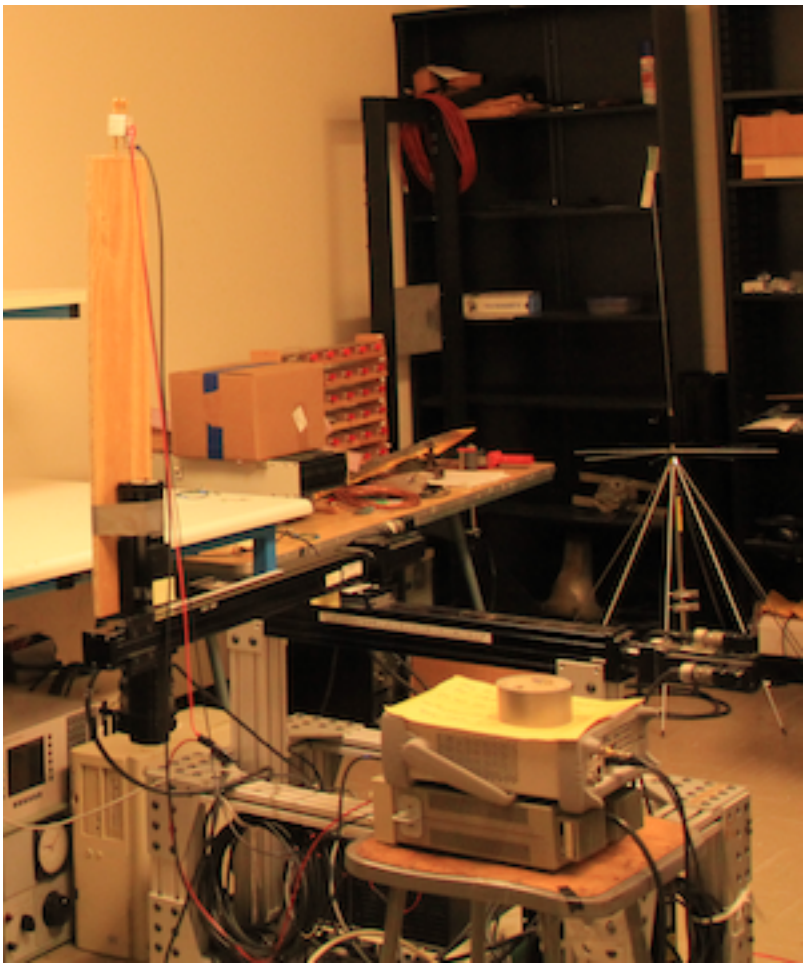

Figure 6.7: A photograph of the two-dimensional positioner used in the experiments.

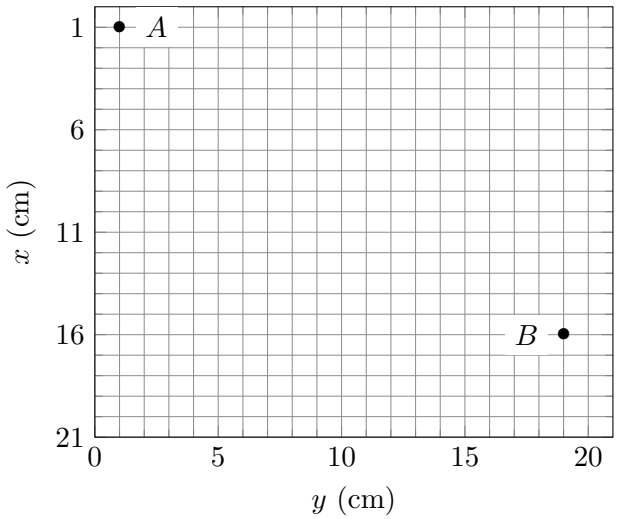

Figure 6.8: The positioner two-dimensional grid. The coordinate of point A is $(1, 1)$ while that of point B is $(16, 19)$.

in this experiment is pictured in Figure 6.5-(b) and the tag is identical to that in Figure 6.10. This experiment is denoted as Experiment #3.

4. An unobstructed LoS geometry with correlated forward and backward channels ($d =$ 15.5 cm). This experiment is conducted in a different location. This experiment is pictured in Figure 6.11. Also, this experiment is denoted as Experiment #4.

The measurement scene for the first three experiments is depicted in Figure 6.12 while that of the fourth experiment is depicted in Figure 6.13.

Each experiment is conducted twice, once for a standard tag and the other for a retrodirective tag. Each experiment run takes about eight hours. To ensure that the channel is static, each experiment is conducted overnight.

6.2.7 Data Processing

The received, demodulated signal is collected using an N200 USRP interfaced with GNU Radio and stored in a complex-binary format. In addition, the received data at the USRP are sampled at 10 MSps, which results in 10 samples per symbol. This dense sampling reduces the necessity for time-error correction, which is a challenging process since the transmitted pulses are not Nyquist pulses. The raw data will be publicly available at [106].

The received data are post-processed in MATLAB. Since the received signal is complex, a matched filter is applied to each individual channel. The matched filter outputs are averaged over 100 periods and that average is used to estimate the envelope and phase of the received signal. The PDF of each experiment is estimated using `ksdensity` function in MATLAB, then the estimated PDF is integrated to get the experimental CDF.

6.3 Results

Figures 6.14–6.17 show the measured PDF's and CDF's for the four experiments. Moreove, the heat-maps in Figures 6.18–6.21 depict the location of constructive and destructive interference patterns in the received signal power. The measurements in Figures 6.18–6.21 are normalized by the RMS power in order to maintain a fair point of comparison between these systems. From these plots, we can deduce the following:

Figure 6.9: A photograph of Experiment #1 scene. The reader antenna is pictured in Figure 6.5-(a).

(a)

(b)

Figure 6.10: Photographs of Experiment #2 scene. (a) The reader. (b) The tag.

Figure 6.11: A photograph of Experiment #4 scene. The reader antenna is pictured in Figure 6.5-(b).

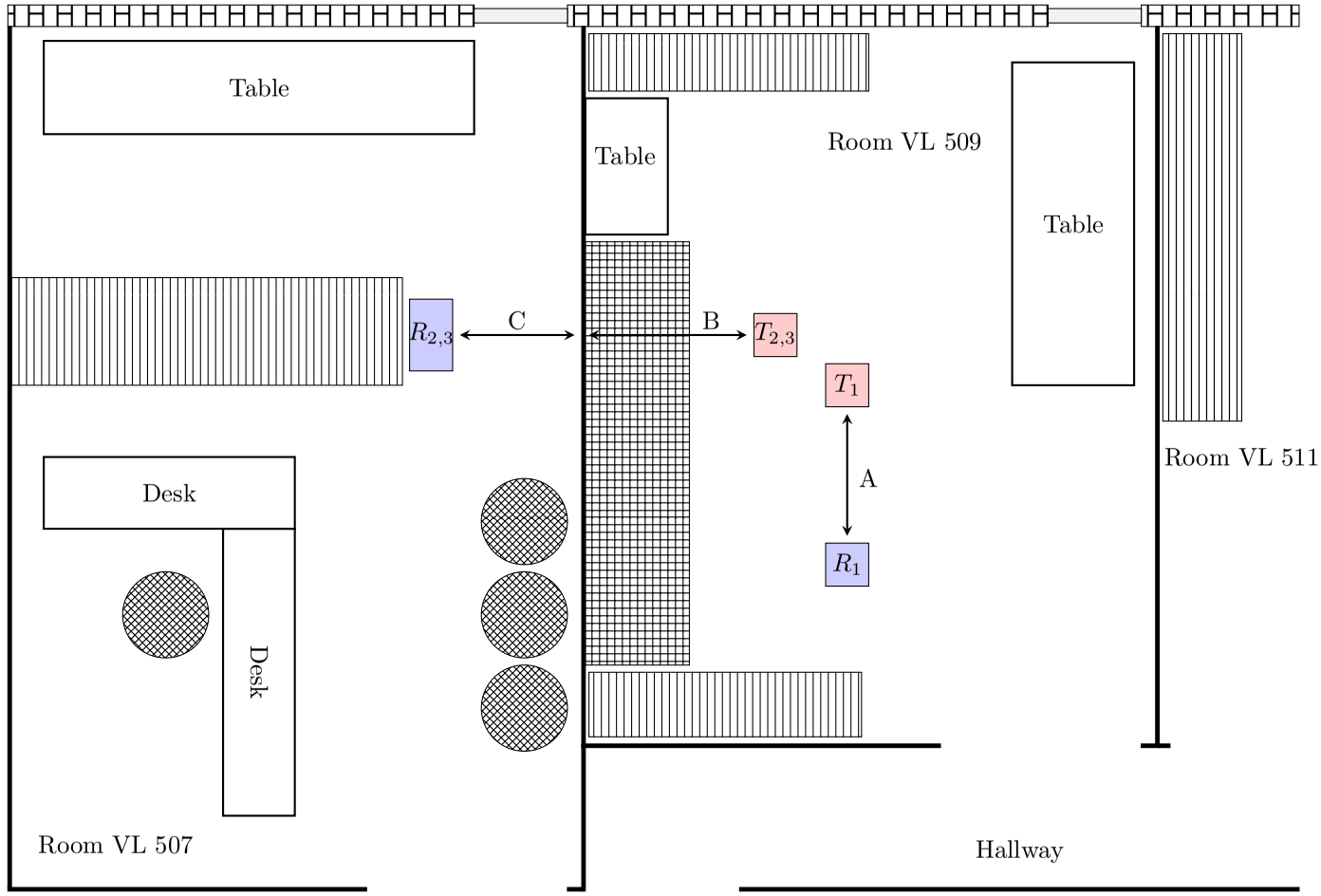

Figure 6.12: A layout of Experiments #1, #2, and #3. The rooms contain clutters that are not shown in the simple layout. In addition, the subscript in R_x and T_x indicates the location of the reader and tag at experiment #x (drawing is not to scale).

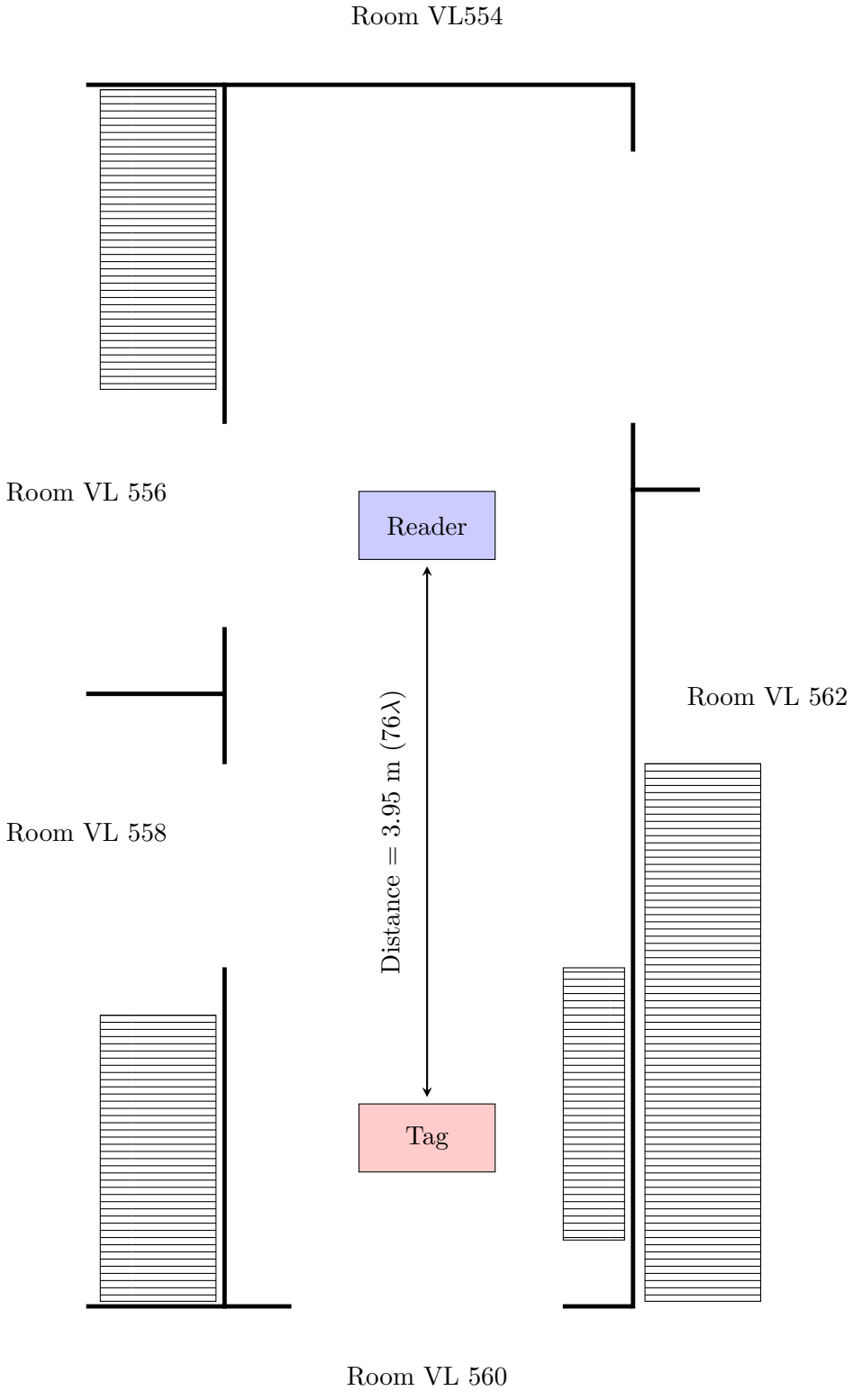

Figure 6.13: Experiment #4 scene. The hashed lines are metallic shelves (drawing is not to scale).

- When the underlying Rician channels have high Rician K-factors, the link quality of retrodirective tags is better than that of their standard counterparts. This behavior can be also observed from the heat-map in Figure 6.18, which shows that deep nulls are more pronounced in the case of the standard tag. In addition, this scenario—unobstructed LoS and decorrelated channels—is the best case scenario for a standard tag and one of the worst scenarios for a retrodirective tag. Nonetheless, the link quality of the retrodirective channel outperforms that of its standard counterpart. Although the receiving antenna of the reader—in theory—should not capture any backscattered signal from the retrodirective tag, this experiment shows otherwise. Two reasons caused such slight disagreement between the theory and measurements: First, the absence of the received signal at the reader requires that the forward and backward channels be *completely* decorrelated; however, the calculated correlation coefficient, ϱ, is approximately 0.1. Therefore, the forward and backward channels are weakly correlated. Second, the absence of the received signal at the reader also requires an ideal retrodirective tag, which in turn should have $N \to \infty$ elements. The retrodirective tag considered in this experiment is the least ideal one ($N = 2$).

- One of the key properties of retrodirective tags is that they reduce the deep nulls observed in the case of their standard counterparts. Consider the second experiment, where the backward channel is partially blocked by the wall steel truss joint. The number of nulls in the case of the retrodirective tag—referring to Figure 6.19—is not as many as those in the case of the standard tag. In addition, referring to Figure 6.12, the metallic book shelf in Room VL509 and that in Room VL511 cause a standing wave pattern that is more pronounced in the case of the standard tag. Therefore, despite the fading severity, retrodirective tags reduce the number of deep nulls observed in their standard counterparts.

- Retrodirective tags benefit from the increase in the forward and backward channel correlation. The behavior is observed in the CDF gap between the first experiment (Figure 6.14) and that in the third experiment (Figure 6.16). Therefore, contrary to the standard multi-channel communications, retrodirective tags leverage the channel

correlation.

- The last experiment (Experiment #4) also shows that retrodirective tags reduce the number of the deep fading nulls. However, the estimated PDF's from this experiment do not lend themselves into a well-known distribution. The reason behind this peculiar behavior is that the tag is in close proximity to metallic shelves, which increases the number of the specular multipath components. This behavior is similar—conceptually—to that studied in [60] in which the two specular components in the TWDP geometry cancel each other.

In addition, the noise floor at the output of the matched filter is measured to be -65 dBm. The main contributor to the noise is the USRP. Furthermore, in order to minimize the envelope error, we only include the values of the signal power that are at least 20 dB above the noise floor in the PDF estimation [1]; that is, the minimum received power is -45 dBm. In these set of experiments, two points in the second experiment when the tag is not retrodirective, two points in the fourth experiment when the tag is retrodirective, and three points in the fourth experiment when the tag is not retrodirective fall below that threshold; therefore, these points were excluded.

6.3.1 Estimated K-Factor

To add more physical insights, we estimated the Rician K-factors for Experiments #1 and #3 and listed the estimates in Tables 6.1–6.3. In the case of the retrodirective channel, we assume that—although not accurate—the retrodirective channel is an ideal retrodirective channel and estimate the Rician K-factor of that channel. This assumption becomes closer to the true value in the case of correlated forward and backward channels (Experiment #3). On the other hand, in the case of a standard backscatter channel, we estimated the Rician K-factor of the underlying channel assuming decorrelated channels (Table 6.3) and fully correlated channels (Table 6.2). Such estimates give an upper and lower bound of the actual underlying channel Rician K-factor. In all of these estimates, we minimized the mean-square error of the CDF when the normalized envelope obeys the following inequality: $0.1 \leq \rho/\rho_{\text{rms}} \leq 2$. In addition, we excluded the results from Experiments #2

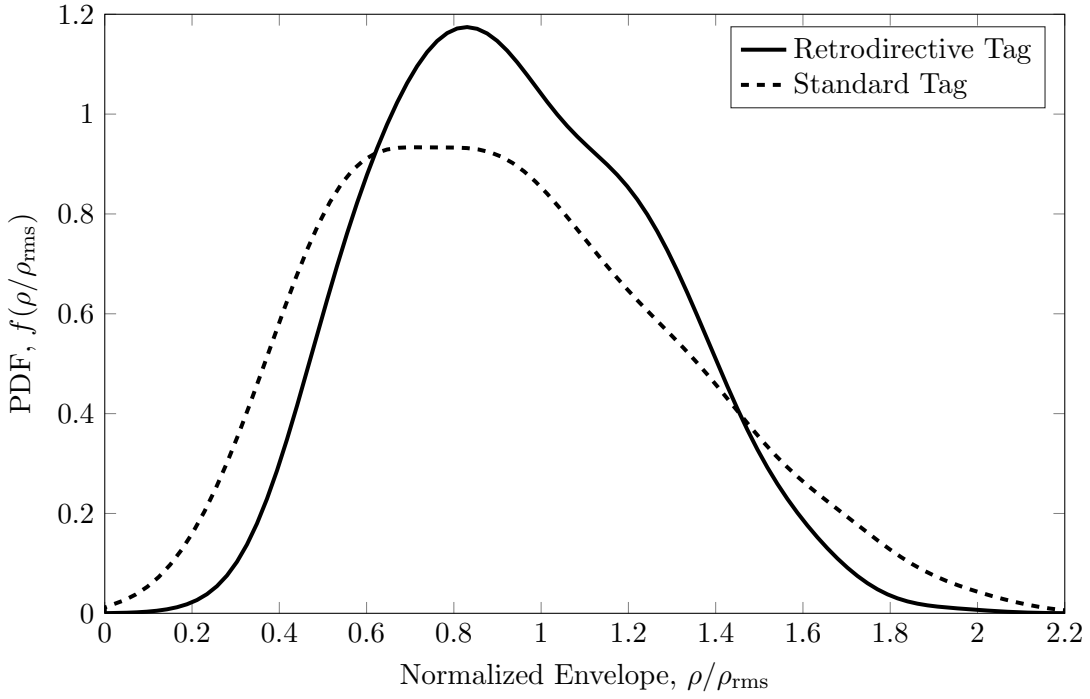

(a)

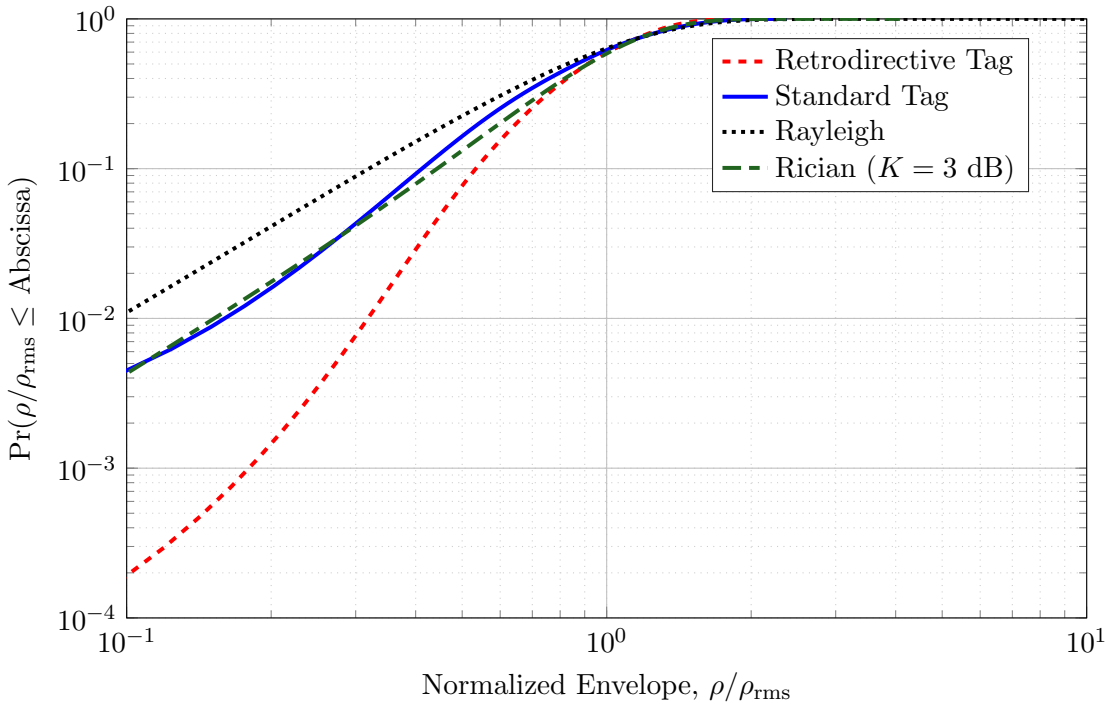

(b)

Figure 6.14: PDF's and CDF's of Experiment #1 (Unobstructed LoS with decorrelated channels in a laboratory room).

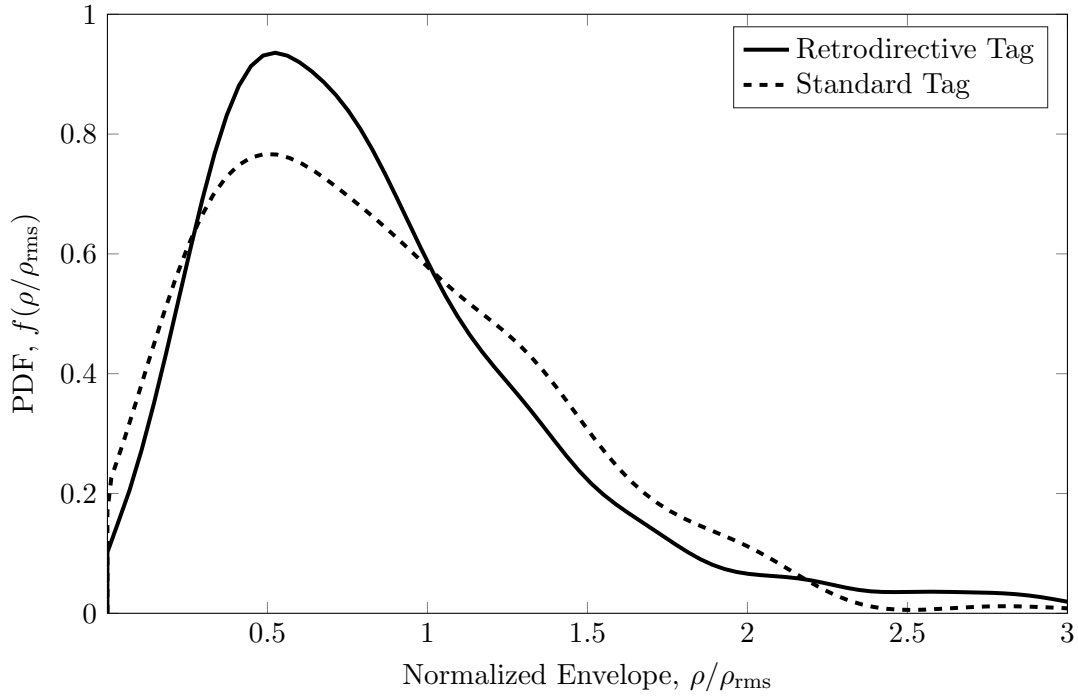

(a)

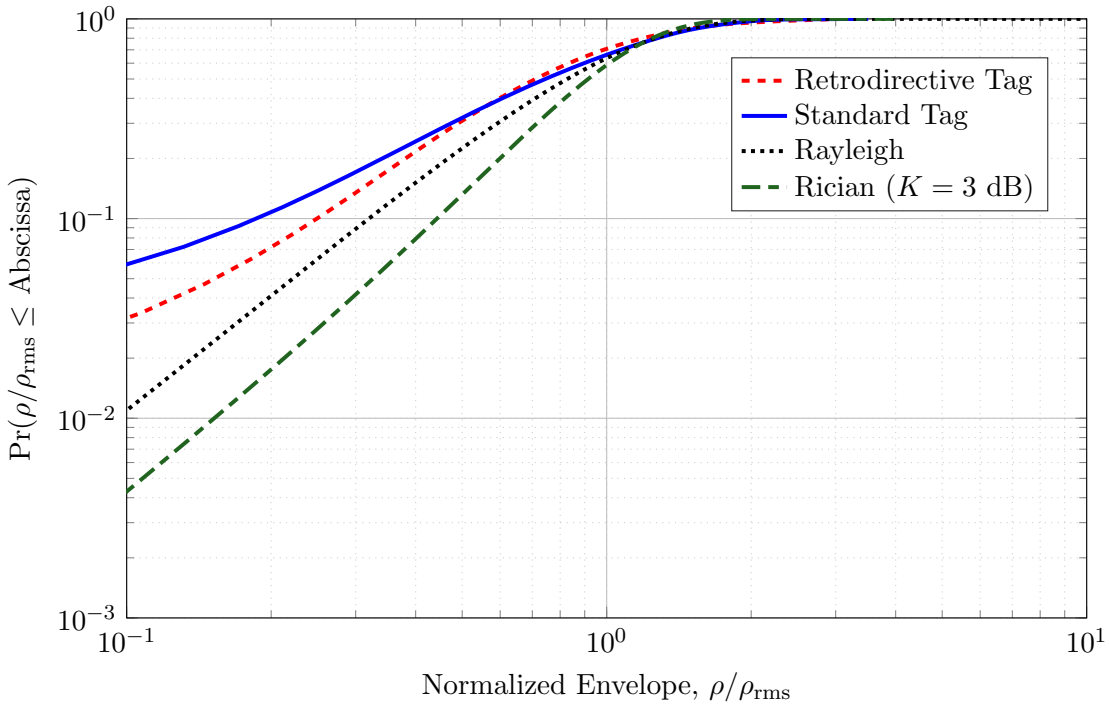

(b)

Figure 6.15: PDF's and CDF's of the Experiment #2 (obstructed LoS with decorrelated channels)

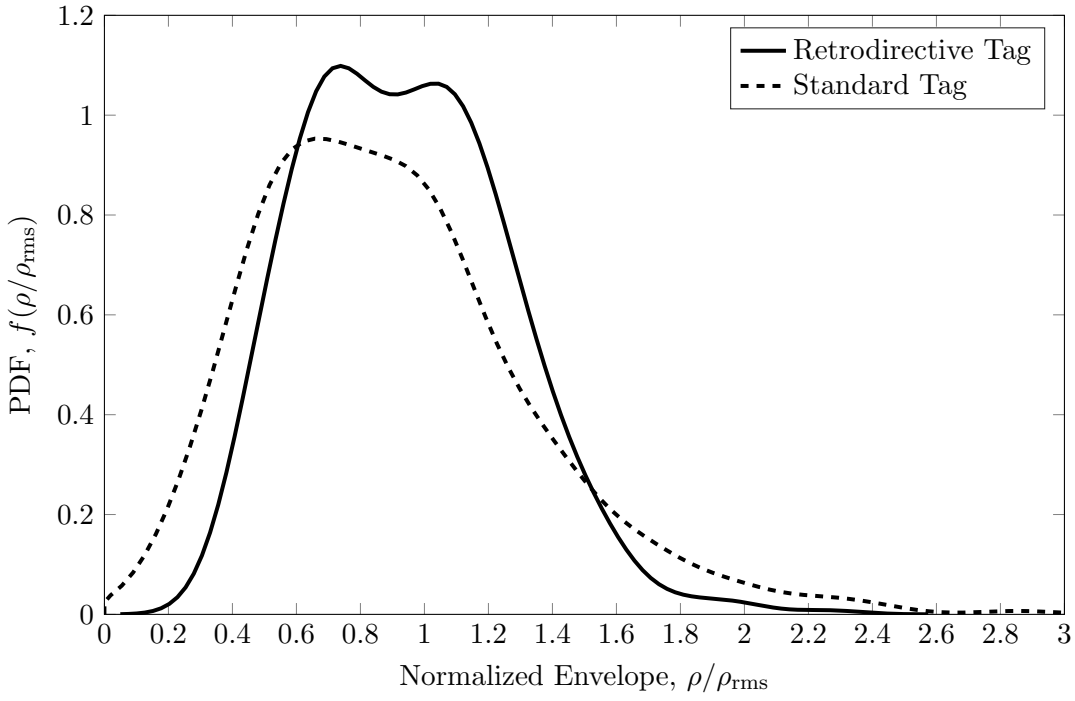

(a)

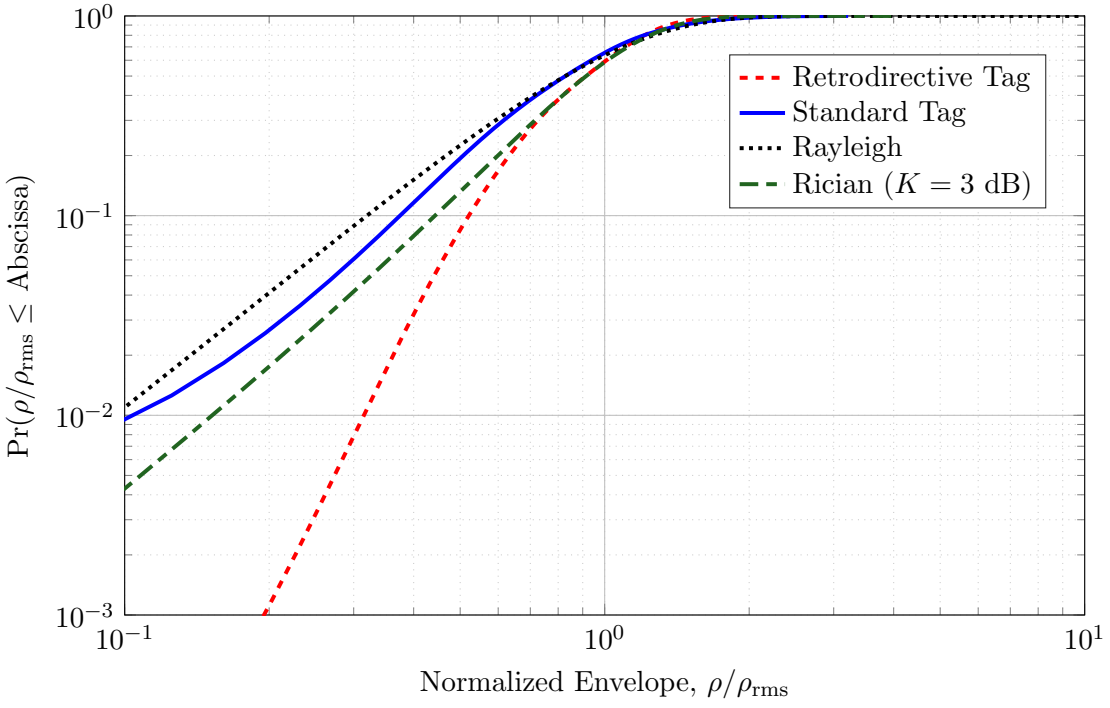

(b)

Figure 6.16: PDF's and CDF's of Experiment #3 (obstructed LoS with correlated channels)

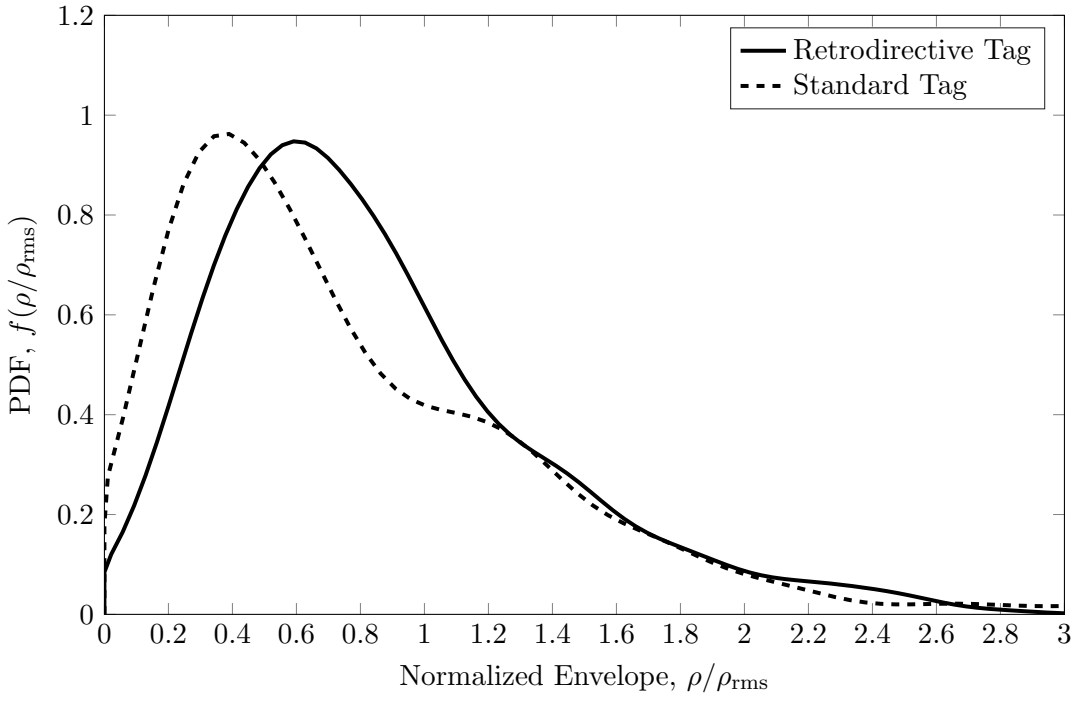

(a)

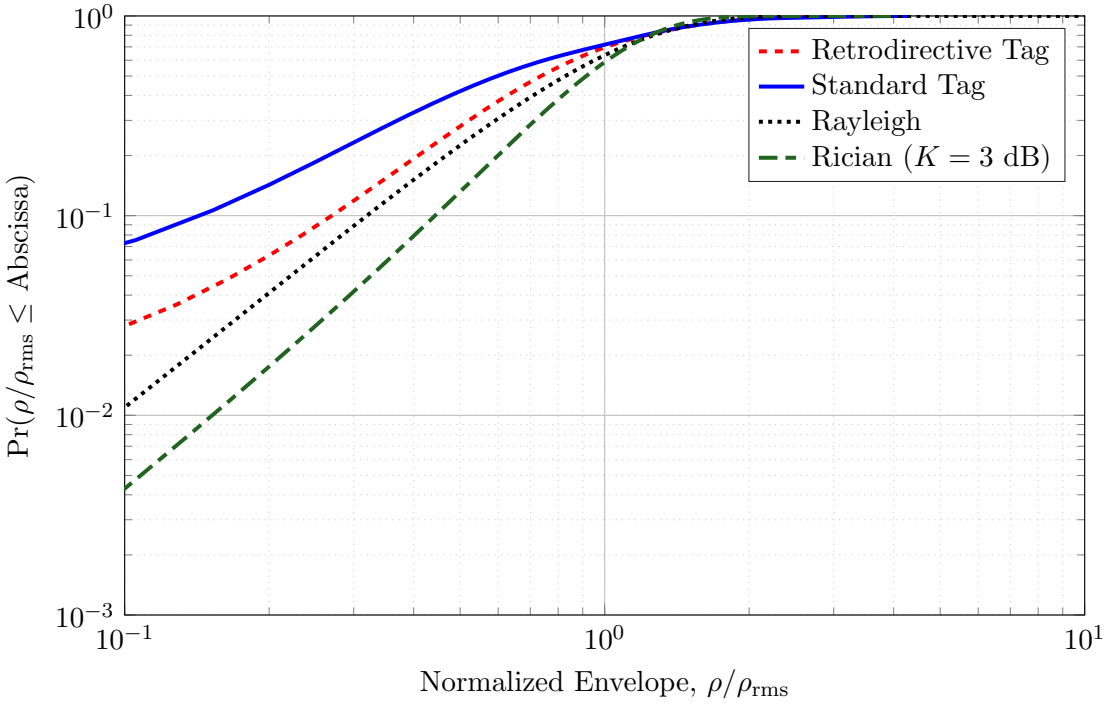

(b)

Figure 6.17: PDF's and CDF's of Experiment #4.

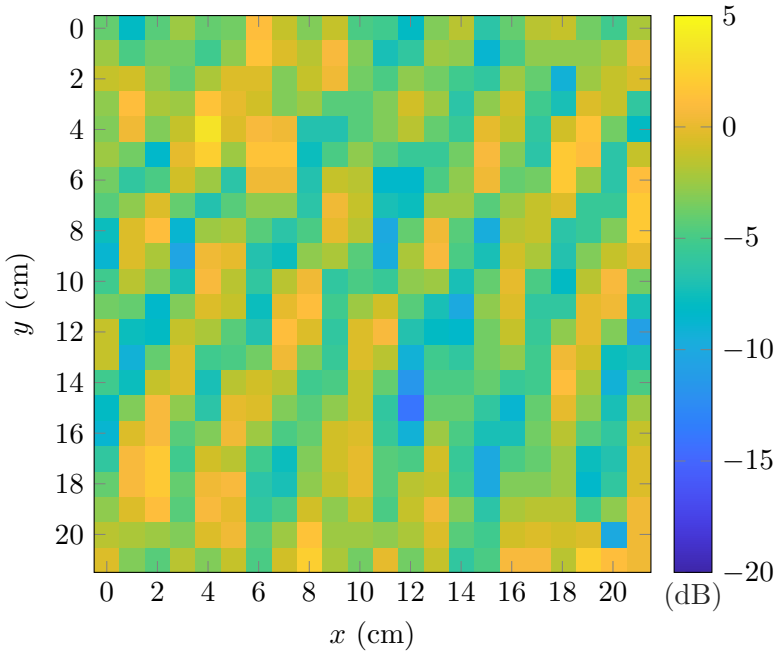

(a)

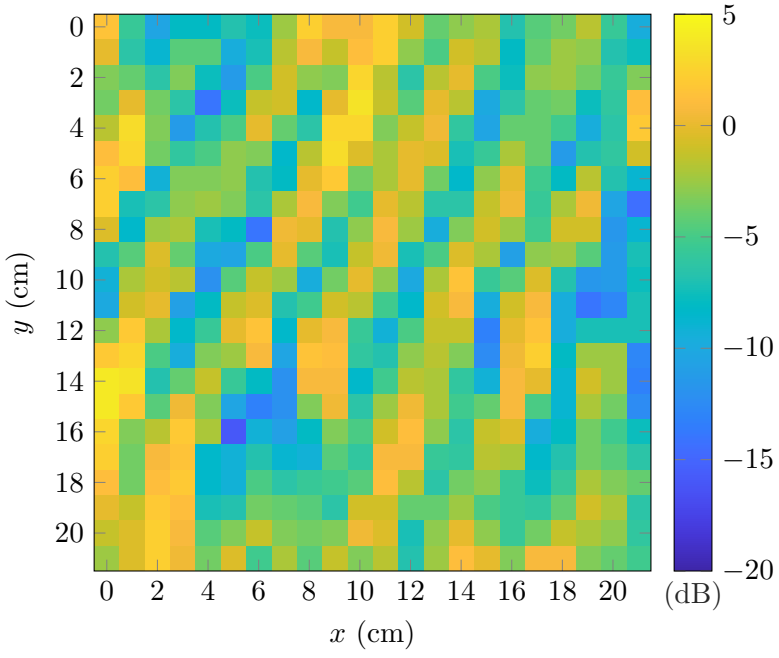

(b)

Figure 6.18: A log-scale heat-map of the normalized received power (normalized by the RMS value of each case) at each grid point for Experiment #1. (a) Retrodirective tag. (b) Standard Tag.

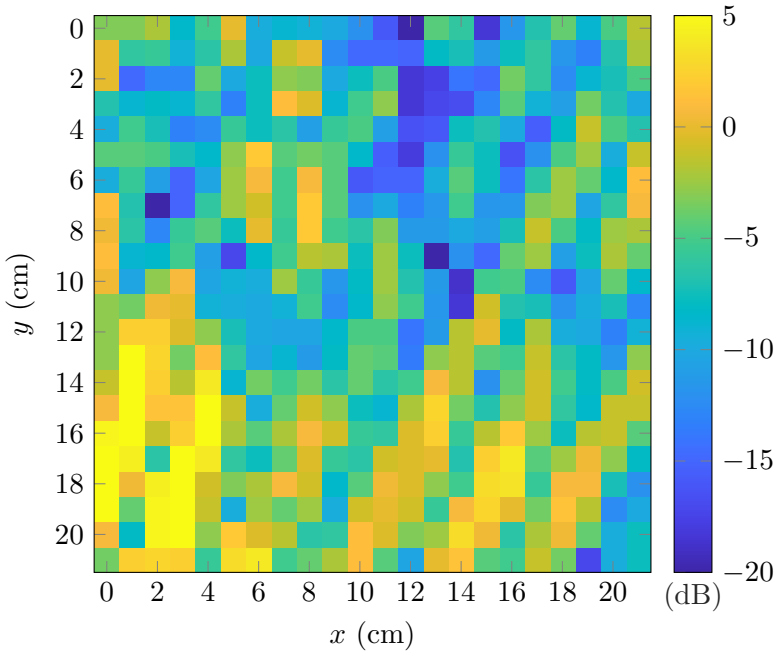

(a)

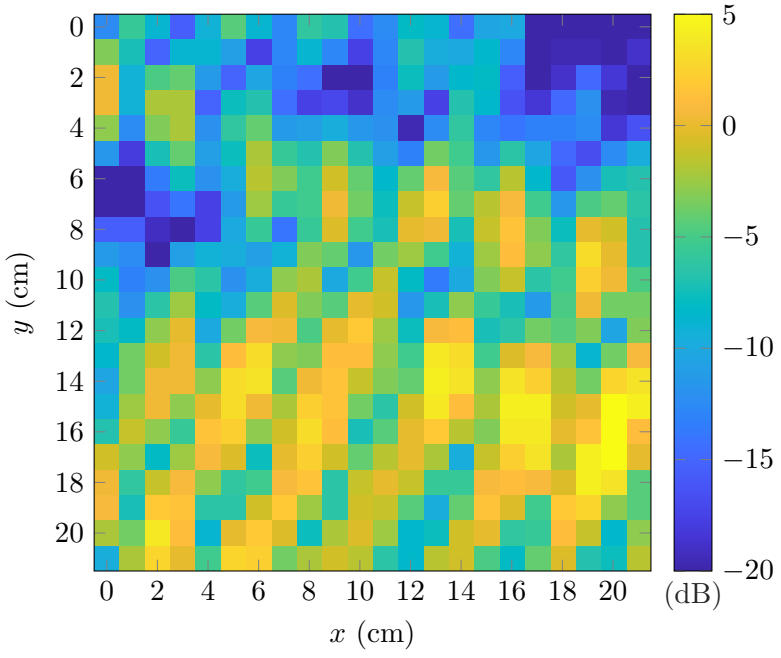

(b)

Figure 6.19: A log-scale heat-map of the normalized received power (normalized by the RMS value of each case) at each grid point for Experiment #2. (a) Retrodirective tag. (b) Standard Tag.

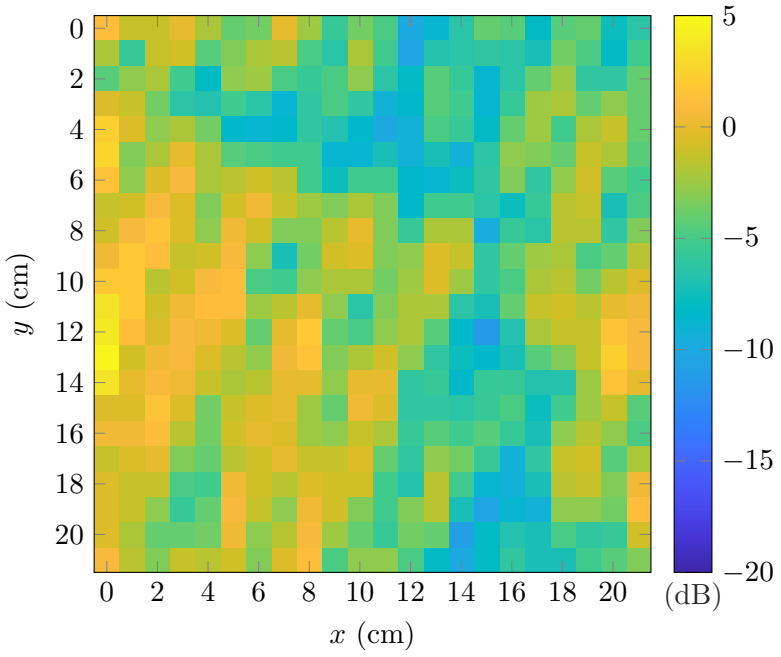

(a)

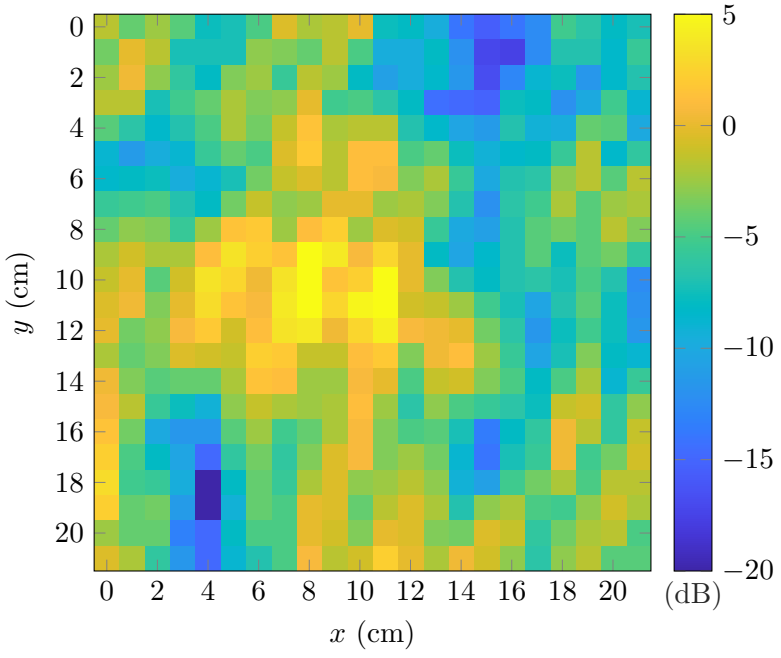

(b)

Figure 6.20: A log-scale heat-map of the normalized received power (normalized by the RMS value of each case) at each grid point for Experiment #3. (a) Retrodirective tag. (b) Standard Tag.

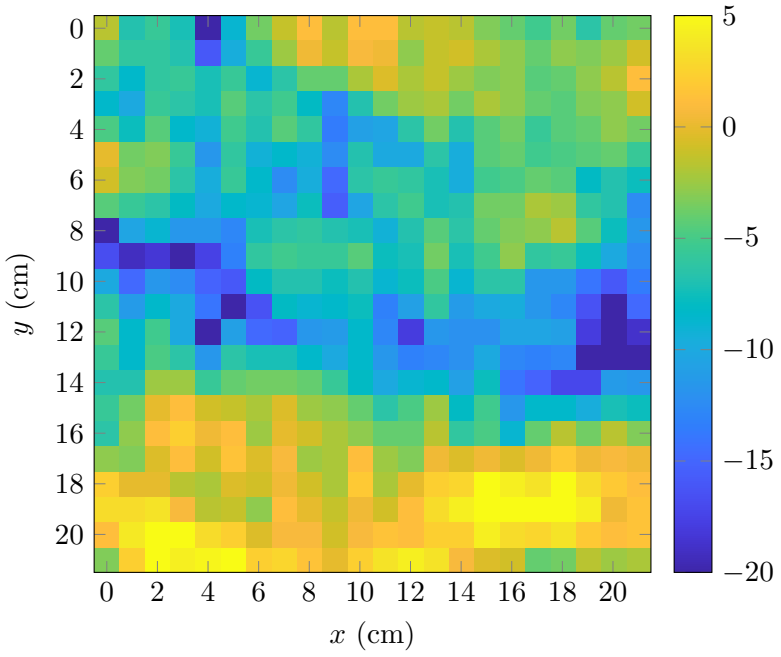

(a)

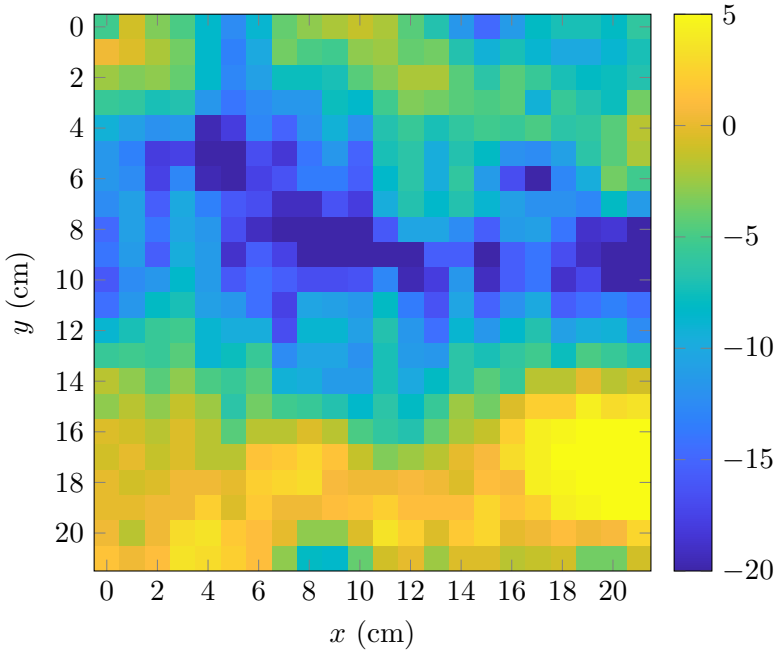

(b)

Figure 6.21: A log-scale heat-map of the normalized received power (normalized by the RMS value of each case) at each grid point for Experiment #4.. (a) Retrodirective tag. (b) Standard Tag.

Table 6.1: Estimated K-factor for Experiments #1 and #3 (Retrodirective Tag)

Experiment #	Estimated K-factor (dB)	MMSE
1	4.9	1.5×10^{-5}
3	4.65	1.3×10^{-4}

Table 6.2: Estimated K-factor for Experiments #1 and #3 (standard tag) assuming the forward and backward channel are fully correlated ($\varrho = 1$). This K-factor is for the underlying channel.

Experiment #	Estimated K-factor (dB)	MMSE
1	9	2.8×10^{-3}
3	8.5	1.2×10^{-4}

and #4 in the estimation since the distribution in the former is akin to the product Rice-Rayleigh distribution and the latter is not a Rician channel. Furthermore, if we take—in these experiments—the best case scenario of the standard tag (Figure 6.14) and that of the retrodirective tag (Figure 6.16) and compare their fade margins under 0.001 outage probability, the fade margin of the standard tag is 34 dB while that of the retrodirective tag is only 13 dB.

6.4 Chapter Summary

The focus of this chapter is on the channel sounding of retrodirective and standard backscatter systems. The take away points from this chapter are:

Table 6.3: Estimated K-factor for Experiments #1 and #3 (standard tag) assuming the forward and backward channel are decorrelated ($\varrho = 0$).

Experiment #	Estimated ($K_f = K_b$)-factor (dB)	MMSE
1	6.5	2.1×10^{-4}
3	5.6	1.1×10^{-4}

- Unlike that of the standard one-way communications, studying spatial fading in backscatter systems requires a non-zero bandwidth signal. This signal has an upper and lower bandwidth-limit constraint. That is, the bandwidth of the signal should be high enough so that the hardware noise is not masking the data signal. In addition, the bandwidth of the signal should be low enough so the channel is frequency flat.

- As a result from the low-power, low-SNR nature of backscatter systems, the modulated signal should have both good autocorrelation properties and deep DC nulls. In this work, the last row of the Hadamard 8 matrix is used.

- Retrodirective tags, although in general not ideal, reduce the deep nulls observed in their standard counterparts.

- Unlike standard multi-channel systems, retrodirective backscatter systems benefit from the correlation between the underlying channels, the forward and backward channels.

CHAPTER 7
CONCLUSIONS

This dissertation studies the future of backscatter systems from both electromagnetic and communication perspectives. This research addresses the major challenges associated with backscatter systems operating at microwave and mm-wave frequencies. Those challenges are: First, operating at higher-frequencies reduce either the backscatter range or the transponder field-of-view, a tradeoff between the antenna gain and its radiation pattern. Second, the backscattered signal at the interrogator fluctuates randomly such that designing a system that operates under most circumstances is near impossible. This fluctuation is due the pinhole nature of backscatter channels.

To overcome these challenges, this dissertation suggested the use of a backscatter transponder (an RFID tag) equipped with a *retrodirective array* for three reasons:

1. **Retrodirective tags are orientation independent:** Since retrodirective tags reflect the impinging wave where it comes, the field-of-views of these tags are not affected by the array factor. Therefore, a pencil-beam pattern can be observed in all directions as long as these directions fall under the angular support of the array constituent element. The implication of this property is that RFID tags can backscatter at extreme distances, at high frequencies, and in all supported directions.

2. **Retrodirective tags are not doubly faded:** In an ideal case, retrodirective arrays backscatter each plane wave back towards the direction of incidence. Therefore, the presence of a retrodirective tag does not alter the statistics of the channel. In fact, backscatter channels become less random when the standard, non-retrodirective tag is replaced by a retrodirective one. Even when the retrodirective array is not ideal (a finite number of elements), retrodirective tags outperform their standard, non-retrodirective counterparts.

3. **Retrodirective tags have high spectral efficiency:** With hybrid-based retrodirective tags, the backscatter communication spectral efficiency can be increased without changing the physical size of the tag. Not only does the spectral efficiency increase, but this increase can be achieved with either maintaining a fixed SNR or even increasing the SNR if a reflection-type amplifier—such as a tunnel diode—is used.

7.1 Major Contributions

This dissertation thoroughly studied the use of retrodirective arrays in multipath environments. In particular, the major contributions of this dissertation can be summarized as:

- An original retrodirective array using a rat-race coupler is designed and thoroughly tested. This retrodirective array is compact, wideband, and best suited for future backscatter systems.
- An in-depth comparative study on hybrid-based retrodirective arrays is conducted.
- An original theoretical stochastic model for ideal backscatter channel is developed. This model is generic in a sense that it models variety of channels with different propagation geometries (LoS, nLoS, TWDP [53]).
- A first channel-sounding experiment for retrodirective arrays is carried out and that experiment concurred with the postulated theory.
- A fully-automated three-dimensional apparatus is designed. This new automated-system enables more accurate measurements with minimal human interactions.

7.2 Future Work

The results of this work open the doors to various research paths, which can be summarized as:

- *Use high-order modulation schemes.* In this work, all tests are conducted using OOK; changing the modulation to QPSK would be a good compromise between the SNR reduction and increase in the spectral efficiency.

- *Backscatter with tunnel diodes and retrodirective arrays.* This enables extreme distance communications with tags that backscatter only on the desired direction.

- *Use space-time modulation.* When multiple retrodirective tags are used and their data are encoded orthogonally, the channel capacity increases, especially at low SNR [107].

- *Channel sounding with more than two elements.* Increasing the number of the retrodirective array elements makes the channel behave closer to its ideal response. Therefore, testing with more than two elements gives an indication on channel ideality versus the number of antennas.

- *Model the non-ideal retrodirective channel.* Although the physics of the non-ideal retrodirective channel is well understood, a statistical model requires an exhaustive number of experiments with various varying parameters such as the channel K-factor and the forward and backward channel correlation.

7.3 Publications

Most of the work presented in this dissertation comes from the author's published journal and conference papers. The list below contains submitted, accepted, and in-submission articles.

7.3.1 Peer-Reviewed Journal Articles

1). M. Alhassoun and G. D. Durgin, "Spatial Fading in Retrodirective Channels: An Experimental Study," in *IEEE Transactions on Wireless Communications* [In Submission]

2). M. Alhassoun and G. D. Durgin, "A Theoretical Channel Model for Spatial Fading in Retrodirective Backscatter Channels," in *IEEE Transactions on Wireless Communications* [Early Access]

3). M. Alhassoun, M. A. Varner and G. D. Durgin, "Theory and Design of a Retrodirective Rat-Race-Based RFID Tag," in *IEEE Journal of Radio Frequency Identification*, vol. 3, no. 1, pp. 25-34, March 2019.

7.3.2 Peer-Reviewed Conference Papers

1). E Baker, M Alhassoun and G. D. Durgin, "Design of a Circular-Patch Reflectarray for Microwave Power Transfer and Communications in Space," *2019 7th IEEE International Conference on Wireless for Space and Extreme Environments (WiSEE)*, Ottawa, Canada

2). M. Alhassoun and G. D. Durgin, "A Comparative Study of Coupler-Based Retrodirective Arrays for Next-Generation RFID Tags," *2019 IEEE International Conference on RFID Technology Application (RFID-TA)*, Pisa, Italy

3). C. Qi, F. Amato, M. Alhassoun and G. D. Durgin, "Breaking the Range Limit of RFID Localization: Phase-based Positioning with Tunneling Tags," *2019 IEEE International Conference on RFID (RFID)*, Phoenix, AZ, USA, 2019, pp. 1-8. (**Best paper award**)

4). M. Alhassoun and G. D. Durgin, "Spatial Fading in Backscatter Channels: Theory and Models," *2019 16th IEEE Annual Consumer Communications & Networking Conference (CCNC)*, Las Vegas, NV, USA, 2019, pp. 1-6.

5). M. Alhassoun, M. A. Varner and G. D. Durgin, "Low-Observable Reflectors Using Perfect Pulses," *2018 IEEE International Symposium on Antennas and Propagation & USNC/URSI National Radio Science Meeting*, Boston, MA, 2018, pp. 915-916.

6). M. Alhassoun, M. A. Varner and G. D. Durgin, "Design and evaluation of a multi-modulation retrodirective RFID tag," *2018 IEEE International Conference on RFID (RFID)*, Orlando, FL, 2018, pp. 1-8.(**Best paper award**)

7). M. A. Varner, M. Alhassoun and G. D. Durgin, "Partitioned pseudo-retrodirective arrays for capacity expansion of backscatter communication channels," *2018 IEEE International Conference on RFID (RFID)*, Orlando, FL, 2018, pp. 1-7.

8). M. Alhassoun, F. Amato and G. D. Durgin, "A multi-modulation retrodirective feed network for backscatter communications," *2017 IEEE 28th Annual International Symposium on Personal, Indoor, and Mobile Radio Communications (PIMRC)*, Montreal, QC, 2017, pp. 1-5.

9). M. B. Akbar, C. Qi, M. Alhassoun and G. D. Durgin, "Orientation sensing using backscattered phase from multi-antenna tag at 5.8 GHz," *2016 IEEE International Conference on RFID (RFID)*, Orlando, FL, 2016, pp. 1-8.

Appendices

APPENDIX A
EQUIVALENT DIFFUSE COMPONENT DISTRIBUTION

In this appendix, we outline the derivations of Equations (5.13) and (5.15).

A.1 Derivation of Equation (5.13)

When the diffuse components in Equation (3.8)(after setting $V_i \longrightarrow \beta_i$) are uniform (i.e., identical), $\beta_i = u$, where u is a constant. Therefore, we can rewrite Equation (3.8) as

$$V_T(r) = \beta_1 \exp(j\Phi_1) + \sum_{i=2}^{N} u \exp(j\Phi_i). \tag{A.1}$$

The diffuse disparity in Equation (5.9) can be then expressed as

$$\zeta = \frac{\sum_{i=2}^{N} u^4}{\left(\sum_{i=2}^{N} u^2\right)^2} = \frac{u^4(N-1)}{u^4(N-1)^2} = \frac{1}{N-1} \Rightarrow N = 1 + \frac{1}{\zeta}. \tag{A.2}$$

Therefore, the number of the required multipath components is $N = 1+1/\zeta$. The magnitude of u is set by the diffuse power; that is,

$$2\sigma^2 = \sum_{i=2}^{N} u^2 = (N-1)u^2. \tag{A.3}$$

Therefore,

$$u = \sqrt{\frac{2\sigma^2}{N-1}}. \tag{A.4}$$

A.2 Derivation of Equation (5.15)

If we assume that the diffuse components in Equation (3.8)(after setting $V_i \longrightarrow \beta_i$) are geometrically tapered, then we can rewrite Equation (3.8) as

$$V_T(r) = \beta_1 \exp(j\Phi_1) + \sum_{i=2}^{N} a^{(i-2)} \exp(j\Phi_i), \quad |a| \leq 1 \tag{A.5}$$

The diffuse disparity in Equation (5.9) can be then expressed as

$$\zeta = \frac{\sum_{i=2}^{N} a^{4(i-2)}}{\left(\sum_{i=2}^{N} a^{2(i-2)}\right)^2} = \underbrace{\frac{1-a^2}{1+a^2}}_{C} \frac{1+a^{2(N-1)}}{1-a^{2(N-1)}}. \tag{A.6}$$

Solving for N yields

$$N = \ln\left(\frac{\zeta - C}{\zeta + C}\right) / \ln\left(a^2\right) + 1. \tag{A.7}$$

Unlike the case of Equation (5.13), a prior assumption on the value of a is required to determine the value of N and vice versa. However, when N is large and $\sigma^2 > 1/2$, a can be approximated using the following formula:

$$a = \sqrt{\frac{2\sigma^2 - 1}{2\sigma^2}}. \tag{A.8}$$

APPENDIX B
PYTHON CONTROL CODES

The channel sounding experiment is fully automated. A python code is used to interface with the USRP (using GNU Radio) and the two-dimensional positioner. The flow graph of the code is given in Figure B.1. To ensure that the channel is statistic, several pause locations are added to the code. The first one is to ensure that everything in the scene is statistic by allowing ample time for us to leave the experiment scene. The remaining pauses are to ensure that the positioner and cables after the movement are at rest. The code is divided into two parts: The main and supporting functions.

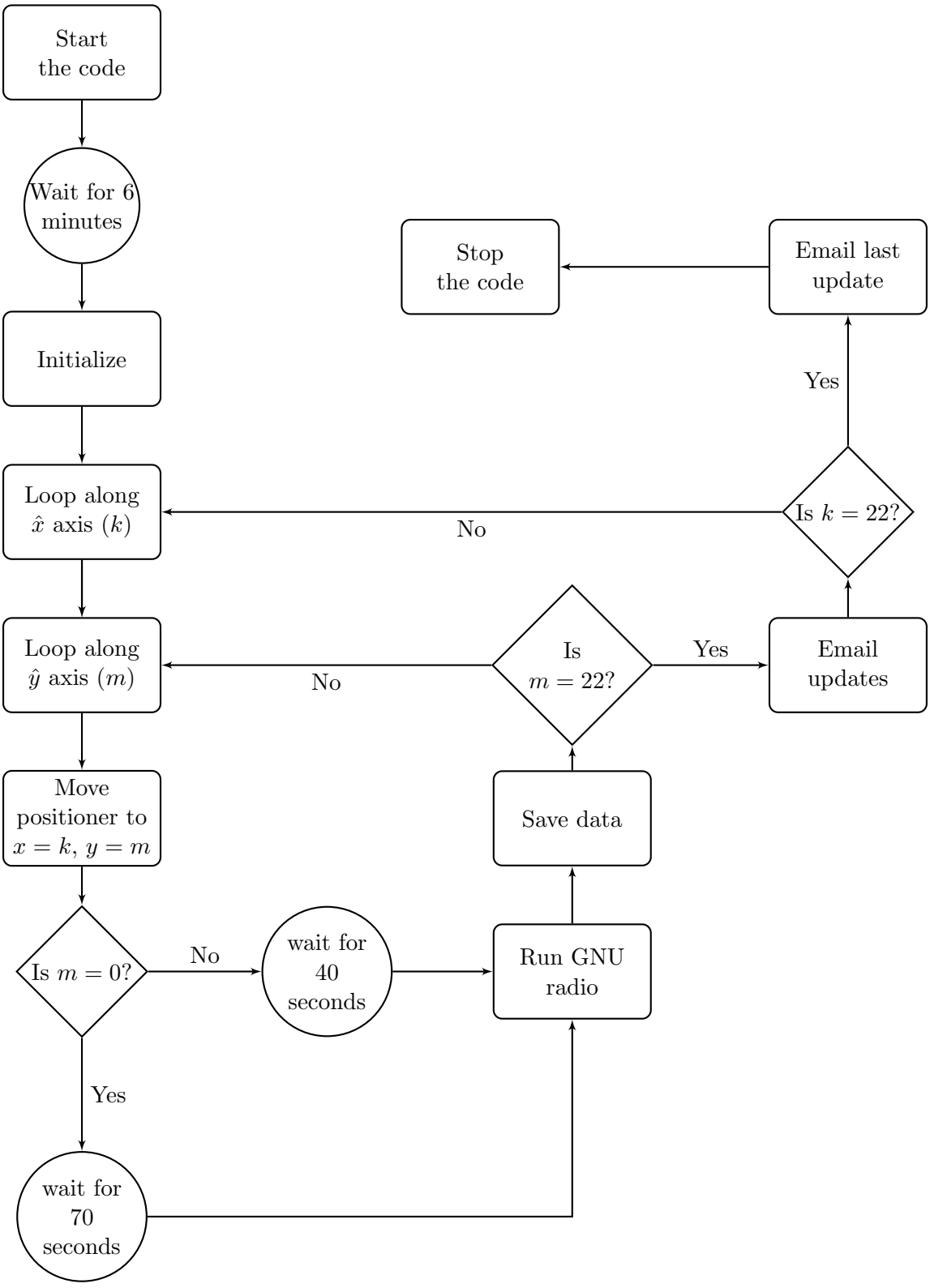

Figure B.1: A flow graph of the code used to for data acquisition in the channel-sounding experiments.

B.1 Main Function

The code main function is shown below.

```
1  # This code is used to control the USRP as well as that Actuator and ...
       extract the complex data
2
3  import shutil
4  import time
5  import os
6  import numpy as np
7  from SendingEmail import SendEmail
8  from PlatformControl import MovePlatform
9
10 StartTime = time.time()
11 time.sleep(360)  # Wait for 360 seconds to start the experiment
12 X = np.linspace(0,21,22)
13 Y = np.linspace(0,21,22)
14
15 RawDataFileName = 'ChannelData09_21_19/RawData/RawDataHad8Samp10MF1M'
16 BPRawDataFileName = 'ChannelData09_21_19/BPRawData/HPRawDataHad8Samp10MF1M'
17 sender = "******@outlook.com"   # Sender's email
18 password = "***"   # Password of the sender's email
19 receiver ="m.s.a.alhassoun@gmail.com"
20
21 # Running the loop
22 for k in range(22):  # X-axis loop
23     for m in range(22):  # Y-axis loop
24         MovePlatform(k,m)
25         if m == 0 and k != 0:
26             time.sleep(70)
27         else:
28             time.sleep(40)  # Wait for 40 seconds to ensure the platform ...
                   is stable
29         os.system("./ChannelData.py")  # Run the GNU radio code
30         time.sleep(10)
```

```
31          Added="X{0}Y{1}.bin".format(int(k),int(m))
32          shutil.copy2('RawData.bin', RawDataFileName+Added)
33          shutil.copy2('BPRawData.bin', BPRawDataFileName+Added)
34          time.sleep(3)
35
36      CurrentTime = time.time()
37      ElapsedTime = (CurrentTime - StartTime)/60 # in minutes
38      if k != 22:
39          Location = 'Subject: Update {0} \n\n Now at x = {0} cm, which ...
                means {1}%'\
40          'is completed.\n The elapsed time is {2} minutes'\
41          .format(k+1, int((k+1)/22*100), int(ElapsedTime))
42          SendEmail(Location, sender, password, receiver)
43      else:
44          break
45  TimeHours=np.floor(ElapsedTime/60)
46  TimeMinutes=((ElapsedTime/60)-TimeHours)*60
47  ExperimentEnded = 'Subject: Final Update\n\n'\
48      'The experiment is completed. Total time is {0} hours and {1} minutes'\
49      .format(int(TimeHours), int(TimeMinutes))
50  SendEmail(ExperimentEnded, sender, password, receiver)
```

B.2 Move-Platform Function

The function shown below is used to move the two-dimensional positioner. It is called during the run of the main function.

```
# This script is meant to control serial ports

import numpy as np
import serial


def MovePlatform(XCent,YCent):

    # XCent= Movement in the X-axis in centimeters
    # YCent= Movement in the Y-axis in centimeters
    # ZCent= Movement in the Z-axis in centimeters
    # IniEnable= Enable initialization of the platform

    # Pre defined values
    CentToIn = 0.393701  # cm to inches
    XCal = 0  # 8.7  # Calibrate the x-axis to the actual location ...
        indicated in the ruler
    YCal = 0  # -13.2
    XIN = (XCent + XCal) * CentToIn
    YIN = (YCent + YCal) * CentToIn
    XString = XIN * 8000 * -1
    YString = YIN * 8000 * -1

    ########### Serial Port

    ser = serial.Serial()
    ser.port = '/dev/ttyUSB0'
    ser.baudrate = 19200
    ser.bytesize = 8
    ser.parity = 'N'
```

```
30      ser.stopbits = 1
31      ser.open()
32
33      temp1 = 'SH XY\r'
34      ser.write(temp1.encode())
35
36      temp2 = f"PA{int(XString)},{int(YString)},0\r"
37      ser.write(temp2.encode())
38      temp3 = 'BG XY\r'
39      ser.write(temp3.encode())
40      ser.close()
```

B.3 Send-Email Function

The function shown below is used to send email with updates about the experiment. It is called during the run of the main function.

```
# This function sends an email using Python

import smtplib

def SendEmail(content, sender, password, receiver):

    mail = smtplib.SMTP('smtp-mail.outlook.com', 587)
    mail.ehlo()
    mail.starttls()
    mail.ehlo
    mail.login(sender, password)
    mail.sendmail(sender, receiver, content)
    mail.close()
```

B.4 GNU Radio Function

The function shown below is used to run GNU radio in the shell. The function is generated from the GNU Radio Companion, a graphical flow-graph tool.

```
#!/usr/bin/env python2
# -*- coding: utf-8 -*-
##################################################
# GNU Radio Python Flow Graph
# Title: Channeldata
# Generated: Sat Sep  7 17:38:16 2019
##################################################


if __name__ == '__main__':
    import ctypes
    import sys
    if sys.platform.startswith('linux'):
        try:
            x11 = ctypes.cdll.LoadLibrary('libX11.so')
            x11.XInitThreads()
        except:
            print "Warning: failed to XInitThreads()"

from gnuradio import blocks
from gnuradio import eng_notation
from gnuradio import filter
from gnuradio import gr
from gnuradio import uhd
from gnuradio.eng_option import eng_option
from gnuradio.filter import firdes
from grc_gnuradio import wxgui as grc_wxgui
from numpy import floor
from optparse import OptionParser
import time
```

```
31 import wx
32
33
34 class ChannelData(grc_wxgui.top_block_gui):
35
36     def __init__(self):
37         grc_wxgui.top_block_gui.__init__(self, title="Channeldata")
38         _icon_path = "/usr/share/icons/hicolor/32x32/apps/gnuradio-grc.png"
39         self.SetIcon(wx.Icon(_icon_path, wx.BITMAP_TYPE_ANY))
40
41         ##################################################
42         # Variables
43         ##################################################
44         self.samp_rate = samp_rate = 10e6
45         self.f_LCutOff = f_LCutOff = 30e3
46         self.f_HCutOff = f_HCutOff = 50e3
47         self.DataPoints = DataPoints = 2**15
48
49         ##################################################
50         # Blocks
51         ##################################################
52         self.uhd_usrp_source_0 = uhd.usrp_source(
53             ",".join(("", "")),
54             uhd.stream_args(
55                 cpu_format="fc32",
56                 channels=range(1),
57             ),
58         )
59         self.uhd_usrp_source_0.set_clock_source('external', 0)
60         self.uhd_usrp_source_0.set_samp_rate(samp_rate)
61         self.uhd_usrp_source_0.set_center_freq(0, 0)
62         self.uhd_usrp_source_0.set_gain(0, 0)
63         self.high_pass_filter_0 = filter.fir_filter_ccf(1, firdes.high_pass(
64             1, samp_rate, f_LCutOff, 10e3, firdes.WIN_HAMMING, 6.76))
65         self.blocks_skiphead_0_0 = ...
                blocks.skiphead(gr.sizeof_gr_complex*1, 1024)
```

```
66          self.blocks_skiphead_0 = blocks.skiphead(gr.sizeof_gr_complex*1, ...
                1024)
67          self.blocks_head_0_0 = blocks.head(gr.sizeof_gr_complex*1, ...
                DataPoints)
68          self.blocks_head_0 = blocks.head(gr.sizeof_gr_complex*1, DataPoints)
69          self.blocks_file_sink_0_0 = ...
                blocks.file_sink(gr.sizeof_gr_complex*1, ...
                '/home/malhassoun/PycharmProjects/testSerial/BPRawData.bin', ...
                False)
70          self.blocks_file_sink_0_0.set_unbuffered(False)
71          self.blocks_file_sink_0 = ...
                blocks.file_sink(gr.sizeof_gr_complex*1, ...
                '/home/malhassoun/PycharmProjects/testSerial/RawData.bin', False)
72          self.blocks_file_sink_0.set_unbuffered(False)
73
74          ##################################################
75          # Connections
76          ##################################################
77          self.connect((self.blocks_head_0, 0), (self.blocks_file_sink_0, 0))
78          self.connect((self.blocks_head_0_0, 0), ...
                (self.blocks_file_sink_0_0, 0))
79          self.connect((self.blocks_skiphead_0, 0), ...
                (self.high_pass_filter_0, 0))
80          self.connect((self.blocks_skiphead_0_0, 0), (self.blocks_head_0, 0))
81          self.connect((self.high_pass_filter_0, 0), (self.blocks_head_0_0, 0))
82          self.connect((self.uhd_usrp_source_0, 0), ...
                (self.blocks_skiphead_0, 0))
83          self.connect((self.uhd_usrp_source_0, 0), ...
                (self.blocks_skiphead_0_0, 0))
84
85      def get_samp_rate(self):
86          return self.samp_rate
87
88      def set_samp_rate(self, samp_rate):
89          self.samp_rate = samp_rate
90          self.uhd_usrp_source_0.set_samp_rate(self.samp_rate)
```

```
91          self.high_pass_filter_0.set_taps(firdes.high_pass(1, ...
                self.samp_rate, self.f_LCutOff, 10e3, firdes.WIN_HAMMING, 6.76))
92
93      def get_f_LCutOff(self):
94          return self.f_LCutOff
95
96      def set_f_LCutOff(self, f_LCutOff):
97          self.f_LCutOff = f_LCutOff
98          self.high_pass_filter_0.set_taps(firdes.high_pass(1, ...
                self.samp_rate, self.f_LCutOff, 10e3, firdes.WIN_HAMMING, 6.76))
99
100     def get_f_HCutOff(self):
101         return self.f_HCutOff
102
103     def set_f_HCutOff(self, f_HCutOff):
104         self.f_HCutOff = f_HCutOff
105
106     def get_DataPoints(self):
107         return self.DataPoints
108
109     def set_DataPoints(self, DataPoints):
110         self.DataPoints = DataPoints
111         self.blocks_head_0_0.set_length(self.DataPoints)
112         self.blocks_head_0.set_length(self.DataPoints)
113
114
115 def main(top_block_cls=ChannelData, options=None):
116
117     tb = top_block_cls()
118     tb.Start(True)
119     #tb.Wait()
120     time.sleep(3)
121
122
123 if __name__ == '__main__':
124     main()
```

APPENDIX C
READER BOARDS

We used a custom-built reader in all of this dissertation experiments. In particular, the reader in Figure 6.1 has three printed circuit boards (PCB's) that correspond to three distinct components. To simplify the debugging process, each component is allocated a distinct PCB.

C.1 Low-Noise Amplifier (LNA)

The low-noise amplifier (LNA) is the first element in the receive chain of the reader. In the system we built, we used Analog Devices Inc. (ADI) HMC902LP3E, which has a de-embedded gain of 19 dB. However, the measured gain is below that of the datasheet for two reasons:

1. The substrate is FR4, which has a relatively high loss tangent at 5.8 GHz.

2. The feed lines to and from the LNA are made long, which makes it easier to test them.

Nonetheless, the measured gain is approximately 13 dB. The circuit was built on a four-layer substrate and the chip is placed on the top layer (the thickness of the top dielectric layer is 0.17 mm), which results in narrower transmission lines that are about the size of chip leads. The circuit schematic is shown in Figure C.1 and the circuit layout is shown in Figure C.2.

C.2 IQ Downconverter

Since the received signal is complexly-modulated, we used ADI HMC951BLP4E that has a conversion gain of 13 dB. The downconverter circuit schematic and layout are shown in Figures C.3 and C.4, respectively. The in-phase and quadrature are externally DC blocked and fed to the baseband operational amplifier (OpAmp).

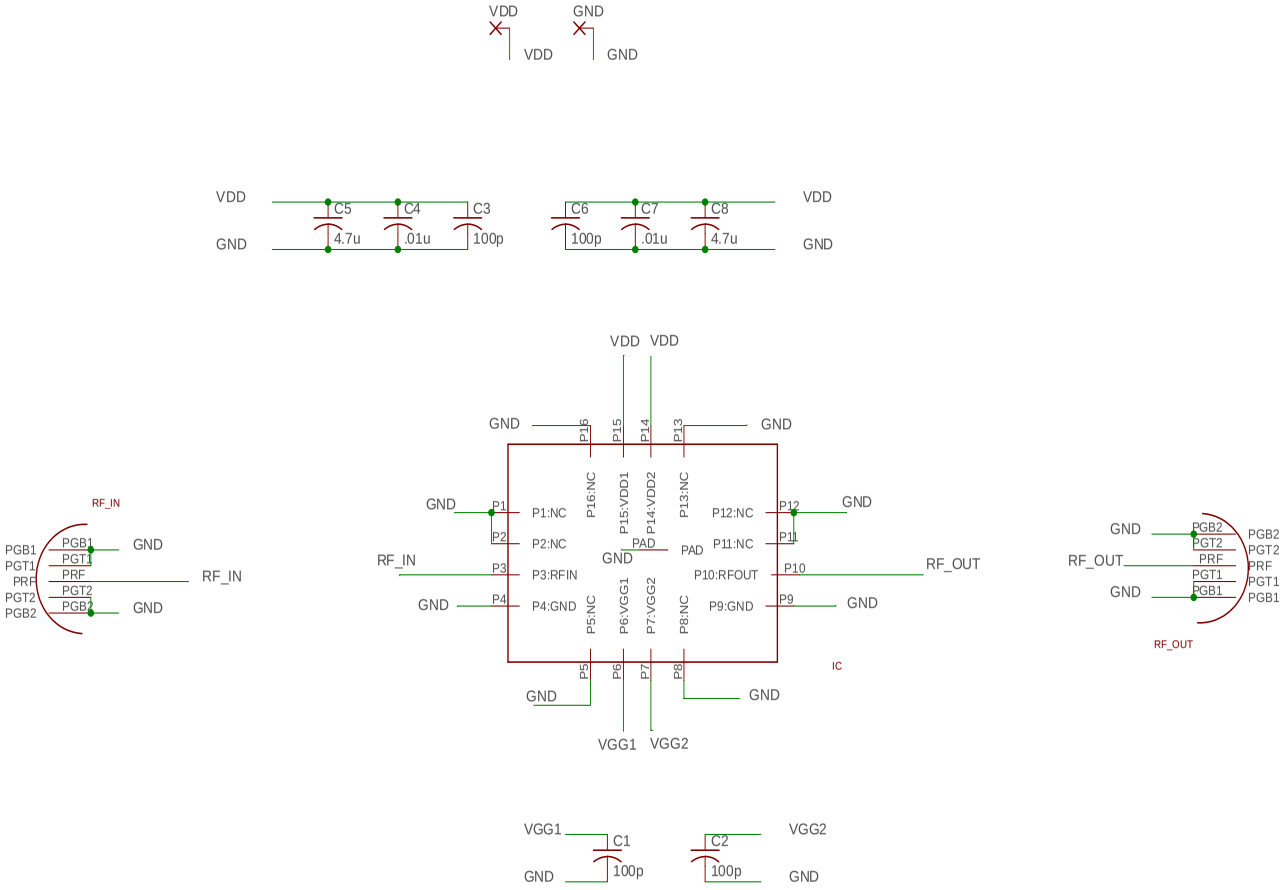

Figure C.1: The schematic of the LNA (using Autodesk Eagle).

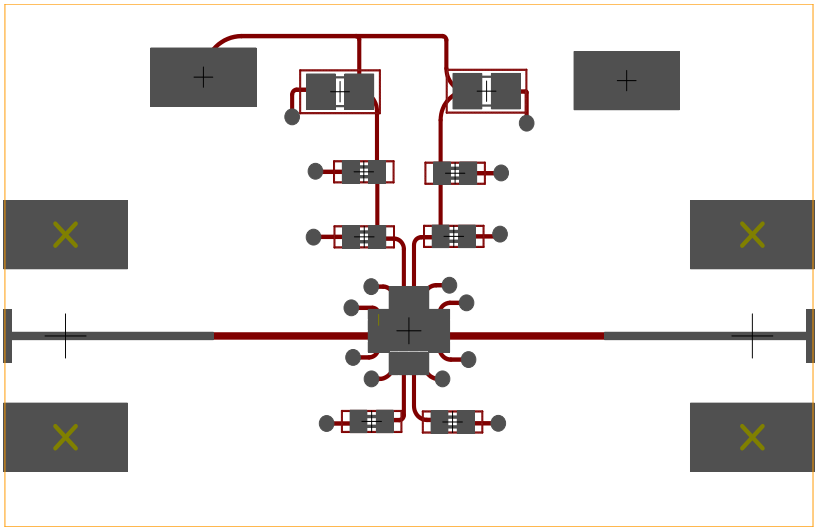

Figure C.2: The LNA circuit layout (using Autodesk Eagle).

C.3 Operational Amplifier

The outputs of the IQ downconverter is DC blocked and fed to a dual, low-noise OpAmp. In these experiments, we used Texas Instruments(TI) OPA2846. The OpAmp is configured in the inverting mode with a linear voltage gain of 20 ($G = -20$). Since TI has sample unpopulated evaluation boards with about the same price as designing these boards, we used the evaluation boards and populated them with the required components. A photograph of the board is given in Figure C.5.

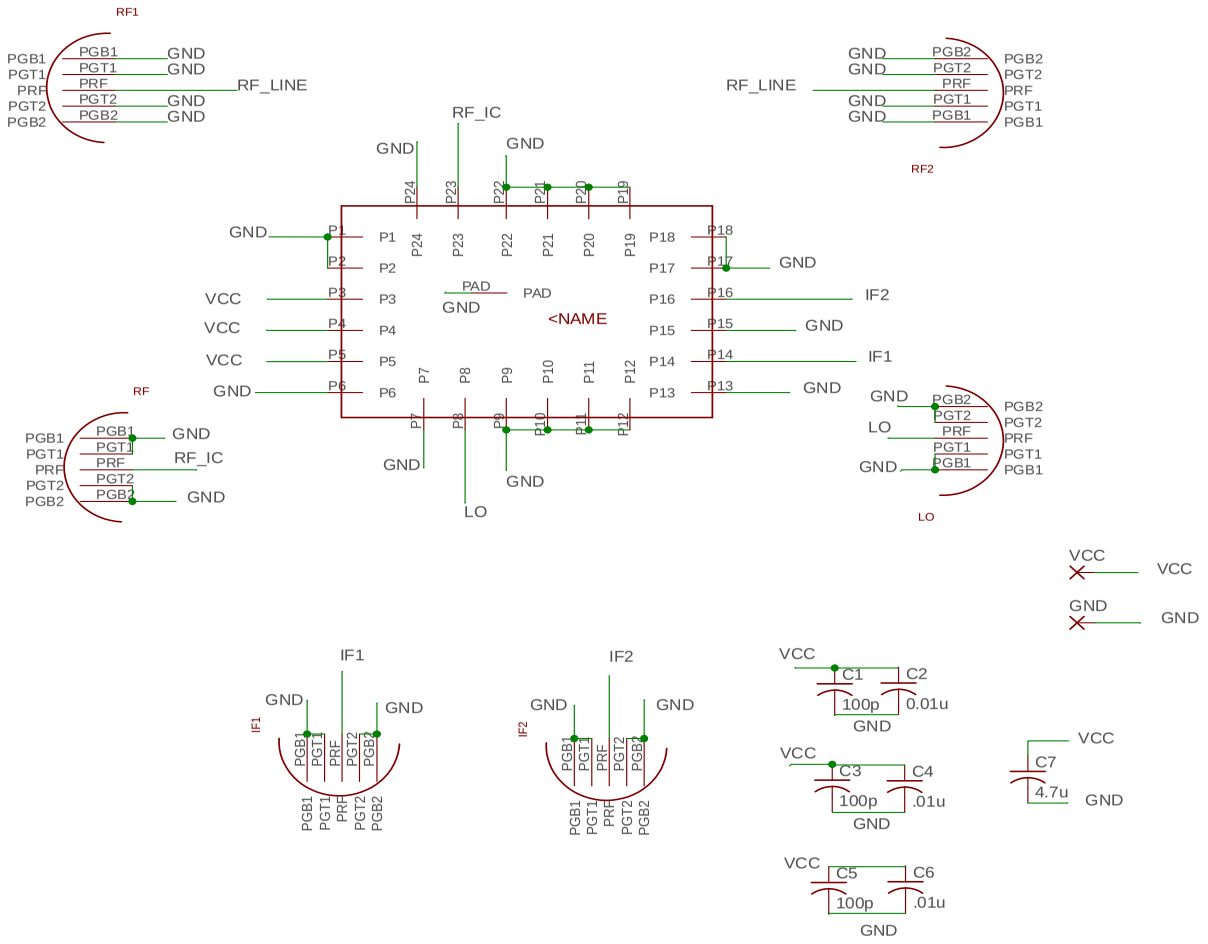

Figure C.3: The schematic of the IQ downconverter (using Autodesk Eagle).

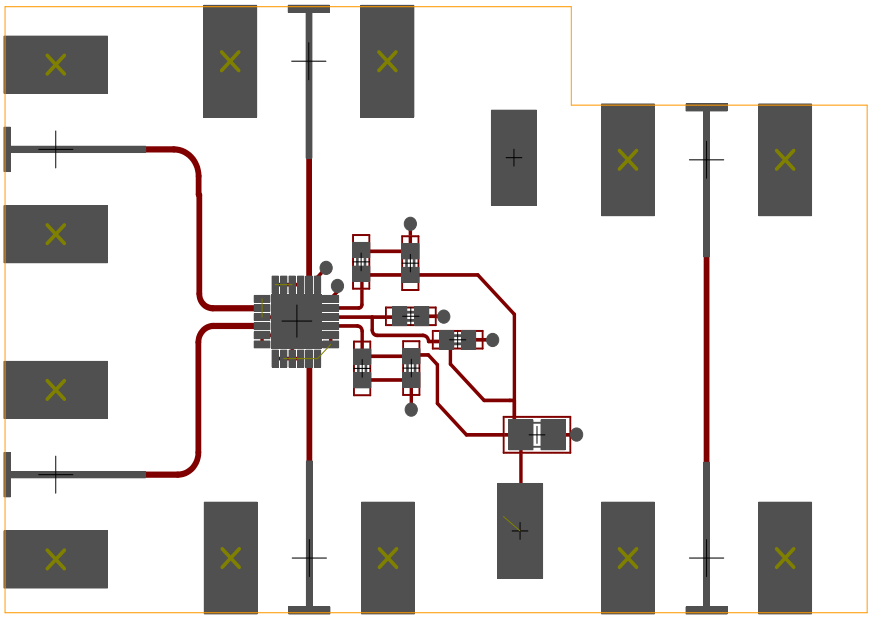

Figure C.4: The downconverter circuit layout (using AUTODESK EAGLE). The extra transmission line in the right side of the board is used for de-embedding.

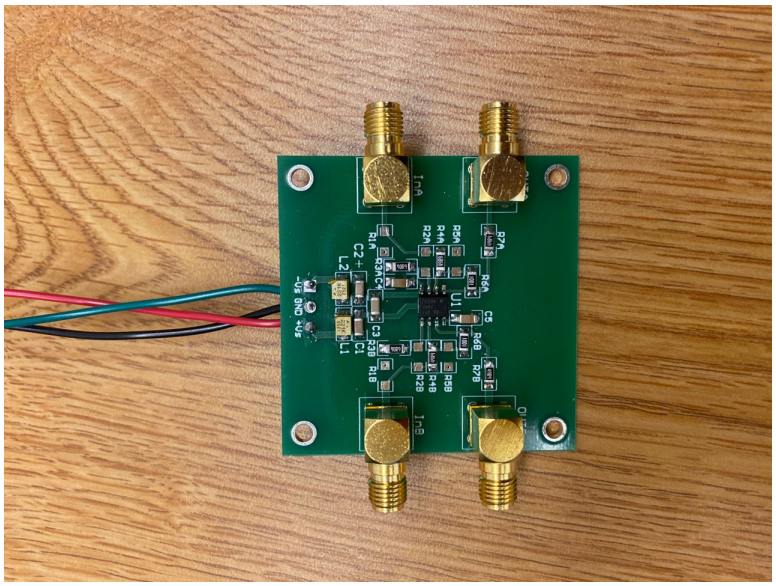

Figure C.5: A photograph of the baseband OpAmp.

APPENDIX D
TAG BOARDS

The tags used in this research are custom built with the exception of the RF switches, which are MINI-CIRCUITS ZFSWA2-63DR+ absorptive, SPDT switches. The PCB-based parts of the tags are: A single antenna, rat-race-based retrodirective array, and branch-line-based retrodirective array.

D.1 RF Switch Characterizations

A ZFSWA2-63DR+ switch has two throw ports: RF1 and RF2. In all the experiments, RF1 is connected to a short-circuit load while RF2 is always connected a 50-Ω load. Let us label one of them SW1 (with Γ_1) and the other SW2 (with Γ_2). Then, the measured reflection coefficients are

$$\Gamma_{1,\text{Short}} = 0.460 + j0.524 \Longrightarrow 20\log_{10}\|\Gamma_{1,\text{Short}}\|^2 = -3.1 \text{ dB}, \tag{D.1}$$

$$\Gamma_{1,50\ \Omega} = 0.270 + j0.040 \Longrightarrow 20\log_{10}\|\Gamma_{1,\text{Short}}\|^2 = -13.5 \text{ dB}, \tag{D.2}$$

$$\Gamma_{2,\text{Short}} = 0.446 + j0.595 \Longrightarrow 20\log_{10}\|\Gamma_{1,\text{Short}}\|^2 = -2.5 \text{ dB}, \tag{D.3}$$

and

$$\Gamma_{2,50\ \Omega} = 0.234 + j0.062 \Longrightarrow 20\log_{10}\|\Gamma_{1,\text{Short}}\|^2 = -12.3 \text{ dB}. \tag{D.4}$$

Since neither the magnitude of Γ_{Short} (in the $20\log_{10}$ sense) is 0 dB nor that of $\Gamma_{50\ \Omega}$ is close to $-\infty$, a reduction in the modulation factor is observed. In fact, the theoretical modulation

Table D.1: Patch antenna specifications (referenced to Figure D.1)

Parameter	Value (mm)
Resonant Length (L)	13.4
Non-resonant Length (W)	17
Feed Line Depth (x_i)	3.6
Feed and patch Gap (g)	2
Feed Line Width (W_{50})	3.5
Board Dimensions	60×60
Board Thickness	1.6
Conductor Thickness	17.5×10^{-3}
Substrate Material	Rogers 4003C

factor for this configuration is -6 dB and the measured one (using Equation (4.26) in the case of the single-antenna tag) is -12.4 dB, which results in a 6.4 dB backscatter power loss.

D.2 Tag Design

All three tags are designed using iterative and sequential processes. The radiating element (the antenna) is simulated using Ansys HFSS while the feed network is simulated using the momentum simulator in Keysight ADS. The licenses to these software tools are provided by Georgia Tech. The measured responses of these tags along with their pictures are shown in Figures 4.20–4.22. All of these three tags share the same antenna, whose specifications are listed in Table D.1 and layout is depicted in Figure D.1.

The schematic and layout of the retrodirective tags are shown in Figures D.2–D.5. The dimensions are given in the Keysight ADS schematic. However, the schematics do not show the antennas, which are identical to that in Figure D.1 and Table D.1.

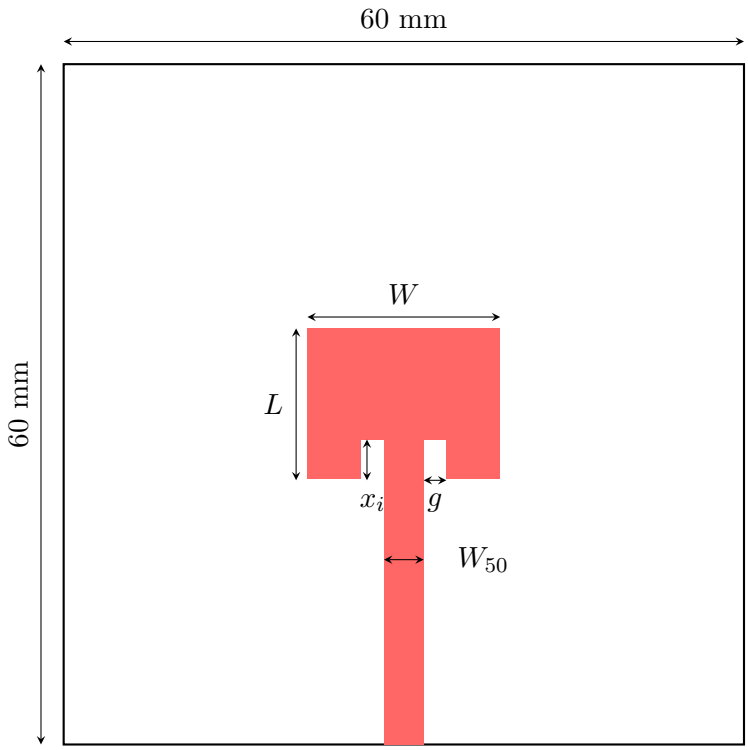

Figure D.1: The layout of the single-element patch antenna.

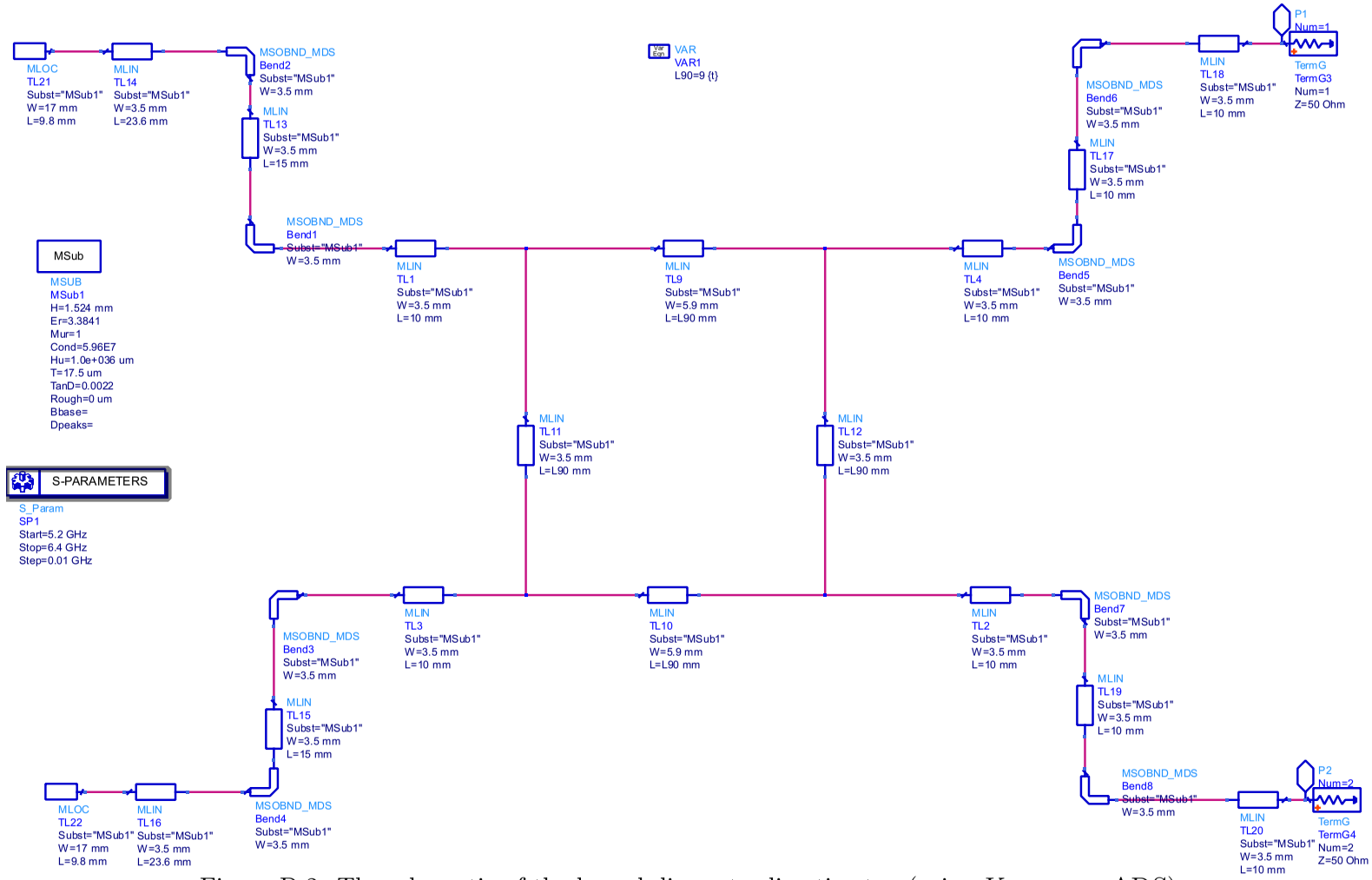

Figure D.2: The schematic of the branch-line retrodirective tag (using KEYSIGHT ADS).

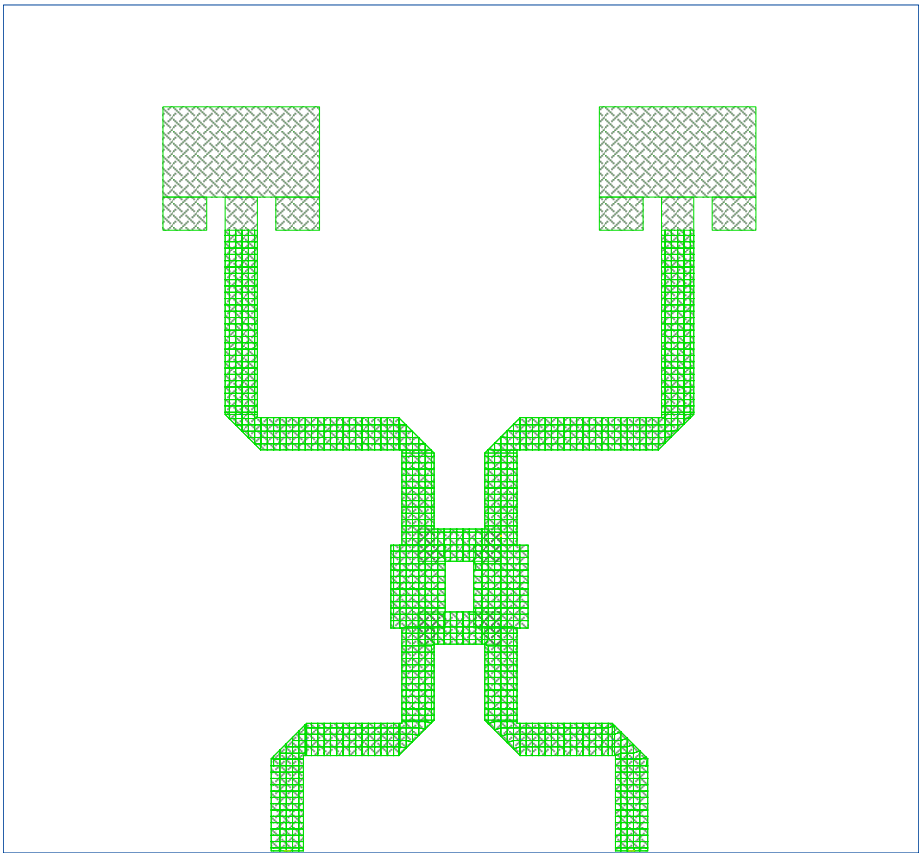

Figure D.3: The layout of the branch-line retrodirective tag (using KEYSIGHT ADS).

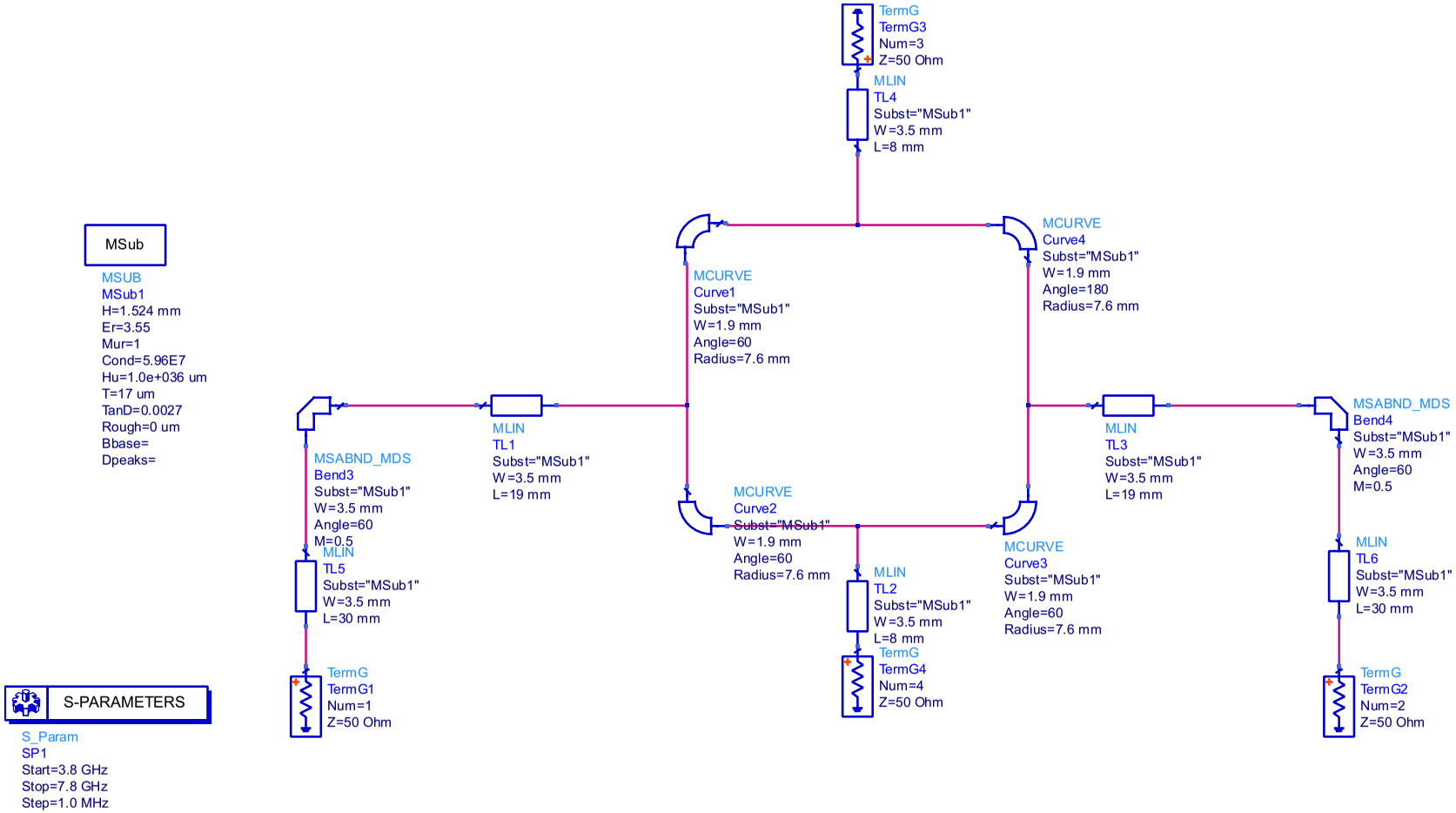

Figure D.4: The schematic of the rat-race retrodirective tag (using KEYSIGHT ADS).

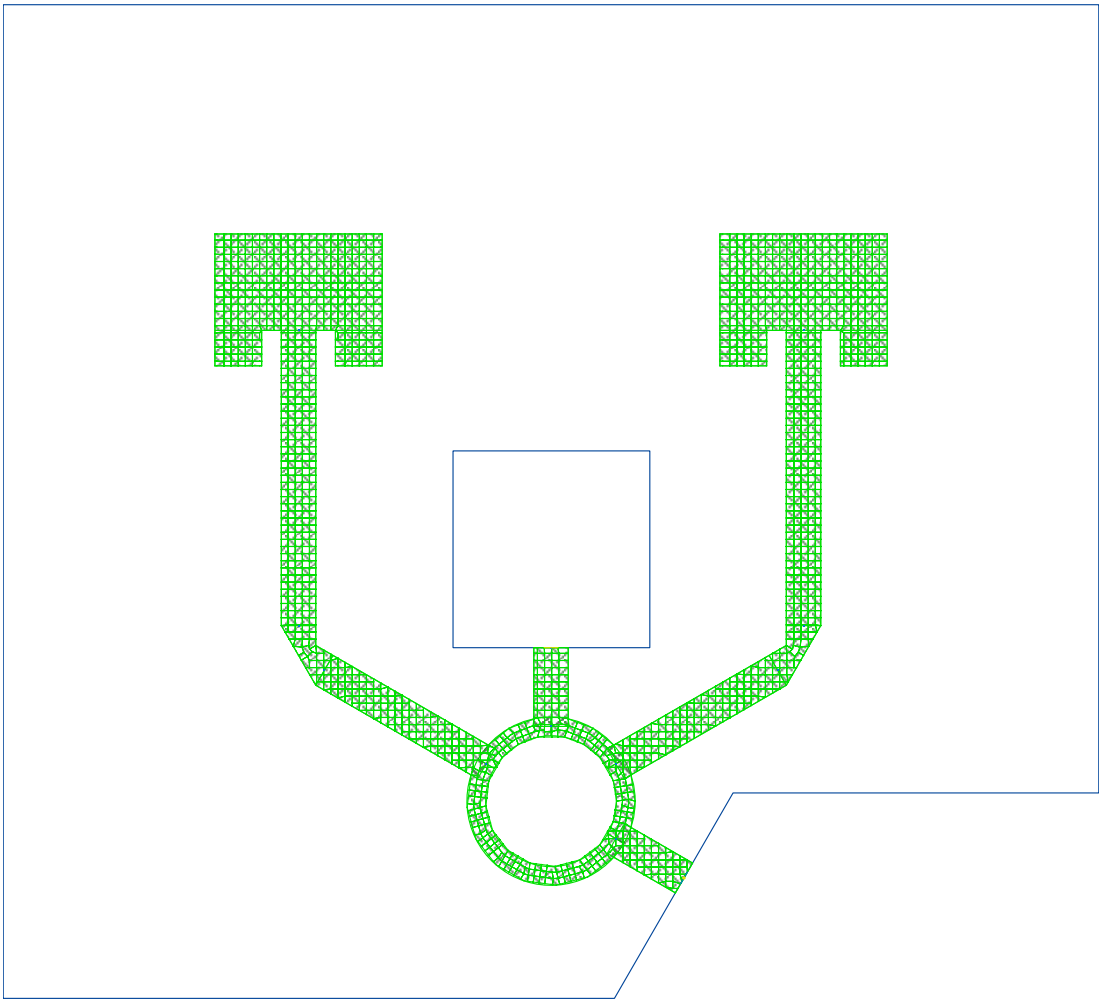

Figure D.5: The layout of the rat-race retrodirective tag (using Keysight ADS).

APPENDIX E
CHANNEL STATISTIC SIMULATION

In many cases, simulating the statistics of wireless channels gives an insight on the envelope distribution of the received complex-valued signal. In this appendix, we show how to simulate the received signal envelope for the Rayleigh and Rician fading geometry. In both cases: the equation that we want simulate is

$$V = V_1 \exp(j\Phi_i) + \sum_{i=2}^{N} V_i \exp(j\Phi_i) \sim Z, \tag{E.1}$$

where Z is a zero-mean complex random variable, which results from the fact that all components in Equation (E.1) have a zero mean. In addition, we assume that if $V_1 \neq 0$, its power is comparable to the summation power such that the central limit theorem does not hold [57].

E.1 Rayleigh Fading

When $V_1 = 0$, then Equation (E.1) is modeled as a complex Gaussian random variable, $\mathcal{CN}(0, 2\sigma^2)$, where σ^2 is the standard deviation of the real and imaginary parts. We can use the following MATLAB experiment with 10,000 channel realizations to verify the distribution:

```
N=1e4; % Number of multipath components
Nrel=1e4; % Number of channel realizations
for i=1:Nrel
VDiffuse(i)=(1/sqrt(N))*sum(randn(N,1).*exp((j*2*pi).*rand(N,1)));
        % The diffuse voltage of each realizations is power normalized ...
            (1/sqrt(N))
end
% Plotting: We use "histfit", which is a function that plots histogram
%  and fits the data to the desired distribution
figure; % Without declaring a figure, each histfit overwrites the ...
```

```
    previous one
10  histfit(abs(VDiffuse),1e2,'Rayleigh') % Envelope histogram
11  figure;
12  histfit(real(VDiffuse),1e2,'normal')  % Real part histogram
13  figure;
14  histfit(imag(VDiffuse),1e2,'normal')  % Imaginary part histogram
```

The output plots are shown in Figures E.1–E.3.

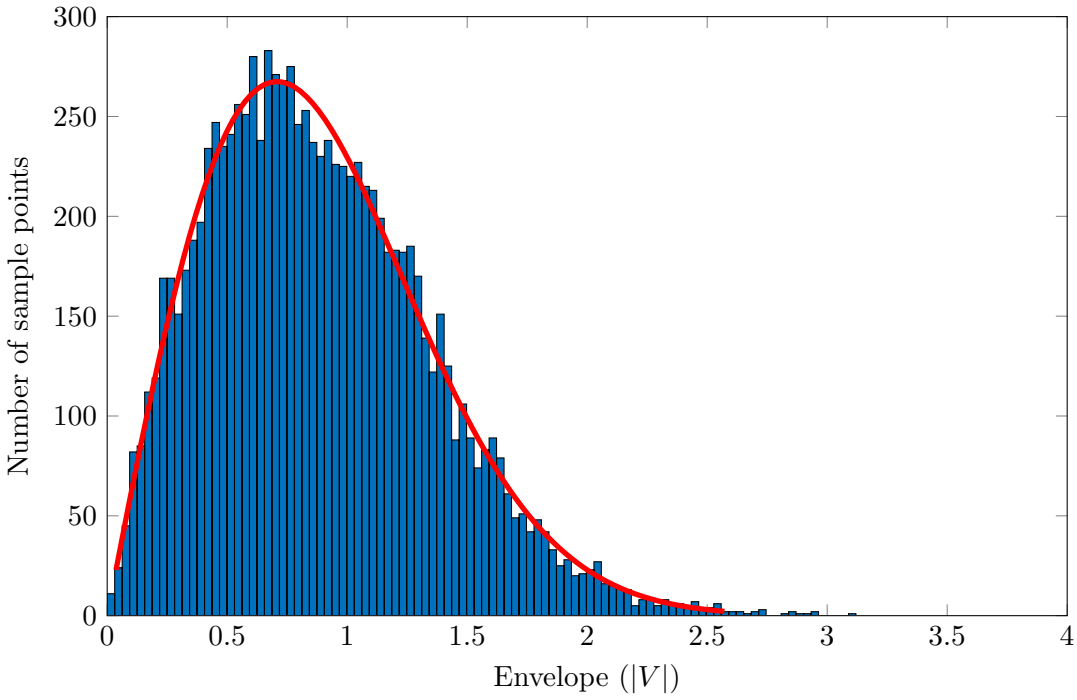

Figure E.1: The envelope distribution of 10,000 channel realizations. The plot results from line 10 in the MATLAB code. The red curve is the fitted Rayleigh PDF.

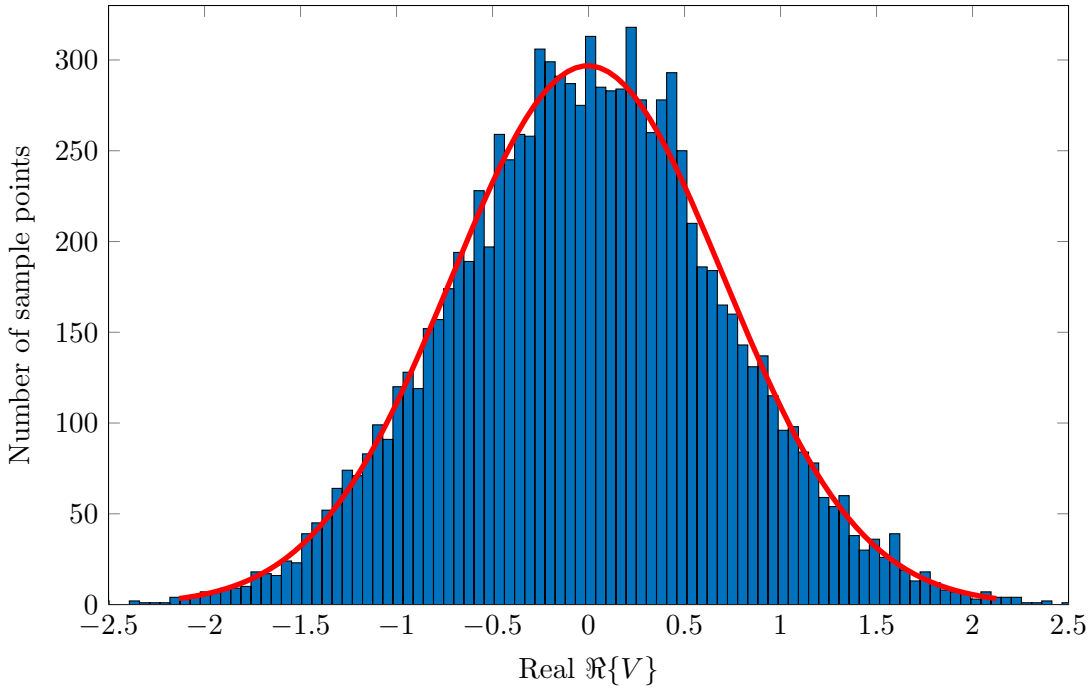

Figure E.2: The results from line 12 in the MATLAB code. The red curve is the fitted zero mean Gaussian PDF.

E.2 Rician Fading

In the case of Rician fading, $V_1 \neq 0$ in Equation (E.1) and the the central limit theorem does not hold. We can use the following MATLAB experiment with 10,000 channel realizations to verify the distribution:

```
1 N=1e4; % Number of multipath components
2 Sigma=1; % Standard deviation of the real and imaginary part of the Gaussian
3          % random variable.
4 X=randn(N,1); % In-phase components
5 Y=randn(N,1); % Phase-quadrature components
6 KdB=10; % The Rician K-factor in dB scale "10*log10"
7 VSpecular=sqrt(10^(KdB/10)*2*sigma); % The specular amplitude
8 Z=VSpecular.*exp(-(j*2*pi).*rand(N,1))+X+j.*Y; % Total Voltage
9 histfit(abs(Z),1e2,'Rician')
```

The code output is plotted in Figure E.4.

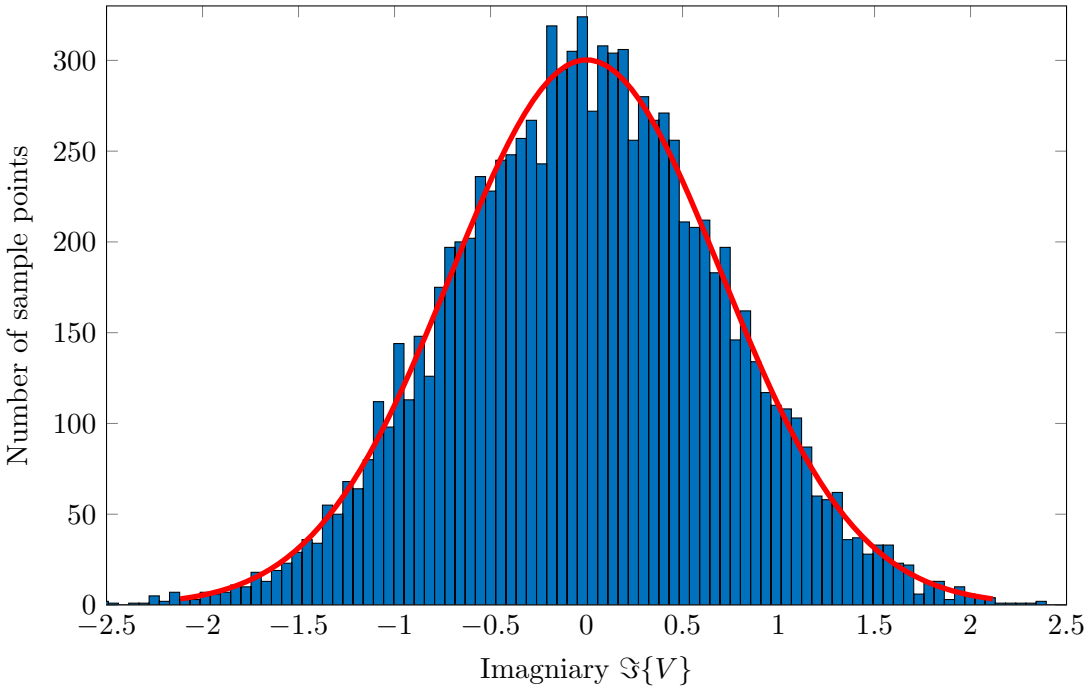

Figure E.3: The results from line 14 in the MATLAB code. The red curve is the fitted zero mean Gaussian PDF.

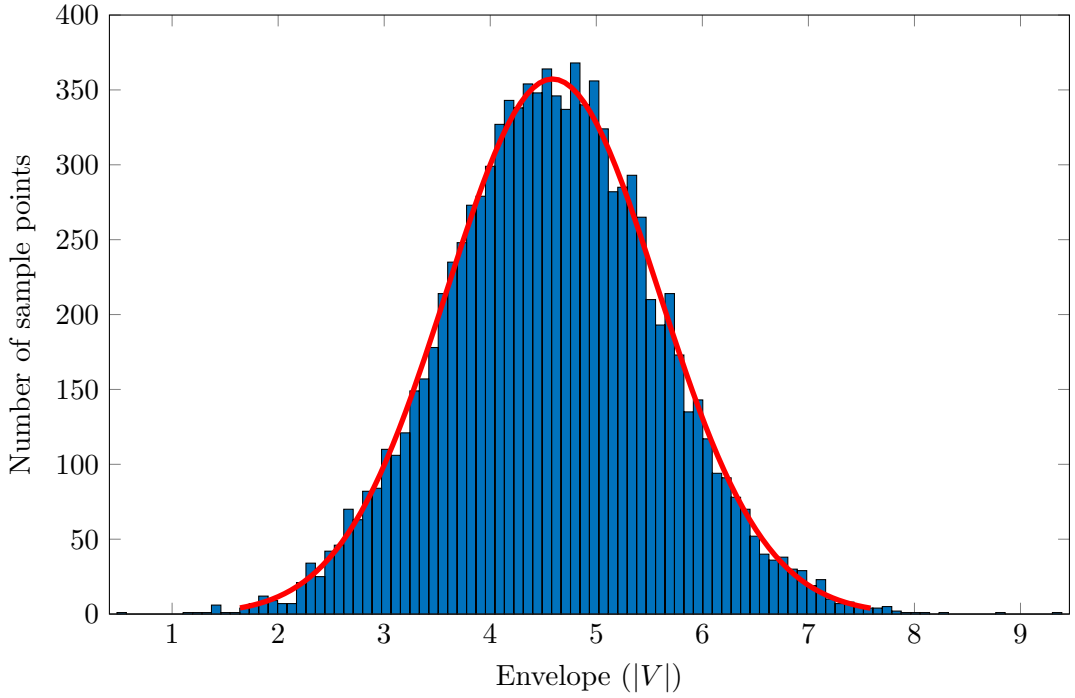

Figure E.4: The envelope distribution of 10,000 channel realizations. The plot results from line 10 in the MATLAB code. The red curve is the fitted Rician PDF.

REFERENCES

[1] J. Griffin, "High-frequency modulated-backscatter communication using multiple antennas," PhD thesis, Georgia Institute of Technology, 2009.

[2] G. Koo, Y. Lu, and G. D. Durgin, "Multi-antenna signaling scheme for low-powered or passive radio communications," pat., US Patent 9,231,292, 2016.

[3] B. R. Marshall, "Staggered pattern energy harvesting and retro-directive backscatter communications for passive RFID tags and sensors," PhD thesis, Georgia Institute of Technology, 2018.

[4] J. Landt, "The history of RFID," *IEEE Potentials*, vol. 24, no. 4, pp. 8–11, 2005.

[5] H. Stockman, "Communication by means of reflected power," *Proceedings of the IRE*, vol. 36, no. 10, pp. 1196–1204, 1948.

[6] A. R. Koelle, S. W. Depp, and R. W. Freyman, "Short-range radio-telemetry for electronic identification, using modulated RF backscatter," *Proceedings of the IEEE*, vol. 63, no. 8, pp. 1260–1261, 1975.

[7] D. M. Dobkin, *The RF in RFID: Passive UHF RFID in Practice*. Elsevier, 2007.

[8] M. Roberti. (2005). The history of RFID technology, [Online]. Available: `http://www.rfidjournal.com/articles/view?1338` (visited on 12/17/2017).

[9] K. Modolo. (2018). IATA follows Delta's lead with RFID bag tag mandate, [Online]. Available: `https://news.delta.com/iata-follows-deltas-lead-rfid-bag-tag-mandate` (visited on 08/01/2019).

[10] (2019). Resolution: RFID Baggage Tracking Set for Global Deployment, [Online]. Available: `https://www.iata.org/pressroom/pr/Pages/2019-06-02-05.aspx` (visited on 08/04/2019).

[11] M. Trotter, "Range finding in passive wireless sensor networks using power-optimized waveforms," PhD thesis, Georgia Institute of Technology, 2011.

[12] G. Koo, "Signal constallation of a retrodirective array phase modulator," Master's thesis, Georgia Institute of Technology, Elect. and Comp. Eng., Atlanta, GA, 2011.

[13] (2013). EPC Radio-Frequency Identity Protocols Generation-2 UHF RFID, [Online]. Available: `https://www.gs1.org/sites/default/files/docs/epc/uhfc1g2_2_0_0_standard_20131101.pdf` (visited on 08/18/2019).

[14] M. Alhassoun and G. D. Durgin, "A theoretical channel model for spatial fading in retrodirective backscatter channels," *IEEE Transactions on Wireless Communications*, pp. 1–1, 2019.

[15] J. D. Griffin and G. D. Durgin, "Complete link budgets for backscatter-radio and RFID systems," *IEEE Antennas and Propagation Magazine*, vol. 51, no. 2, pp. 11–25, 2009.

[16] M. Lenehan. (2019). Far-Field Antenna, [Online]. Available: `https://support.impinj.com/hc/en-us/articles/202755618-Far-Field-Antenna` (visited on 08/18/2019).

[17] W. Lee, S. Khang, W. Lee, H. Tae, and J. Yu, "Wide-coverage array antenna using a dual-beam switching for UHF RFID applications," in *2013 IEEE International Conference on RFID (RFID)*, 2013, pp. 36–41.

[18] N. C. Karmakar, P. Zakavi, and M. Kumbukage, "Development of a phased array antenna for universal UHF RFID reader," in *2010 IEEE Antennas and Propagation Society International Symposium*, 2010, pp. 1–4.

[19] C. Qi, J. D. Griffin, and G. D. Durgin, "Low-power and compact microwave RFID reader for sensing applications in space," in *2018 IEEE International Conference on RFID Technology Application (RFID-TA)*, 2018, pp. 1–6.

[20] (2015). How much does an RFID tag cost today? [Online]. Available: `https://www.rfidjournal.com/faq/show?85` (visited on 08/21/2019).

[21] R. J. Vyas, V. Lakafosis, Z. Konstas, and M. M. Tentzeris, "Design of a novel, battery-less, solar powered wireless tag for enhanced range remote tracking applications," in *2009 IEEE Antennas and Propagation Society International Symposium*, 2009, pp. 1–4.

[22] A. P. Sample, J. Braun, A. Parks, and J. R. Smith, "Photovoltaic enhanced UHF RFID tag antennas for dual purpose energy harvesting," in *2011 IEEE International Conference on RFID*, 2011, pp. 146–153.

[23] M. J. Brady, D.-W. Duan, and V. S. Kodukula, "Radio frequency identification system," pat., US Patent 6,100,804, 2000.

[24] J. Z. Huang, P. H. Yang, W. C. Chew, and T. T. Ye, "A compact broadband patch antenna for UHF RFID tags," in *2009 Asia Pacific Microwave Conference*, 2009, pp. 1044–1047.

[25] M. S. R. Bashri, M. I. Ibrahimy, and S. M. A. Motakabber, "A planar wideband inductively coupled feed patch antenna for UHF RFID tag," in *2013 IEEE International Conference on RFID-Technologies and Applications (RFID-TA)*, 2013, pp. 1–6.

[26] H. Chen and Y. Tsao, "Broadband capacitively coupled patch antenna for RFID tag mountable on metallic objects," *IEEE Antennas and Wireless Propagation Letters*, vol. 9, pp. 489–492, 2010.

[27] You Chung Chung and Kyounghwan Lee, "2.4GHz Yagi-Uda RFID tag antenna design with low back-lobe using genetic algorithm," in *2008 IEEE Radio and Wireless Symposium*, 2008, pp. 475–478.

[28] (2001). Federal communications commission, [Online]. Available: `https://www.gpo.gov/fdsys/pkg/CFR-2001-title47-vol1/pdf/CFR-2001-title47-vol1-sec15-247.pdf` (visited on 12/23/2017).

[29] (2019). The European table of frequency allocations and applications in the frequency range 8.3 kHz to 3000 GHz (ECA table), [Online]. Available: `https://www.ecodocdb.dk/download/2ca5fcbd-4090/ERCREP025.pdf` (visited on 08/22/2019).

[30] G. D. Durgin, C. R. Valenta, M. B. Akbar, M. M. Morys, B. R. Marshall, and Yenpao Lu, "Modulation and sensitivity limits for backscatter receivers," in *2013 IEEE International Conference on RFID (RFID)*, 2013, pp. 124–130.

[31] (2016). Attenuation by atmospheric gases, [Online]. Available: `https://www.itu.int/dms_pubrec/itu-r/rec/p/R-REC-P.676-11-201609-I!!PDF-E.pdf` (visited on 08/24/2019).

[32] (2019). Fcc online table of frequency allocations, [Online]. Available: `https://transition.fcc.gov/oet/spectrum/table/fcctable.pdf` (visited on 08/24/2019).

[33] (2019). Electronic code of federal regulations: Part 15 – Radio frequency devices, [Online]. Available: `https://www.ecfr.gov/cgi-bin/ECFR?page=browse` (visited on 08/24/2019).

[34] F. Guidi, N. Decarli, D. Dardari, F. Mani, and R. D'Errico, "Passive millimeter-wave RFID using backscattered signals," in *2016 IEEE Globecom Workshops (GC Wkshps)*, 2016, pp. 1–6.

[35] S. Kasap, *Optoelectronics and Photonics: Principles and Practices*. Pearson, 2013.

[36] R. F. Harrington, "Small resonant scatterers and their use for field measurements," *IRE Transactions on Microwave Theory and Techniques*, vol. 10, no. 3, pp. 165–174, 1962.

[37] J. H. Richmond, "A modulated scattering technique for measurement of field distributions," *IRE Transactions on Microwave Theory and Techniques*, vol. 3, no. 4, pp. 13–15, 1955.

[38] R. B. Green, "The general theory of antenna scattering," PhD thesis, Ohio State University, 1663.

[39] R. C. Hansen, "Relationships between antennas as scatterers and as radiators," *Proceedings of the IEEE*, vol. 77, no. 5, pp. 659–662, 1989.

[40] P. V. Nikitin, K. V. S. Rao, and R. D. Martinez, "Differential RCS of RFID tag," *Electronics Letters*, vol. 43, no. 8, pp. 431–432, 2007.

[41] W. K. Kahn and H. Kurss, "Minimum-scattering antennas," *IEEE Transactions on Antennas and Propagation*, vol. 13, no. 5, pp. 671–675, 1965.

[42] R. E. Collin and F. J. Zucker, *Antenna theory*. McGraw-Hill, 1969.

[43] H. T. Friis, "A note on a simple transmission formula," *Proceedings of the IRE*, vol. 34, no. 5, pp. 254–256, 1946.

[44] M. A. Richards, *Fundamentals of radar signal processing*. McGraw-Hill Education, 2014.

[45] J. Prothro, "Improved performance of a radio frequency identification tag antenna on a metal ground plane," Master's thesis, Georgia Institute of Technology, Elect. and Comp. Eng., Atlanta, GA, 2007.

[46] F. Amato, H. M. Torun, and G. D. Durgin, "RFID backscattering in long-range scenarios," *IEEE Transactions on Wireless Communications*, vol. 17, no. 4, pp. 2718–2725, 2018.

[47] C. R. Valenta and G. D. Durgin, "Harvesting wireless power: Survey of energy-harvester conversion efficiency in far-field, wireless power transfer systems," *IEEE Microwave Magazine*, vol. 15, no. 4, pp. 108–120, 2014.

[48] J. R. Barry, E. A. Lee, and D. G. Messerschmitt, *Digital communication*. Springer Science & Business Media, 2012.

[49] S. J. Thomas, E. Wheeler, J. Teizer, and M. S. Reynolds, "Quadrature amplitude modulated backscatter in passive and semipassive UHF RFID systems," *IEEE Transactions on Microwave Theory and Techniques*, vol. 60, no. 4, pp. 1175–1182, 2012.

[50] S. J. Thomas and M. S. Reynolds, "A 96 Mbit/sec, 15.5 pJ/bit 16-QAM modulator for UHF backscatter communication," in *2012 IEEE International Conference on RFID (RFID)*, 2012, pp. 185–190.

[51] C. Boyer and S. Roy, "Coded QAM backscatter modulation for RFID," *IEEE Transactions on Communications*, vol. 60, no. 7, pp. 1925–1934, 2012.

[52] S. Ebrahimi-Asl, M. T. Ghasr, and M. J. Zawodniok, "Design of dual-loaded RFID tag for higher order modulations," *IEEE Transactions on Microwave Theory and Techniques*, vol. 66, no. 1, pp. 410–419, 2018.

[53] G. D. Durgin, *Space-time wireless channels*. Prentice Hall Professional, 2003.

[54] I. Cuinas and M. G. Sanchez, "Measuring, modeling, and characterizing of indoor radio channel at 5.8 GHz," *IEEE Transactions on Vehicular Technology*, vol. 50, no. 2, pp. 526–535, 2001.

[55] R. Vaughan and J. B. Andersen, *Channels, propagation and antennas for mobile communications*. IET, 2003, vol. 50.

[56] W. L. Stutzman and G. A. Thiele, *Antenna theory and design*. John Wiley & Sons, 2013.

[57] P Beckman, *Probability in Communication Engineering*. New York: Haracourt, Brace & World, Inc., 1967.

[58] R. D. Lord, "The use of the Hankel transform in statistics I. General theory and examples," *Biometrika*, vol. 41, no. 1/2, pp. 44–55, 1954.

[59] A. Abdi, H. Hashemi, and S. Nader-Esfahani, "On the PDF of the sum of random vectors," *IEEE Transactions on Communications*, vol. 48, no. 1, pp. 7–12, 2000.

[60] M. Rao, F. J. Lopez-Martinez, M. Alouini, and A. Goldsmith, "MGF approach to the analysis of generalized two-ray fading models," *IEEE Transactions on Wireless Communications*, vol. 14, no. 5, pp. 2548–2561, 2015.

[61] J. D. Griffin and G. D. Durgin, "Gains for RF tags using multiple antennas," *IEEE Transactions on Antennas and Propagation*, vol. 56, no. 2, pp. 563–570, 2008.

[62] M. Alhassoun and G. D. Durgin, "Spatial fading in backscatter channels: Theory and models," in *2019 16th IEEE Annual Consumer Communications Networking Conference (CCNC)*, 2019, pp. 1–6.

[63] I. S. Gradshteyn and I. M. Ryzhik, *Table of integrals, series, and products*. Academic press, 2014.

[64] M. K. Simon, *Probability distributions involving Gaussian random variables: A handbook for engineers and scientists*. Kluwer Academic Publishers, 2002.

[65] J. D. Griffin and G. D. Durgin, "Link envelope correlation in the backscatter channel," *IEEE Communications Letters*, vol. 11, no. 9, pp. 735–737, 2007.

[66] D. Arnitz, U. Muehlmann, and K. Witrisal, "Wideband characterization of backscatter channels: Derivations and theoretical background," *IEEE Transactions on Antennas and Propagation*, vol. 60, no. 1, pp. 257–266, 2012.

[67] A. Goldsmith, *Wireless communications*. Cambridge university press, 2005.

[68] M. K. Simon and M.-S. Alouini, *Digital communication over fading channels*. John Wiley & Sons, 2005, vol. 95.

[69] M. Alhassoun, M. A. Varner, and G. D. Durgin, "Theory and design of a retrodirective rat-race-based RFID tag," *IEEE Journal of Radio Frequency Identification*, vol. 3, no. 1, pp. 25–34, 2019.

[70] R. Kronberger, T. Knie, R. Leonardi, U. Dettmar, M. Cremer, and S. Azzouzi, "UHF RFID localization system based on a phased array antenna," in *2011 IEEE International Symposium on Antennas and Propagation (APSURSI)*, 2011, pp. 525–528.

[71] M. Abbak and I. Tekin, "RFID coverage extension using microstrip-patch antenna array [wireless corner]," *IEEE Antennas and Propagation Magazine*, vol. 51, no. 1, pp. 185–191, 2009.

[72] L. Viglione, D. Mason, and P. Primiani, *Wireless power transmission using phased array antennae*, US Patent 8,879,995, 2014.

[73] L. C. Van Atta, "Electromagnetic reflector," pat. 2 908 002, Oct. 1959.

[74] E. Sharp and M. Diab, "Van Atta reflector array," *IRE Transactions on Antennas and Propagation*, vol. 8, no. 4, pp. 436–438, 1960.

[75] C. Pon, "Retrodirective array using the heterodyne technique," *IEEE Transactions on Antennas and Propagation*, vol. 12, no. 2, pp. 176–180, 1964.

[76] G. D. Durgin, "RFID virtual journal - issue 3," *IEEE RFID Virtual Journal*, 2014.

[77] C. W. Pobanz and T. Itoh, "A conformal retrodirective array for radar applications using a heterodyne phased scattering element," in *Proceedings of 1995 IEEE MTT-S International Microwave Symposium*, 1995, 905–908 vol.2.

[78] F. Amato and G. D. Durgin, "Signal-to-noise ratio measurements for IoT communications with quantum tunneling reflectors," in *2016 IEEE 3rd World Forum on Internet of Things (WF-IoT)*, 2016, pp. 383–388.

[79] T. Brabetz, V. F. Fusco, and S. Karode, "Balanced subharmonic mixers for retrodirective-array applications," *IEEE Transactions on Microwave Theory and Techniques*, vol. 49, no. 3, pp. 465–469, 2001.

[80] J. Tuovinen, G. S. Shiroma, W. E. Forsyth, and W. A. Shiroma, "Multipath communications using a phase-conjugate array," in *IEEE MTT-S International Microwave Symposium Digest, 2003*, vol. 3, 2003, 1681–1684 vol.3.

[81] S. L. Karode and V. F. Fusco, "Use of an active retrodirective antenna array as a multipath sensor," *IEEE Microwave and Guided Wave Letters*, vol. 7, no. 12, pp. 399–401, 1997.

[82] S.-J. Chung and K. Chang, "A retrodirective microstrip antenna array," *IEEE Transactions on Antennas and Propagation*, vol. 46, no. 12, pp. 1802–1809, 1998.

[83] W.-J. Tseng, S.-B. Chung, and K. Chang, "A planar Van Atta array reflector with retrodirectivity in both E-plane and H-plane," *IEEE Transactions on Antennas and Propagation*, vol. 48, no. 2, pp. 173–175, 2000.

[84] M. S. Trotter, C. R. Valenta, G. A. Koo, B. R. Marshall, and G. D. Durgin, "Multi-antenna techniques for enabling passive RFID tags and sensors at microwave frequencies," in *2012 IEEE International Conference on RFID (RFID)*, 2012, pp. 1–7.

[85] H.-T. Chen and S.-J. Chung, "Design of a planar array transponder with broad responding beam," *IEEE Microwave and Guided Wave Letters*, vol. 7, no. 9, pp. 297–299, 1997.

[86] P. Chan and V. Fusco, "Bi-static 5.8 GHz RFID range enhancement using retrodirective techniques," in *2011 41st European Microwave Conference*, 2011, pp. 976–979.

[87] Y.-J. Ren and K. Chang, "New 5.8-GHz circularly polarized retrodirective rectenna arrays for wireless power transmission," *IEEE Transactions on Microwave Theory and Techniques*, vol. 54, no. 7, pp. 2970–2976, 2006.

[88] X. X. Yang, C. Jiang, A. Z. Elsherbeni, F. Yang, and Y. Q. Wang, "A novel compact printed rectenna for data communication systems," *IEEE Transactions on Antennas and Propagation*, vol. 61, no. 5, pp. 2532–2539, 2013.

[89] J. Butler and R. Howe, "Beam-forming matrix simplifies design of electronically scanned antennas," *Electronic design*, vol. 9, pp. 170–173, 1961.

[90] S. N. Hsieh and T. H. Chu, "Linear retro-directive antenna array using 90° hybrids," *IEEE Transactions on Antennas and Propagation*, vol. 56, no. 6, pp. 1573–1580, 2008.

[91] S.-J. Chung, S.-M. Chen, and Y.-C. Lee, "A novel bi-directional amplifier with applications in active Van Atta retrodirective arrays," *IEEE Transactions on Microwave Theory and Techniques*, vol. 51, no. 2, pp. 542–547, 2003.

[92] L. C. Hsu and T. G. Ma, "Data modulation of a reflection-type retrodirective array," *IEEE Antennas and Wireless Propagation Letters*, vol. 16, pp. 1196–1199, 2017.

[93] M. M. Islam, K. Rasilainen, S. K. Karki, and V. Viikari, "Designing a passive retrodirective wireless sensor," *IEEE Antennas and Wireless Propagation Letters*, vol. 16, pp. 1739–1742, 2017.

[94] C. Y. Pon, "Hybrid-ring directional coupler for arbitrary power divisions," *IRE Trans. Microwave Theory Tech.*, vol. 9, no. 6, pp. 529–535, 1961.

[95] M. Alhassoun, F. Amato, and G. Durgin, "A multi-modulation retrodirective feed network for backscatter communications," *IEEE International Symposium on Personal, Indoor, and Mobile Radio Communications*, 2017.

[96] M. Alhassoun, M. A. Varner, and G. D. Durgin, "Design and evaluation of a multi-modulation retrodirective RFID tag," in *2018 IEEE International Conference on RFID (RFID)*, 2018, pp. 1–8.

[97] F. Amato, C. W. Peterson, M. B. Akbar, and G. D. Durgin, "Long range and low powered RFID tags with tunnel diode," in *2015 IEEE International Conference on RFID Technology and Applications (RFID-TA)*, 2015, pp. 182–187.

[98] M. Alhassoun and G. D. Durgin, "A comparative study of coupler-based retrodirective arrays for next-generation RFID tags," in *2019 IEEE International Conference on RFID Technology Application (RFID-TA)*, 2019, pp. 1–5.

[99] J. G. Proakis, *Digital signal processing: principles algorithms and applications*. Pearson Education India, 2001.

[100] R. Y. Miyamoto and T. Itoh, "Retrodirective arrays for wireless communications," *IEEE Microwave Magazine*, vol. 3, no. 1, pp. 71–79, 2002.

[101] A. D. Broumas, H. Ling, and T. Itoh, "Transmission properties of a right-angle microstrip bend with and without a miter," *IEEE Trans. Microwave Theory Tech.*, vol. 37, no. 5, pp. 925–929, 1989.

[102] R. L. Haupt, *Antenna arrays: a computational approach*. John Wiley & Sons, 2010.

[103] G. D. Durgin and B. P. Degnan, "A better channel code than FM0 for next-generation RFID," in *2017 IEEE International Conference on RFID (RFID)*, 2017, pp. 1–5.

[104] C. Qi, F. Amato, M. Alhassoun, and G. D. Durgin, "Breaking the range limit of RFID localization: Phase-based positioning with tunneling tags," in *2019 IEEE International Conference on RFID (RFID)*, 2019, pp. 1–8.

[105] W. L. Stutzman and G. A. Thiele, *Antenna theory and design*. John Wiley & Sons, 2012.

[106] M. Alhassoun. (2019). Retrodirective-channel-sounding, [Online]. Available: `https://github.com/malhassoun3/Retrodirective-Channel-Sounding` (visited on 10/27/2019).

[107] M. A. Varner, M. Alhassoun, and G. D. Durgin, "Partitioned pseudo-retrodirective arrays for capacity expansion of backscatter communication channels," in *2018 IEEE International Conference on RFID (RFID)*, 2018, pp. 1–7.

VITA

Mohammad S. Alhassoun received the B.Sc. degree in electrical engineering from King Fahd University of Petroleum and Minerals (KFUPM), Saudi Arabia in 2013 and the MS and PhD degrees from the Georgia Institute of Technology, Atlanta in 2015 and 2019, respectively. His PhD research pertains to retrodirective RFID tags, millimeter-wave RFID technology, and stochastic models of backscatter channels. He is the recipient of both the 2018 and 2019 IEEE International Conference on RFID best paper award. He previously worked at Nokia Bell Labs as an EMCD intern and a graduate assistance at KFUPM where he was awarded the best lab instructor in the Department of Electrical Engineering. He also spent nine weeks as a visiting researcher in the Portable Radio Research Group (MPRG) at Virginia Tech. He was also awarded the Tech to Teaching Certificate in College Teaching from the Georgia Institute of Technology in addition to the Associate Level Certificate from the Center of Integration of Research, Teaching and Learning. He was the instructor of record for ECE3710 at Georgia Tech. In the spring of 2020, he started an assistant professor position at KFUPM, Saudi Arabia.